Characterisation of Dye-Sensitized Solar Cells for Process Control

Peltola, Timo

Award date:
2015

Awarding institution:
University of Bath

Characterisation of Dye-Sensitized Solar Cells for Process Control

submitted by

Timo Peltola

for the degree of Doctor of Philosophy

of the

University of Bath

Department of Physics

August 2014

Summary

Dye-sensitized solar cells are a class of photovoltaics that have shown promise in producing electricity at a reasonable price. Although the processes limiting performance of the devices are quite well understood, their quantification has not been incorporated into a single consistent framework. In this study this framework, based on continuum charge transport equations, is presented and used to investigate the effectiveness of common characterisation methods. Approximate analytical solutions to the model are also derived and it is shown that these can be used to solve the device model inverse problem by fitting the solutions to impedance spectroscopy measurements. Experimental results indicate that the overall device model is a good description of the system and that it can be used to quantify different power loss mechanisms.

Additionally some initial work was undertaken to formulate a charge transport model for a new class of photovoltaics called perovskite cells. The cell is modelled as a p-i-n heterojunction where the perovskite absorber is an intrinsic semiconductor sandwiched between two selective contacts. Simulations indicate that a significant built-in field drives free charges towards the contacts significantly improving charge collection.

Declaration of Work Done in Conjunction with Others

All of the work in this thesis was carried out by the author with the following exceptions:

Fabrication of the experimental dye-sensitized solar cell in chapter 5 was conducted by Thomas Risbridger.

The perovskite solar cells in chapter 7 were made by Giles Eperon and measured by Adam Pockett.

Contents

Chapter 1

Introduction

1.1 Motivation for the Study

One of the key challenges of this century is to respond to the ever growing demand for energy without sacrificing quality of human life either in the short or the long term. Present reliance on fossil fuels is undesirable as eventually exploitable deposits will be depleted and burning carbon compounds releases a number of harmful materials into the atmosphere. Indeed the Brent Crude spot benchmark price for crude oil has risen from approximately 18 United States dollars in 1999 to about 108 in 2013 [1] — a six-fold increase in just fourteen years — and current proven reserves are estimated to be sufficient for only half a century of production at present levels [1]. World Health Organization has also stated that air pollution may account for more than one percent of total mortality worldwide [2]. One would therefore prefer to extract energy from cleaner and more sustainable sources than fossil fuels.

The average solar power that reaches the surface of Earth is about $1.2 \cdot 10^{17}$ W [3] which can be compared to the total world primary energy consumption of $1.7 \cdot 10^{13}$ W as given by the oil company BP [1]. Clearly solar power has technical potential to be one of the biggest sources of energy globally. It also has the advantages of being renewable, clean and suitable to both small and large scale energy production. Solar radiation can be converted into heat using simple absorbers or directly into electricity using photovoltaic devices (commonly known as solar cells). Traditional silicon-based solar cells have good efficiency and stability but they are, at present, too costly [4] to manufacture and deploy to be commercially competitive with traditional power generation. One possible alternative technology is the dye-sensitized solar cell (DSSC). This type of cell should be relatively cheap, easy to manufacture and has shown promise in high efficiency [5] and adequate lifetime [6]. To date, a number of problems in combining high efficiency, stability and simple manufacturing [7, 8] have hindered the commercial adoption of this technology. Therefore considerable effort is directed towards improving cell efficiency and stability through identifying and utilizing new materials.

1.2 Aims and Scope

Due to the vast quantity of possible material combinations that can be employed in dye solar cells, simple trial and error is very unlikely to produce the optimal materials and processing methods. Performance characterization through several different measurements is used to gain insight into optimal cell construction. As the system produces electricity from light, natural ways to probe it are various optical and electrical measurements. This study will examine electrical measurements as these are generally simple enough to conduct on complete solar cells yielding crucial in situ information.

A dye solar cell is a quite a complicated system and any interpretation of electrical measurements requires a theory for cell operation. A relatively simple diffusion model has been developed over the course of the last two decades and successfully used by many authors to explain various measurements [9, 10, 11, 12, 13, 14, 15, 16, 17, 18, 19]. However, in its most advanced formulations [19], the diffusion model requires numerical methods in order to solve it, and therefore there have been few studies where a quantitative agreement between measured and calculated cell performance has been achieved without any arbitrary additions to the model [18, 19]. In this study it is shown that under certain conditions the complicated diffusion model can be simplified to the point where closed form solutions are feasible and that these solutions can be exploited to refine the model parameters in order to obtain highly accurate predictions. The overall methodology enables quantitative analysis of several performance limiting factors in fully assembled solar cells and could be in principle adapted to production line quality control.

Before delving into the diffusion model in chapter 4, some essential solid state physics is reviewed in chapter 2 and an introduction to solar cell physics and characterization methods is given in chapter 3. The analytical solutions and their application to both simulated and experimental data are shown in chapters 5 and 6. Additionally chapter 7 contains some early work on a charge transport model for a new perovskite solar cell that has the same advantages as the dye cell but better performance.

Chapter 2

Essential Solid State Physics

2.1 Electrons in Matter and the Schrödinger Equation

According to classical quantum mechanics, an electron orbiting an atomic nucleus is described by the Schrödinger equation of the form

$$\frac{ih}{2\pi} \cdot \frac{\partial \psi}{\partial t} = -\frac{h^2}{4\pi^2 \mu} \nabla^2 \psi - \frac{qQ}{4\pi\epsilon_0 r} \psi \tag{2.1}$$

where i is the imaginary unit, h is the Planck constant, ψ is the wavefunction of the electron, t is time, μ is the reduced mass of the electron and the atomic nucleus, q is the elementary charge, Q is the electric charge of the atomic nucleus, ϵ_0 is the vacuum permittivity and r the distance between the electron and the nucleus.

This equation, describing the electronic structure of a hydrogen atom, can be solved in closed form. The result is that the solutions are discrete and correspond to a set of discontinuous energy levels. Larger atoms cannot be solved analytically due to the added electron-electron interactions, but numerical solutions — confirmed by experiments — result in discrete energy levels as well [20].

In matter a very large number of atoms are brought close together changing the electronic structure. At first the energy levels split into several new ones and as more atoms are added the number of levels becomes so large that they can be thought to merge into continuous bands of allowed energies. However, gaps of forbidden energies (i.e. energies that do not correspond to any standing wave solutions) remain [20].

In a crystal atoms are ordered in a distinct repeating arrangement, which — assuming that electron-electron interactions can be neglected — results in that the wave function has the form

$$\psi(\bar{k}, \bar{r}) = e^{i \cdot \bar{k} \cdot \bar{r}} \cdot U(\bar{k}, \bar{r}) \tag{2.2}$$

where $U(\bar{k}, \bar{r})$ is a lattice periodical function that depends on the repeating arrangement of atoms, $\bar{k}$ is the wave vector of the electron wave, and $\bar{r}$ is the position vector. The importance of this Bloch wave solution is that at equilibrium electrons are delocalized across the entire

crystal structure [21].

Bloch waves are not applicable to disordered materials as there is no long range order. In this case electrons are understood to be localized around a few atoms [22].

Both electric and optical properties of materials result from their electronic band structure. For example, semiconductors and insulators are materials where electrons have filled the highest occupied energy band completely whereas in metals this band is only partially filled [23].

2.2 Electron Transport in Solids

When modelling charge transport in crystalline matter, an electron can be thought of as a localized wave packet that is governed by semiclassical equations of motion [21]

$$\frac{\partial \bar{r}}{\partial t} = \bar{v}(\bar{k}) = \frac{2\pi}{h} \cdot \frac{\partial E(\bar{k})}{\partial \bar{k}} \tag{2.3}$$

$$\frac{\partial \bar{k}}{\partial t} = -\frac{2\pi q}{h} \cdot \left(\bar{E}_{el} + \frac{\bar{v}(\bar{k})}{c} \times \bar{H} \right) \tag{2.4}$$

where $\bar{r}$ is the position vector, t is time, $\bar{v}(\bar{k})$ is the group velocity of the wave packet, E is energy, $\bar{k}$ is the wave vector, q is the elementray charge, $\bar{E}_{el}$ is electric field, c is the speed of light and $\bar{H}$ the magnetic field.

The equations describe a classical wave packet; the only quantum mechanical part comes from the $\bar{k}$ dependence of the energy E. Bloch's theorem states that wave functions are unique only to the first Brillouin zone meaning that both wave functions and energy levels are periodic to the reciprocal lattice. Hence the electron velocity (group velocity of the wave packet) is limited and can even be opposite to the electrostatic force acting on it. Net flow of electrons is calculated by integrating the product of state occupation and state velocity over all the electron states in the system. Due to the periodicity of energies the integral for full bands is always zero (the integral of the gradient of a periodic function over a full period is always zero) meaning that full energy bands do not contribute to electric current at all [21].

Electron transport in disordered materials is considered to occur through electron hopping between localized states where the energy difference of the states has a major effect on hopping probability [22]. Because an electron cannot transfer to a state that is already occupied and a hop to a state with much larger energy is highly improbable, the hopping model also results in electric conduction being determined by electrons in partially filled energy bands.

In semiconductors there are two partially filled bands: the conduction band has the higher energy and it is mostly empty whereas the lower energy valence band is almost full of electrons. The valence band conduction can be simplified by tracking the movement of electron vacancies called holes instead of electrons. The behaviour of these imaginary particles is identical to positively charged real particles [23].

The essential results of solid state electron transport theory described here are that only some electrons contribute to net electric current and that electrons can be modelled to move

as localized wave packets. This picture is used in this report to justify modelling electrons and holes as classical particles instead of waves.

2.3 Density of Electron States in a Semiconductor

The number of electrons in a given system depends on the number of electron states and the probability of electrons occupying these states. The number of states should properly be calculated from the Schrödinger equation but solid state textbooks have a way to obtain an approximation [23] by assuming that electrons are free to move inside the crystal.

First it is assumed that the crystal is a cube with an edge length L and that the electron wavefunction falls to zero at the boundaries. This limits the wavenumbers to

$$k_x = \frac{2\pi n}{L} \tag{2.5}$$

where n is an integer and k_x is the wave number (amplitude of the wave vector component) in the x-direction.

The previous equation applies to each cartesian component of the wavenumber. The number of allowed states that have an absolute wavenumber value between k and $k + dk$ is

$$g'(k)dk = \frac{L^3 k^2}{2\pi^2} dk \tag{2.6}$$

Near the band minimum or maximum (relevant energies for semiconductors) the relationship between wavenumber k and energy E can be approximated as a parabola

$$E(k) \approx \frac{1}{2} \cdot \frac{\partial^2 E}{\partial k^2}(k = 0) \cdot k^2 + E(k = 0) \tag{2.7}$$

where the prefactor is the curvature of the parabola. Inserting $k = \frac{2\pi}{h} p$ into the second partial derivative yields

$$\frac{\partial^2 E}{\partial k^2} = \frac{h^2}{4\pi^2} \cdot \frac{\partial^2 E}{\partial p^2} = \frac{h^2}{4\pi^2 m_{eff}} \tag{2.8}$$

where the last equals sign results from the kinetic energy of a classical particle $E = \frac{p^2}{2m}$ thus defining the the effective mass of the electron m_{eff}.

Solving k from the last two equations and inserting it into the expression for density of states gives

$$g'(E)dE = g'(k)dk \Leftrightarrow g'(E) = g'(k)\frac{dk}{dE} = \frac{L^3}{4\pi^2} \cdot \left(\frac{8\pi^2 m_{eff}}{h^2}\right)^{\frac{3}{2}} \cdot \sqrt{E} \tag{2.9}$$

This density of states is for the entire crystal so it must be divided by volume in order to obtain the density of states per unit volume. Also, classical quantum mechanics does not account for spin, which is a relativistic property. This can be corrected by multiplying the final density of states by two corresponding to the two possible electron spin states.

$$g(E) = \frac{2g'(E)}{L^3} = \frac{1}{2\pi^2} \cdot \left(\frac{8\pi^2 m_{eff}}{h^2} \right)^{\frac{3}{2}} \cdot \sqrt{E} \tag{2.10}$$

The importance of this equation is that now density of states near band minima or maxima can be approximated using the effective mass m_{eff} which is obtained from the curvature of the band.

2.4 Electron Statistics, Free Energy and Charge Carrier Concentrations

Based on fundamental postulates in statistical physics and applying the Pauli exclusion principle (which states that only one electron can occupy a given quantum state at a time), one can show that the probability of an electron occupying an energy state is given by the Fermi-Dirac statistics [24]

$$f(E) = \frac{1}{e^{\frac{E-E_F}{k_B T}} + 1} \tag{2.11}$$

where E is the energy of the state, E_F is the Fermi level, k_B is the Boltzmann constant and T is the absolute temperature.

The Fermi level is the same as the chemical potential of electrons, which is defined as the energy that is added to or subtracted from the system by the addition or subtraction of one electron. It is also called free energy because the change in energy of the system is the same regardless of the energy of the individual electron added or removed and hence is the amount of energy freed — or carried away — by the removal of an electron from the system. Note that in electrochemistry it is called electrochemical potential because conceptually it can be divided into chemical and electrostatic parts [25].

Experimentally differences in electron free energies between two points can be measured as a voltage

$$V = \frac{\Delta E_F}{q} \tag{2.12}$$

where V is voltage and q is the elementary charge.

It should also be noted that free energy is only defined for a system in equilibrium whereas one is mostly interested in non-equilibrium systems where net flows of energy or particles are present. The solution to this contradiction is that thermal motion is thought to occur in very fast time scales compared to other processes allowing one to reason that any differences to equilibrium statistics are small enough to be negligible. Thus one defines a quasi-equilibrium condition where equilibrium statistics can be used locally and separately for conduction and valence bands.

The number of electrons in the conduction band can be calculated by integrating the product of the density of states and occupation probability across all the conduction band states

$$n = \int_{E_C}^{\infty} g(E - E_C) \cdot f(E - E_C)\, d(E - E_C) \tag{2.13}$$

Integrating the Fermi-Dirac function cannot be done analytically but when the Fermi level is significantly below the conduction band (i.e. $E - E_F \gg 0$) one can approximate the Fermi-Dirac function with the Boltzmann distribution

$$f(E) = \frac{1}{e^{\frac{E-E_F}{k_B T}} + 1} \approx \frac{1}{e^{\frac{E-E_F}{k_B T}}} = e^{\frac{E_F - E}{k_B T}} \tag{2.14}$$

Performing the integration gives

$$\begin{aligned} n &= \int_{E_C}^{\infty} \frac{1}{2\pi^2} \cdot \left(\frac{8\pi^2 m_{eff}}{h^2}\right)^{\frac{3}{2}} \cdot \sqrt{E - E_C} \cdot e^{\frac{E_F - E + E_C}{k_B T}}\, d(E - E_C) \\ &= \frac{1}{2\pi^2} \cdot \left(\frac{8\pi^2 m_{eff}}{h^2}\right)^{\frac{3}{2}} \cdot \frac{\sqrt{\pi}}{2} \cdot (k_B T)^{\frac{3}{2}} \cdot e^{\frac{E_F - E_C}{k_B T}} \\ &= 2 \cdot \left(\frac{2\pi m_{eff} k_B T}{h^2}\right)^{\frac{3}{2}} \cdot e^{\frac{E_F - E_C}{k_B T}} \end{aligned} \tag{2.15}$$

The coefficient in front of the exponential term is called the effective conduction band density of states N_C.

$$N_C = 2 \cdot \left(\frac{2\pi m_{eff} k_B T}{h^2}\right)^{\frac{3}{2}} \tag{2.16}$$

For holes in the valence band the calculation is almost the same

$$\begin{aligned} p &= \int_{-\infty}^{E_V} g(E - E_V) \cdot (1 - f(E - E_V))\; d(E - E_V) \\ &= N_V \cdot e^{\frac{E_V - E_F}{k_B T}} \end{aligned} \tag{2.17}$$

where p is the number density (concentration) of holes and N_V is the effective valence band density of states

$$N_V = 2 \cdot \left(\frac{2\pi m_{eff,p} k_B T}{h^2}\right)^{\frac{3}{2}} \tag{2.18}$$

Charge carrier concentration can also be expressed in terms of equilibrium concentrations

$$n = N_C \cdot e^{\frac{E_F - E_C}{k_B T}} = n_{eq} \cdot e^{\frac{E_F - E_{F,eq}}{k_B T}} \tag{2.19}$$

$$p = N_V \cdot e^{\frac{E_V - E_F}{k_B T}} = p_{eq} \cdot e^{\frac{-E_F + E_{F,eq}}{k_B T}} \tag{2.20}$$

where

$$n_{eq} = N_C \cdot e^{\frac{E_{F,eq} - E_C}{k_B T}} \tag{2.21}$$

$$p_{eq} = N_V \cdot e^{\frac{E_V - E_{F,eq}}{k_B T}} \tag{2.22}$$

$E_{F,eq}$ is the Fermi level at equilibrium. The advantage of this formulation is that by setting the zero of energy the same as the equilibrium Fermi level one only has to specify the equilibrium carrier concentrations as opposed to conduction and valence band levels and densities of state in order to calculate the Fermi levels.

$$\frac{E_{F,n} - E_{F,eq}}{q} = \frac{k_B T}{q} \cdot \ln\left(\frac{n}{n_{eq}}\right) \tag{2.23}$$

$$\frac{E_{F,eq} - E_{F,p}}{q} = \frac{k_B T}{q} \cdot \ln\left(\frac{p}{p_{eq}}\right) \tag{2.24}$$

where $E_{F,n}$ and $E_{F,p}$ are the conduction and valence band (quasi-)Fermi levels.

2.5 The Continuity Equation

Stating that particles of any type are created or destroyed in a given (arbitrary) volume only by specific sources or sinks leads to the conclusion that the change in the number of particles in the volume must correspond to these source (or sink) terms as well as particle in- or outflow through the surfaces of the volume. Using Gauss' divergence theorem one can state this mathematically as a differential equation for an infitely small point in space.

$$\frac{\partial n}{\partial t} = -\nabla \cdot j + S \tag{2.25}$$

where n is the number density of the particles in question, t is time, j the flux of the particles and S is the source or sink term. Note that from now on electrons and other charged patricles will be modelled as classical particles with well defined positions instead of waves.

In semiconductors charged particles move both due to drift caused by electric fields and due to diffusion caused by concentration differences. Magnetic fields will also affect moving charges, but in this report these fields are always assumed to be zero.

When placed under the influence of an electric field in free space, a charged particle accelerates indefinitely ultimately reaching relativistic speeds. Inside matter, however, the particle will collide with other particles (atoms, ions or electrons) and will move at a finite speed called drift velocity. At low electric field values, drift velocity is proportional to electric field and a coefficient called mobility. [26]

$$j_{drift} = zn\mu \cdot (-\nabla\varphi) \tag{2.26}$$

where z is the charge number and μ the electrical mobility of the particle. Here electric field has been expressed as the negative gradient of electric potential φ.

Thermal motion causes particles to move around in matter randomly. Einstein showed [27] that this random movement can be approximated by

$$j_{diffusion} = -D\nabla n \tag{2.27}$$

where D is the diffusion coefficient.

Einstein also showed that as long as the energy of the particles is described by the Boltzmann distribution, the diffusion coefficient can be expressed using the particle mobility, temperature and natural constants [27].

$$D = \frac{k_B T}{q} \cdot \mu \tag{2.28}$$

where k_B is the Boltzmann constant, T is temperature and q is the elementary charge.

Chapter 3

Photovoltaic Devices and Characterization Techniques

A photovoltaic cell is a device that converts electromagnetic energy into electric energy through the photovoltaic effect. In this chapter the underlying physics of photovoltaics is briefly summarized and important characterization techniques used in this report are discussed.

3.1 Photovoltaic Effect

When electromagnetic radiation of suitable energy is absorbed by a piece of material, there is a chance that an electron is excited from its initial state to a one with higher energy leaving behind a vacancy called a hole. As the electron and hole have opposite electric charge, they are bound together through electrostatic interaction. In some materials the relative permittivity is high enough that the bound state called an exciton will dissociate into a free electron and hole almost immediately due to thermal motion, in others this requires a nearby vacant state of lower energy for the electron or hole to transfer into. In any case the dissociated charges must prefer to move into opposite directions due to some energetic asymmetry that has been built into the cell in order to collect electric current. Without this asymmetry electrons will eventually recombine with the holes and no electrical energy can be gathered [28]. An illustration for the photovoltaic effect in given in figure 3-1.

3.2 I-V and J-V Curves

As solar cells are made to produce as much electric power as possible from available electromagnetic radiation, the most important measurement of cell performance is its current-voltage dependence or I-V curve. The cell is placed under a lamp and the current given by the cell is measured as reverse voltage is varied. Both current and voltage given by the cell depend on cell temperature as well as the incident light intensity and spectrum. Therefore measure-

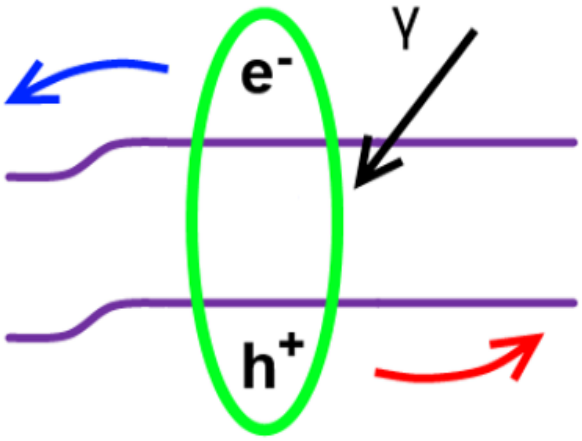

Figure 3-1: Illustration of the principle behind photovoltaic devices. An incoming photon (γ) excites an electron (e^-) from a lower energy state to higher one leaving a behind a hole (h^+). Initially the electron and hole form a bound state called an exciton which will break up either spontaneously or due to energetic asymmetry (not shown). Finally a type of built-in asymmetry in the cell (band bending on the left) will cause the free electron and hole to preferentially move in different directions leading to electric current.

ments are usually made in — or normalized to — Standard Reporting Conditions (SRC) with a temperature of 25°C, Air Mass 1.5 G spectrum and incident power intensity 1000 W/m^2. This intensity and spectrum is also commonly called 1 sun as it is close to the solar radiation hitting the surface of Earth at a latitude of 48° on a clear day at solar noon (the power density is rounded to 1000 W/m^2 for convenience) [29].

Photocurrent is directly proportional to the area of the cell. Current density is therefore a better value than current for characterizing the performance of a particular cell design and is usually given instead of current. In this case the plot is called the J-V curve. An example J-V curve is given in figure 3-2.

A number of values are calculated from the I-V curve. Open circuit voltage V_{oc} is the value of reverse bias applied to the cell when there is no current. Short circuit current I_{sc} (or current density J_{sc}) is the value of current with no reverse bias.

Fill factor FF is defined by

$$FF = \frac{I_{mpp}V_{mpp}}{I_{sc}V_{oc}} \tag{3.1}$$

where I_{mpp} and V_{mpp} are the current density and voltage at the maximum power point. This value describes the squareness of the I-V curve. In general low fill factor indicates high internal resistance in the cell.

The power conversion efficiency PCE or η_{PC} of the cell is

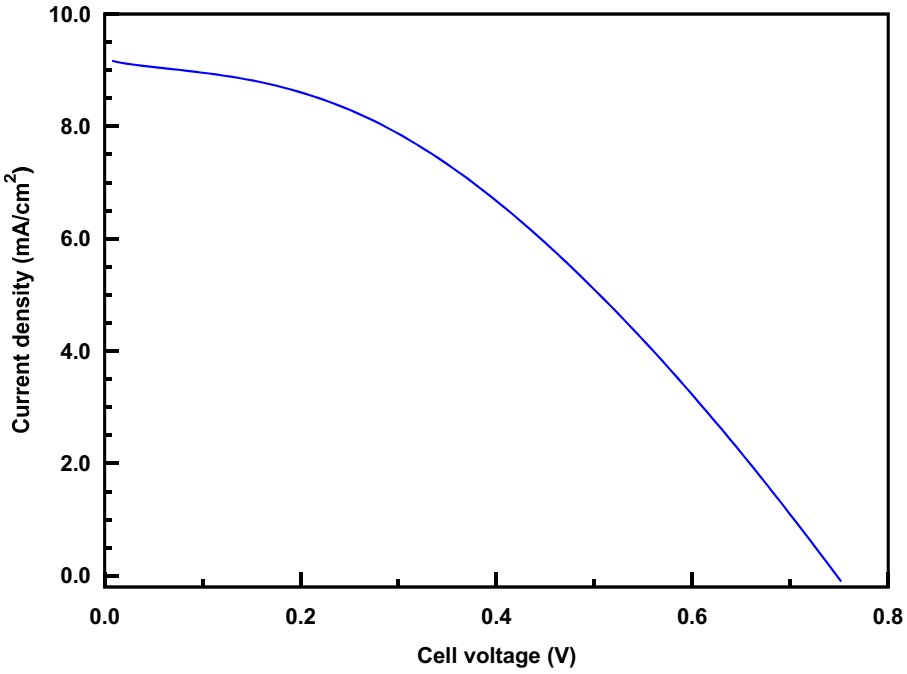

Figure 3-2: An example experimental J-V curve of a dye-sensitized solar cell.

$$\eta_{PC} = \frac{I_{mpp}V_{mpp}}{P} = \frac{I_{sc}V_{oc}FF}{P} \tag{3.2}$$

where P is the power density ($\mathrm{W/m^2}$) of the incident light.

Most solar cell I-V curves can be described by an equation describing an electrical circuit where a current source is connected in parallel with a diode and in series with a resistor [28].

$$I_{cell} = I_{ph} - I_D \cdot e^{\frac{q(V_{cell}+R_s I_{cell})}{mk_B T}} \tag{3.3}$$

where I_{cell} is cell current, I_{ph} is the photogeneration current of the cell, q is the elementary charge, V_{cell} cell voltage, R_s reistance of the resistor, k_B the Boltzmann constant, T cell temperature and m the cell nonideality factor. Although more detailed physical models give better agreement with experiment, this equation is often used to calculate the nonideality factor, which may give some information about the underlying physical processes of recombination. For example, the equation predicts that increasing light intensity by a factor of ten will increase open circuit voltage by $m \cdot 59$ mV.

Although the I-V curves and power conversion efficiencies at different lighting and temperature conditions contain all the necessary information about device performance to an end user, they do not provide enough information to someone seeking to improve the device. The first steps towards addressing this issue are taken in the next section.

3.3 Process Efficiencies in a Solar Cell

As stated before a photovoltaic device requires light to create free electric charges and some type of asymmetry to drive these charges into one direction. If this asymmetry is not strong enough some charges will recombine by falling back into their initial state. In an ideal device all incident photons will be absorbed by the correct material, all absorbed photons will create free charges and all free charges are collected. Therefore the current efficiency, also known as the external quantum efficiency (EQE) or incident photon to collected electron efficiency (IPCE) can be divided into three parts: light harvesting, absorbed photon to charge generation and charge collection efficiencies.

$$IPCE = \frac{I_{cell}}{qA_{cell}\phi} = \eta_{LH} \cdot \eta_{APCG} \cdot \eta_{COL} \tag{3.4}$$

where I_{cell} is the cell current, q the elementary charge, A_{cell} cell area, ϕ the incident photon flux and η_{LH}, η_{APCG} and η_{COL} are the light harvesting, absorbed photon to charge generation and charge collection efficiencies, respectively. In dye solar cells free charge generation occurs through electron injection into a lower energy level (see next chapter) so absorbed photon to charge generation efficiency is usually called the injection efficiency η_{INJ} [18]. Note that typically IPCE (and EQE) are understood to be given at short circuit unless otherwise stated, although the numbers can be defined anywhere on the I-V curve. This convention is also used elsewhere in this report.

Light harvesting and free charge generation depend either entirely or heavily on the optical properties of the cell which are not the focus of this study. As such these two are referred collectively as the charge generation efficiency in this report. Charge collection efficiency, on the other hand, is the target of this work. Unfortunately there is no simple and reliable way to measure charge generation and collection efficiencies separetely meaning that charge transport models must be used to discern between the them. Most of the modelling work in this study is done to achieve this.

In order to separate charge generation and collection, as well as potential different recombination processes from each other, one must be able to use measurement data to obtain the correct parameter values of the model used to describe charge transport. Thus the problem is not only to find the correct model, but to also find a way to solve the inverse problem associated with it.

Overall power conversion efficiency depends not only on the current efficiency but also on the voltage efficiency. Ideally all the energy of every incoming photon can be exploited but in practice this is not the case. If an electron is excited beyond the lower limit of the conduction band, the collisions caused by thermal motion will cause the electron to drop into the lowest unoccupied conduction band state very quickly. The same happens for holes in the valence band with the difference that holes move up in electron energy as they have the opposite electric charge. When this thermalization is combined with unavoidable radiative losses caused by free electrons recombining with free holes, the result is that any photon energy exceeding the absorber band gap cannot be utilized using a conventional solar cell [28]. Therefore one

can write the voltage efficiency of the solar cell as

$$\eta_{voltage} = \frac{qV_{cell}}{E_{bg}} \cdot \frac{E_{bg}}{E_{photon}} \tag{3.5}$$

where V_{cell} is the cell voltage, E_{bg} absorber band gap and E_{photon} the average energy of the incident photons. The band gap depends on the absorber material and the average photon energy on the spectrum of incident light. Thus these constants do not need to be measured from a full device.

Combining the current and voltage efficiencies yields the overall power conversion efficiency

$$\eta_{PC} = IPCE \cdot \eta_{voltage} = \eta_{LH} \cdot \eta_{APCG} \cdot \eta_{COL} \cdot \frac{qV_{cell}}{E_{bg}} \cdot \frac{E_{bg}}{E_{photon}} \tag{3.6}$$

3.4 Impedance Spectroscopy

Impedance spectroscopy is a measurement where a small perturbation (voltage or current) is applied to the cell and the resulting output (current or voltage) is measured. In its most common form a sinusoidal perturbing signal is applied on top of a steady-state bias. Scanning across a range of frequencies will then give information about the behaviour of the cell. Impedance itself is defined as the transfer function linking current and voltage of a linear time-invariant system [30].

$$Z(\omega) = \frac{V_{AC}(\omega)}{I_{AC}(\omega)} \tag{3.7}$$

where Z is impedance, ω is the angular frequency of the perturbation, V_{AC} is the alternating voltage and I_{AC} the alternating current. Physically impedance measurement results consist of two values: the first is the ratio of the signal and perturbation amplitudes and the second is the phase shift between the signals. Usually impedance as well as alternating currents and voltages are given as complex numbers [30]. For a short introduction in using complex numbers to represent sinusoidal signals, see appendix A. A dye solar cell impedance spectrum is described in appendix B.

Most systems, particularly electrochemical ones, are not linear and therefore the output signal in equation 3.7 refers only to the linear part of the full signal. This is not a problem if the signal is measured using a frequency response analyser which can implement a type of Fourier analysis to isolate only the linear part of the output signal [30].

The output signal S of a non-linear system can be represented as a Fourier series plus a noise term N [30, 31]

$$S = A_0 \sin(\omega t + \phi_0) + \sum_{k=1}^{\infty} (A_k \sin(k\omega t + \phi_k)) + N \tag{3.8}$$

where the sum is the non-linear part of the signal.

Multiplying the output by the input signal and integrating the product over one or multiple

full cycles yields the linear part of the output signal S because as the integration time increases the integral of noise approaches zero and the orthogonality of sines and cosines yields

$$\begin{aligned}
&\int_0^{n\cdot\frac{2\pi}{\omega}} \sin(m\omega t)\cdot\sin(k\omega t+\phi_k)\,dt \\
=&\int_0^{n\cdot\frac{2\pi}{\omega}} \sin(m\omega t)\cdot\sin(k\omega t)\cdot\cos(\phi_k)\,dt + \int_0^{n\cdot\frac{2\pi}{\omega}} \sin(m\omega t)\cdot\cos(k\omega t)\cdot\sin(\phi_k)\,dt \\
=&0 \quad \text{, when } m\neq k
\end{aligned} \tag{3.9}$$

where n, m and k are integers.

The importance of rejecting the non-linear part of the signal is that frequency-based measurments can be mathematically described using linear or linearized equations as the measurement itself rejects all higher harmonics caused by non-linearity of the response. This greatly simplifies modelling and is a reason for choosing to use impedance spectroscopy over transient methods — which are only approximately linear with small perturbations — in this report.

Chapter 4

Dye-Sensitized Solar Cell Device Model

4.1 Dye-Sensitized Solar Cell

A dye-sensitized solar cell (DSSC) consists of a semiconductor, dye and a hole conducting layer on a suitable mechanical support. Incoming photons are absorbed by dye molecules attached to the surface of the semiconductor. The energy of the photon excites an electron from an occupied molecular orbital to a higher unoccupied one. The electron is then injected from the dye into the conduction band of the semiconductor, from which it can be collected into an external circuit. The oxidized dye molecule is regenerated by an electron transfer from the hole conductor. After the electron has moved through the external circuit, it reduces the hole conductor [32].

Figure 4.1 shows the layers in a typical dye solar cell. The cell is built on a glass sheet coated with fluorine-doped tin oxide (FTO). Nanoporous titanium dioxide acts as the semiconductor and is sensitized by a ruthenium complex dye. The combination of the semiconductor and dye is called the photoelectrode (PE). A reduction-oxidation couple (typically iodide/tri-iodide) in organic solvent (typically acetonitrile or similar) acts as the hole conductor. The porosity of the semiconductor increases the effective surface area by several orders of magnitude enabling more dye molecules to attach to its surface. Although this enhances short circuit current, it also increases electron back reaction into the electrolyte. One of the remarkable features of the dye solar cell is that back reaction can be suppressed so efficiently that a high surface area junction is actually desirable. Another FTO glass sheet coated with platinum is used as the counter electrode (CE) to return the electron from the external current into the cell [32].

An energy scheme for a dye-sensitized solar cell is also given in figure 4.1. A photon excites an electron from the highest occupied molecular orbital (HOMO) S_0 to the lowest unoccupied molecular orbital (LUMO) S^* (1). The electron is then injected into the conduction band (CB) of the semiconductor with a lifetime of femto- to picoseconds (2). The electron could also return

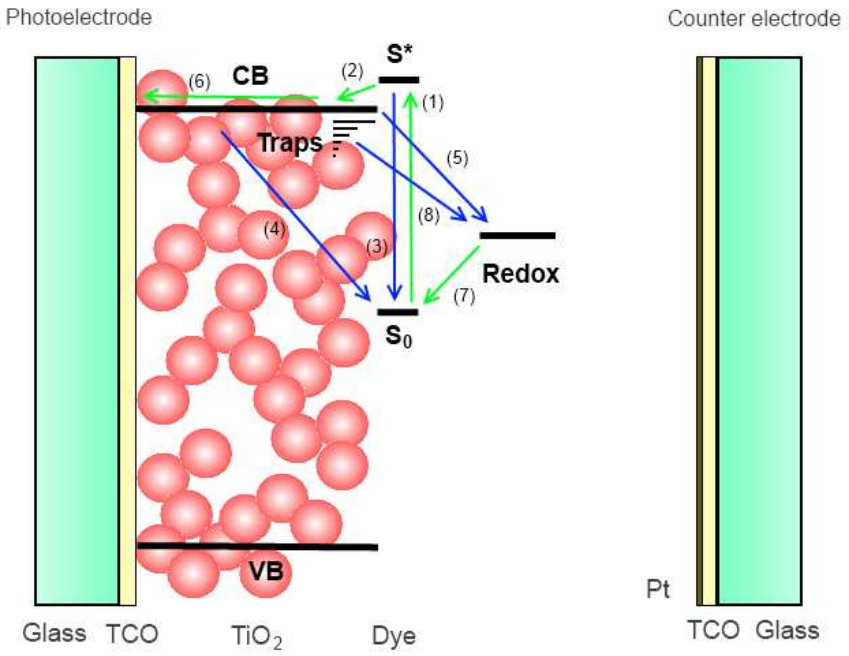

Figure 4-1: An illustration of the layers in a typical dye-sensitized solar cell and an energy scheme. The cell is built by depositing a nanoporous titanium dioxide layer on glass with some transparent conductive oxide (TCO). Dye is adsorbed on the surface of the nanoparticles and the entire cell filled with a redox electrolyte. Another TCO glass piece with additional platinum catalyst acts as a counter electrode. Light is absorbed by the dye exciting an electron from a ground state S_0 to an excited state S^* (1). The electron is then injected into the conduction band (CB) of the TiO_2 (2) before it can fall back to the original state (3). A conduction band electron may recombine with an excited dye molecule (4) or directly with an oxidized redox ion (5). A possible additional recombination pathway is from the localized (trap) states below conduction band into the electrolyte (8). Power is generated when electrons diffuse to the contact (6) and the reduced redox ion regenerates the dye (7).

to its original state (3) but this radiative recombination takes several nanoseconds hence making injection much more probable. The electron can also be captured from the semiconductor by an oxidized dye species (4) or the electrolyte (5) before it can diffuse into the external circuit (6). The dye molecule gets an electron from the electrolyte (7) in just pico- to nanoseconds whereas both transport into the external circuit and recombination from the semiconductor occur at a timescale of microseconds to seconds. Recapture from the semiconductor is therefore considered the most important recombination mechanism in a dye-sensitized solar cell. Another possibility is recombination from localized states (traps) beneath the conduction band (8) [32].

The electrons present in the semiconductor increase the electrochemical potential (also known as quasi-Fermi level) in the material. The difference of this potential and the redox potential of the electrolyte is the measured cell voltage. The band gap of the common ruthenium dyes is about 1.7 eV, the TiO_2 conduction band is about 0.2 eV lower than the dye LUMO level and the energy difference between the iodine electrolyte and the ground state of the dye is about 0.6-0.7 eV. These values give a maximum open circuit voltage of about 0.8-0.9 V [32, 33]. In practice, however, open circuit voltages are somewhat lower due to electron recombination from the semiconductor and/or trap states. In principle one would prefer for the LUMO and redox levels to be closer to the conduction band bottom and dye HOMO levels, respectively. However, the energy differences are necessary for the injection and regeneration reactions to dominate as lower driving forces result in slower reactions. Moreover, the energy scheme in figure 4.1 is more complicated in reality as iodide/tri-iodide redox couple involves the transfer of two electrons and thus the energy level relevant to regeneration is the redox potential of iodine radical/iodide, which is considerably lower than the redox potential of the overall couple [15].

Laboratory scale devices can be made up to 10% efficiencies [34] although achieving this level of performance requires optimizations that are too impractical to be used routinely. According to the solar cell record efficiency listings in the journal Progress in Photovoltaics, the current verified champion cell has an efficiency of 11.9% [35].

4.2 Dye Solar Cell Device Model

A dye solar cell is a photoelectrochemical device meaning that to fully understand its operation one has to model interactions with light, chemical reactions as well as movement of electrons. This study concentrates on electrical measurements and thus optical and chemical models are given less attention. The standard configuration of sensitized titanium dioxide on fluorine-doped tin oxide coated glass with iodide/tri-iodide redox couple in organic solvent is assumed as this corresponds to the experimental work done in chapter 5.

In the following sections an electrical model for the dye solar cell is developed. The focus is on a device level picture and details and effects that cannot be seen with electrical measurements are ignored.

The model can perhaps be easier to understand using a conceptual equivalent circuit that represents the different physical processes as ideal electric circuit elements. This conceptual

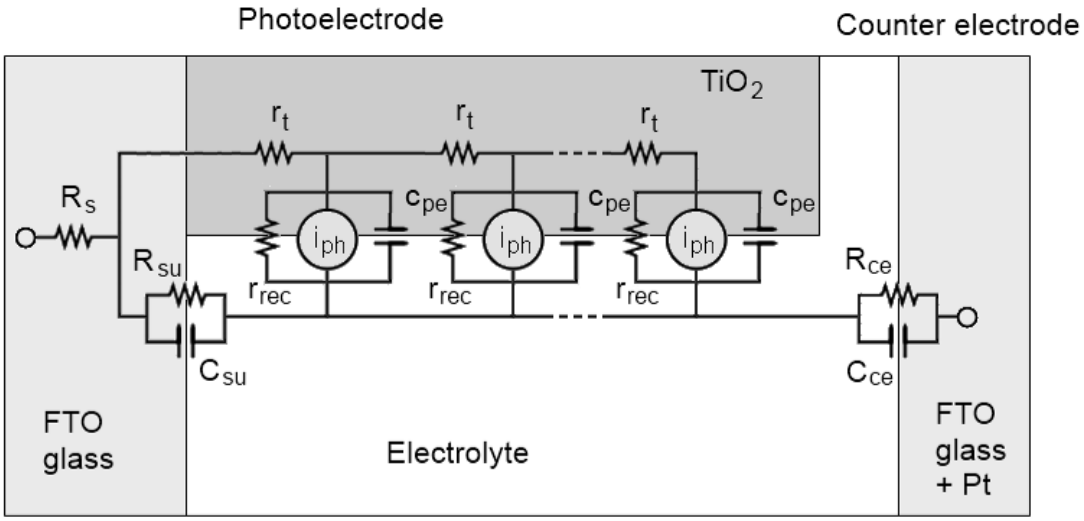

Figure 4-2: Conceptual dye solar cell equivalent circuit. Sheet resistance of the FTO glass substrate is treated as a resistor R_s. Recombination from the titanium dioxide is treated as a distributed resistance r_{rec}. Diffusion (r_t), recombination from the substrate (R_{su}) and counter electrode overpotential (R_{ce}) are also treated as resistors. Trapping (c_{pe}) as well as counter electrode and substrate interfacial capacitances (C_{ce} and C_{su}) are treated as simple capacitors. Light absorption and charge generation is modeled as a current source (i_{ph}).

circuit is given shown in figure 4-2.

4.2.1 The Continuity Equations

Since one is ultimately interested in the current the cell produces as function of applied voltage, the treatment will start with the conduction band (or free) electrons of the semiconductor following the scheme first presented by Soedergren et al. [9]. The semiconductor is treated a quasi-homogeneous layer in contact with the electrolyte: porosity, grain boundaries or band bending effects are neglected although they may be considered to be implicitly included in the parameters. For example, poor electrical connections between particles and higher porosity would lead to a smaller effective diffusion coefficient.

The continuity equation for conduction band electrons is

$$\frac{\partial n_c}{\partial t} = -\nabla \cdot j + G - R - T_c \tag{4.1}$$

where n_c is conduction band electron density, t is time and j electron flux. Electron injection (generation, G) from the dye is the source term. Recombination (R) into the electrolyte and trapping (T_c) into the localized states are sink terms. Recombination of electrons with the oxidized dye molecules will be taken into account in the generation term G, as shown below in the recombination and dye regeneration section.

Conventional wisdom holds that electron transport in the conduction band occurs by diffu-

sion as long range electric fields are screened by the electrolyte ions that surround the semiconductor nanoparticles (see figure 4.1) [9, 18]. Peter also calculated the electric potential change inside the particles assuming moderate N-type doping and concluded that band bending is negligible [36].

The flux is therefore

$$j = -D_c \cdot \frac{\partial n_c}{\partial x} \tag{4.2}$$

where D_c is the free electron diffusion coefficient. For the sake of simplicity the coefficient is assumed to be independent of position or electron density. This assumption is also backed by experiment [17].

Transport of ions in the electrolyte is also thought to occur by diffusion as the short distances between electrodes preclude convection and theoretical calculations by Papageorgiou et al. [37] have indicated that the electrochemically inactive ions effectively screen the electric field making drift negligible at all but very high current densities.

The continuity equation for the oxidized redox ion species is

$$\frac{\partial c_{ox}}{\partial t} = D_{ox} \cdot \frac{\partial^2 c_{ox}}{\partial x^2} + S_{ox}G - S_{ox}R \tag{4.3}$$

where c_{ox} is the oxidized ion concentration, D_{ox} is the diffusion coefficient and S_{ox} the number of ions reduced or oxidized by one transferred electron. For example, two electrons are needed to reduce one tri-iodide ion into three iodide ions so S_{ox} for tri-iodide is 0.5.

For the reduced species the continuity equation is

$$\frac{\partial c_{red}}{\partial t} = D_{red} \cdot \frac{\partial^2 c_{red}}{\partial x^2} - S_{red}G + S_{red}R \tag{4.4}$$

where c_{red} is the reduced species concentration, D_{red} is the diffusion coefficient and S_{red} the number of ions reduced or oxidized by one transferred ion. For example, two electrons are needed to oxidize three iodide ions into one tri-iodide ion so S_{red} for iodide is 1.5.

As shown in figure 4.1 electrolyte both fills the pores of the photoelectrode and the gap between the electrodes. The above continuity equations describe transport in the porous area whereas in the free area the source and sink terms are zero.

$$\frac{\partial c_{ox,F}}{\partial t} = D_{ox,F} \cdot \frac{\partial^2 c_{ox,F}}{\partial x^2} \tag{4.5}$$

$$\frac{\partial c_{red,F}}{\partial t} = D_{red,F} \cdot \frac{\partial^2 c_{red,F}}{\partial x^2} \tag{4.6}$$

where the subsript F denotes the free electrolyte layer.

Note that trapping of electrons into surface states should be matched by the same amount of charge accumulating on the electrolyte side meaning that capacitive terms should be added to the redox ion continuity equations as well. The justification for omitting these is that ions have much higher concentrations than electrons and hence surface capacitance effects should

be very small. For example, tri-iodide has usually the smallest concentration in the electrolyte at about $2 \cdot 10^{25}$ m^{-3} whereas measurements of total electron concentration in the TiO_2 film at open circuit give values of about $1 \cdot 10^{24}$ m^{-3} [38].

4.2.2 Light Absorption and Injection

As with any other photovoltaic device, a dye-sensitized solar cell works by absorbing photons of suitable energy and converts them into free electrons. For this to happen, the incoming photon must be absorbed by the dye. However, all cells must have many other components that necessarily absorb some of the available energy. Firstly, light must pass through the cell sealing materials and mechanical supports (typically glass or plastic). Secondly, in most configurations light will enter the cell after penetrating a transparent conductive layer (TCO) that is used to collect cell current. As electrical conductivity and transparency in the visible region tend to be mutually exclusive properties, transparency is necessarily compromised to reduce resistive losses. Another absorbing medium in the cell is the electrolyte which fills the photoelectrode pores.

Typically the optical model coupled to the diffusion equation follows simple Lambert-Beer exponential decay [9, 18], which assumes wavelength-independent absorption and neglects any scattering in the layers. The reasons for this choice are simplicity of equations, narrow band illumination using LEDs in common measurements and the lack of any strongly scattering materials in most (but not all [34]) cells.

$$\phi_{TiO_2} = \phi T_{subst} e^{\alpha_t x + \sigma} \tag{4.7}$$

where ϕ_{TiO_2} is the photon flux inside the photoelectrode, ϕ is the photon flux directly outside the cell, T_{subst} is the transparency of the supporting structure (seals, glass, and TCO, additionally electrolyte and catalyst if light enters from the counter electrode side), x is the position in the film and α_t is the total extinction coefficient of the sensitized and electrolyte filled film. In the formalism used here α_t also has a sign indicating the direction of illumination: conventional photoelectrode side lighting is presented as a negative α_t. A scaling factor σ is used to normalize light intensity in order to avoid additional prefactors when using counter electrode side illumination.

$$\text{PE side: } \alpha_t < 0, \quad \sigma = 0 \tag{4.8}$$

$$\text{CE side: } \alpha_t > 0, \quad \sigma = \alpha_t d \tag{4.9}$$

where d is the thickness of the titania film.

Once the photon has excited an electron into the LUMO level of the dye, it can then either fall back to the original HOMO level (radiative recombination) or be injected into the conduction band.

In principle one could formulate a physical model for electron injection in a DSSC. However, this study is concerned with electrical properties of the device and any details not captured

by electrical measurements are omitted. In practice it is found that injection is only weakly influenced by electron density in the film [38] thus enabling one to model it as an undetermined constant.

In summary overall photogeneration of free electrons in the semiconductor is modeled as Lambert-Beer exponential decay of light intensity multiplied by absorption coefficient of the dye as well as injection efficiency.

$$G = \alpha_d \eta_{INJ} \eta_{REG} \phi T_{subst} e^{\alpha_t x + \sigma} \tag{4.10}$$

where α_d is dye light extinction coefficient and n_{INJ} electron injection efficiency. Regeneration efficiency n_{REG} is discussed in the recombination section below.

Noting that integrating the generation term over the film thickness gives the total photoinjection current, which is the same as incident photon flux multiplied by the product of light harvesting, injection and regeneration efficiencies, one can simplify the generation term to

$$G = \eta_{LH} \eta_{INJ} \eta_{REG} \phi \cdot \frac{\alpha_t}{e^{\alpha_t d} - 1} \cdot e^{\alpha_t x} \tag{4.11}$$

where η_{LH} is light harvesting efficiency.

Combining the three efficiencies yields overall charge generation efficiency, which simplifies the model in the case where light harvesting, injection and renegeration are assumed to be constant.

$$\eta_{CG} = \eta_{LH} \eta_{INJ} \eta_{REG} \tag{4.12}$$

where η_{CG} is the charge generation efficiency.

4.2.3 Localized States: Trapping

In addition to conduction band states, time dependent electrical measurements give evidence that most of the electrons in the titanium dioxide film in fact occupy localized states between the conduction and valence bands [14, 39]. The nature and origin of these traps is uncertain at present, although Zhu et al. found evidence that traps are located at the nanoparticle surfaces [40]. Katoh et al. [41] also observed a particle size effect in injection studies which they related to trap states giving further evidence of the traps being located on the surface.

Bisquert and Vikhrenko introduced a model where localized electrons are thought to occupy a continuum of exponentially distributed states in equilibrium with the conduction band [10].

The concentration of trapped electrons can be calculated by multiplying the density of trap states with the Fermi-Dirac occupation probability.

$$n_t = \int_{E_V}^{E_C} N_{t,0} e^{\beta_T \cdot \frac{E - E_C}{k_B T}} \cdot \frac{1}{e^{\frac{E - E_F}{k_B T}} + 1} \, dE \tag{4.13}$$

where $N_{t,0}$ is the trap density coefficient, β_T is the trap distribution parameter, E is energy and E_V, E_C and E_F are the valence, conduction and Fermi energy levels, respectively.

The integral can be evaluated analytically if the Fermi-Dirac function is approximated by a step function

$$\begin{aligned} n_t &\approx \int_{E_V}^{E_F} N_{t,0} e^{\beta_T \cdot \frac{E-E_C}{k_B T}} \cdot 1 \, dE + \int_{E_F}^{E_C} N_{t,0} e^{\beta_{T,0} \cdot \frac{E-E_C}{k_B T}} \cdot 0 \, dE \\ &= N_{t,0} \cdot \frac{k_B T}{\beta_T} \cdot \left(e^{\beta_T \cdot \frac{E_F - E_C}{k_B T}} - e^{\beta_T \cdot \frac{E_V - E_C}{k_B T}} \right) \\ &\approx N_{t,0} \cdot \frac{k_B T}{\beta_T} \cdot e^{\beta_T \cdot \frac{E_F - E_C}{k_B T}} = n_{t,eq} e^{\beta_T \cdot \frac{E_F - E_{F,eq}}{k_B T}} \end{aligned} \tag{4.14}$$

where $n_{t,eq}$ is the trapped electron concentrataion at equilibrium and $E_{F,eq}$ is the equilibrium Fermi level.

The conduction band electron concentration is given by

$$n_c = N_C e^{\frac{E_F - E_C}{k_B T}} = n_{c,eq} e^{\frac{E_F - E_{F,eq}}{k_B T}} \tag{4.15}$$

where N_C is the conduction band density of states and $n_{c,eq}$ is the equilibrium conduction band electron concentration.

Assuming that conduction band and trapped electrons are in equilibrium, their concentrations can be described using a common Fermi level and the two last equations can be combined to get

$$n_t = \frac{n_{t,eq}}{n_{c,eq}^{\beta_T}} \cdot n_c^{\beta_T} \tag{4.16}$$

This results in the trapping term

$$T_c = \frac{\partial n_t}{\partial t} = \frac{n_{t,eq} \beta_T}{n_{c,eq}^{\beta_T}} \cdot n_c^{\beta_T - 1} \cdot \frac{\partial n_c}{\partial t} \tag{4.17}$$

4.2.4 Recombination and Dye Regeneration

As stated before, a conduction band electron may recombine with an oxidized redox ion or dye molecule before it has time to travel into the external circuit. Measurements of open circuit voltage against light intensity indicate that this back reaction is a nonlinear function of conduction band electrons which is usually explained as evidence of recombination from the trap states (see previous section) [11].

In principle recombination into the electrolyte from the trap states could be calculated by integrating the product of trapped electron number and reaction rate across the band gap energy,

$$R_T = \int_{E_V}^{E_C} k_{r,t}(E) n_t(E_F, E) \, dE \tag{4.18}$$

where R_T is recombination from trap states, $k_{r,t}(E)$ is trap recombination rate coefficient and

$n_t(E_F, E)$ is the concentration of trapped electrons per energy.

Unfortunately the energy dependence of the recombination rate coefficient $k_{r,t}$ is unknown so in practice the integral cannot be calculated. Bisquert et al. [16] have used Marcus–Gerischer theory to obtain one expression but this theory is only valid for outer sphere redox couples where electron transfer merely distorts chemical bonds instead of breaking them. The iodide/tri-iodide redox couple reactions do involve breaking of bonds so at first it appears that the model is not valid. It is possible that the rate determining step is indeed a suitable reaction but at present the exact recombination pathway is unknown (see below) so for now one must simply accept a phenomenological recombination rate model.

Fortunately experimental evidence indicates that for a large voltage range recombination is well described by a simple power law [11, 18].

$$R \propto (n_c - n_{c,eq})^{\gamma} \tag{4.19}$$

where n_c and $n_{c,eq}$ are the current and equilibrium conduction band electron concentrations. This form is also approximately compatible with the Marcus–Gerischer theory derived by Bisquert et al. discussed above [16].

Back reaction to the electrolyte also requires the presence of oxidized redox ions. The most commonly used iodide/tri-iodide couple actually involves the transfer of two electrons

$$I_3^- + 2e^- \Leftrightarrow 3I^- \tag{4.20}$$

The exact pathway for recombination is presently unclear and in fact even the main electron acceptor species is not known as the iodide/tri-iodide redox couple is formed by elemental iodine capturing an iodide ion [15].

$$I^- + I_2 \Leftrightarrow I_3^- \tag{4.21}$$

Irrespective of whether recombination involves iodine or tri-iodide, the rate seems to be linear with respect to iodine/tri-iodide concentration [15].

$$R = k_{r,c} \cdot \frac{c_{acc}}{c_{acc,eq}} \cdot (n_c - n_{c,eq})^{\gamma} \tag{4.22}$$

where k_r is the recombination rate constant, c_{acc} is the electron acceptor concentration (number of molecules per m^3), $c_{acc,eq}$ equilibrium acceptor concentration, n_c and $n_{c,eq}$ the conduction band electron density at operating conditions and equilibrium, respectively.

In this report tri-iodide is considered to be the electron acceptor. Should one prefer to consider iodine as well one has to account for the tri-iodide formation reaction (equation 4.21). The equilibrium of this reaction is so far to the right side that very little iodine is present in the electrolyte [15]. Therefore tri-iodide concentration is effectively independent of iodide concentration but iodine is not. Using the law of mass action yields

$$c_{I_2} = \frac{c_{I_3^-}}{c_{I^-}} \cdot \frac{1}{K_{I_2}} \Rightarrow \frac{c_{I_2}}{c_{I_2,eq}} = \frac{c_{I_3^-}}{c_{I_{3,eq}^-}} \cdot \frac{c_{I_{eq}^-},}{c_{I^-}} \tag{4.23}$$

where K_{I_2} the equilibrium constant for the reaction.

Dye regeneration by the electrolyte and dye mediated recombination by photogenerated electrons are responsible for the reduction of the oxidized dye molecule. As one does not wish to lose any conduction band electrons to the dye, achieving fast regeneration kinetics is necessary for highly efficient devices. Traditional thinking has been that dye regeneration is 100% efficient in good cells as some cells convert 100% of incident photons (after correcting for substrate transparency) into current in certain conditions [32]. Jennings and coworkers, however, argue that while this may be the case at short circuit, it may not hold when electron density is increased [42]. Assuming that the number of oxidized dye molecules reaches a steady state immediately under electrical perturbation (dye regeneration is too fast to be seen with any electrical measurement [32]), they have derived an expression for regeneration efficiency that is a function of redox ion and electron densities.

$$\eta_{REG} = \frac{k_{REG} c_{red}^{\gamma_{red}}}{k_{REG} c_{red}^{\gamma_{red}} + k_e n_c^{\gamma_e}} \tag{4.24}$$

where n_{REG} is regeneration efficiency, k_{REG} is regeneration rate constant, c_{red} is the reduced ion concentration, k_e dye recombination rate constant and n_c conduction band electron density.

Experimentally Jennings et al. [42] find that the presented model works well at high electron densities but requires an extra recombination pathway at low densities. Anderson et al. also studied regeneration and presented the equation above but without the exponents [43] (more precisely they found the reaction order to be close to three with respect to total electron concentration, which results in a reaction order of one for conduction band electrons when trapped electrons are taken into account). Both works agreed that regeneration can be assumed perfect or close to perfect at high iodide concentrations at short circuit.

In this report the exponents are assumed to be 1 or regeneration efficiency is assumed to be constant.

4.2.5 Counter Electrode Overpotential

Although electron transfer from the counter electrode to the oxidized redox ion is a very fast process when using suitable catalysts, the voltage loss (usually termed overpotential) at this interface is not negligible — at least when mass transport limitations start to play a role at high current densities. Although the overall reaction is the same as given in the recombination section (equation 4.20), the pathway may be different. Here, the model overviewed by Halme et al. [18] is briefly summarized.

The current-overpotential equation for a metallic electrode in the presence of a redox couple [25] is

$$\frac{I_{cell}}{A_{cell}} = i_0 \left(\frac{c_{ox}}{c_{ox,eq}} e^{\beta_{CE} \frac{qV_{CE}}{k_B T}} - \frac{c_{red}}{c_{red,eq}} e^{-(1-\beta_{CE}) \frac{qV_{CE}}{k_B T}} \right) \tag{4.25}$$

where I_{cell} is cell current, A_{cell} is cell area, i_0 exchange current density (rate coeffcient), c_{red}, $c_{red,eq}$, c_{ox}, $c_{ox,eq}$ the present and equilibrium concentration of the reduced and oxidized ions, β_{CE} a symmetry parameter and V_{CE} the voltage loss. If redox ion concentrations can be assumed to be the same as their equilibrium values, then this equation is also called the Butler-Volmer equation [25].

A complicating factor with the iodide/tri-iodide redox couple is that electron transfer seems to involve the dissociation of iodine molecules into elemental iodine on the catalyst surface and the subsequent electron transfer to form iodide [44]. This means that, as far as the counter electrode reaction is concerned, the oxidized redox "ion" is actually iodine atom. Assuming that all the other reactions are in equilibrium, one can use the law of mass action to express atomic iodine concentration in terms of iodide and tri-iodide [18].

$$c_I = K_I \cdot \sqrt{\frac{c_{I_3^-}}{c_{I^-}}} \tag{4.26}$$

where K_I is the equilibrium constant.

The resulting current-overpotential relation is

$$\frac{I_{cell}}{A_{cell}} = i_0 \left(\sqrt{\frac{c_{I_3}}{c_{I_{3,eq}}} \cdot \frac{c_{I_{eq}^-}}{c_{I^-}}} e^{\beta_{CE} \frac{qV_{CE}}{k_B T}} - \frac{c_{I^-}}{c_{I_{eq}^-}} e^{-(1-\beta_{CE}) \frac{qV_{CE}}{k_B T}} \right) \tag{4.27}$$

4.2.6 Contact Resistance and Substrate Recombination

Significant recombination occurs at low photovoltages from the fluorine-doped tin oxide (FTO) surface and therefore blocking layers of compact TiO_2 deposited with spray pyrolysis are used to reduce this effect [12]. The blocking layer could also lead to a significant contact resistance as its interface with could function as a Schottky diode. Fortunately in practice the contact resistance appears to be negligible [14, 18, 39]. Therefore this resistance is taken to be zero in this report.

Based on Tafel plots in a report by Cameron et al. [12] substrate recombination is taken to have the same current–voltage behaviour as the counter electrode.

$$\frac{I_{surf}}{A_{cell}} = i_{0,s} \left(\sqrt{\frac{c_{I_3}}{c_{I_{3,eq}}} \cdot \frac{c_{I_{eq}^-}}{c_{I^-}}} e^{\beta_{PE} \frac{qV_{PE}}{k_B T}} - \frac{c_{I^-}}{c_{I_{eq}^-}} e^{-(1-\beta_{PE}) \frac{qV_{PE}}{k_B T}} \right) \tag{4.28}$$

where I_{surf} is the substrate recombination current, $i_{0,s}$ the substrate exchange current and V_{PE} is the photoelectrode voltage.

4.2.7 Electrolyte Capacitance

Electric potential difference between a solid electrode and bulk electrolyte results in ions moving towards or away from the electrode according to their electric charge. The standard Gouy-Chapman-Stern theory [25] divides the electrolyte in two layers: In the compact layer ions are densely packed on the electrode surface and their response to changes in electric field is small. The opposite is true for the diffuse layer as the concentration of ions is so small that they can be thought of as point charges. Although the theory provides only a qualitative description of experimental electrolytes, it is deemed adequate for the purposes of this report as counter electrode capacitance is not particularly important for dye solar cell performance.

The key prediction here is that differential capacitance is not constant but will depend on overpotential. Electrolyte capacitance will also affect the photoelectrode but it is assumed that this has already been taken into account by the phenomenological trap density of states. The author would also argue that due to the relatively large mass and likely nonlinear transport kinetics caused by dense packing of ions the charges cannot be assumed to relax to a steady state infinitely fast resulting in the prediction that electrolyte capacitance will depend on the frequency of an electric perturbation. This is indeed experimentally observed in most solid–electrolyte interfaces although usually it is explained to be caused by the microscopic structure of the interface [45].

For the purposes of the model presented here, electrolyte capacitance is taken to behave as an ideal capacitor.

4.2.8 Substrate Series Resistance

A dye solar cell must be constructed on conductive substrate as the semiconductor has too high a resistivity for efficient lateral current collection. The most common substrate is fluorine doped tin oxide (FTO) glass which is about 80% transparent in the visible with sheet resistance values of ca. 7-15 ohms/square [46].

Voltage loss due to sheet resistance depends mostly on cell configuration with large (dimensions exceeding 1 cm) continuous areas having very high loss [47]. The magnitude of the voltage loss itself is not a significant complicating factor in cell modelling, but the distributed nature of it is. Sheet resistance causes different parts of the cell to experience a different applied voltage which effectively makes the cell nonhomogeneous. However, in practice laboratory scale cells are simply made small enough (<1 cm^2) for a single series resistor approximation to be reasonable. Nevertheless, some measurements can be expected to be somewhat distorted due to the distributed series resistance caused by the geometry of the cell. In this report simulations are made with no substrate series resistance present.

4.2.9 Summary and Normalized Form of the Continuity Equations

Inserting the generation, recombination and trapping terms into the continuity equations yields

$$\left(1+\frac{n_{t,eq}\beta_T}{n_{c,eq}^{\beta_T}}\cdot n_c^{\beta_T-1}\right)\cdot\frac{\partial n_c}{\partial t}=D_c\frac{\partial^2 n_c}{\partial x^2}-k_r\cdot\frac{c_{acc}}{c_{acc,eq}}\cdot(n_c-n_{c,eq})^\gamma$$
$$+\eta_{LH}\eta_{INJ}\phi\cdot\frac{k_{REG}c_{red}}{k_{REG}c_{red}+k_e n_c}\cdot\frac{\alpha_t}{e^{\alpha_t d}-1}e^{\alpha_t x} \tag{4.29}$$

for conduction band electrons. Iodide and tri-iodide equations are

$$\frac{\partial c_{red}}{\partial t}=D_{red}\frac{\partial^2 c_{red}}{\partial x^2}+S_{red}k_r\cdot\frac{c_{acc}}{c_{acc,eq}}\cdot(n_c-n_{c,eq})^\gamma$$
$$-S_{red}\eta_{LH}\eta_{INJ}\phi\cdot\frac{k_{REG}c_{red}}{k_{REG}c_{red}+k_e n_c}\cdot\frac{\alpha_t}{e^{\alpha_t d}-1}e^{\alpha_t x} \tag{4.30}$$

$$\frac{\partial c_{ox}}{\partial t}=D_{ox}\frac{\partial^2 c_{ox}}{\partial x^2}+S_{ox}k_r\cdot\frac{c_{acc}}{c_{acc,eq}}\cdot(n_c-n_{c,eq})^\gamma$$
$$-S_{ox}\eta_{LH}\eta_{INJ}\phi\cdot\frac{k_{REG}c_{red}}{k_{REG}c_{red}+k_e n_c}\cdot\frac{\alpha_t}{e^{\alpha_t d}-1}e^{\alpha_t x} \tag{4.31}$$

in the porous photoelectrode film and

$$\frac{\partial c_{red,F}}{\partial t}=D_{red,F}\frac{\partial^2 c_{red,F}}{\partial x^2} \tag{4.32}$$

$$\frac{\partial c_{ox,F}}{\partial t}=D_{ox,F}\frac{\partial^2 c_{ox,F}}{\partial x^2} \tag{4.33}$$

in the free electrolyte layer. The subsript F indicates this layer.

Expressing all concentrations by the normalized concentration (concentration divided by equlibrium concentration and denoted with the subscript N) and distance by normalized distance y (distance divided by photoelectrode film thickness d) results in

$$T_{c,N}\cdot\frac{\partial n_{c,N}}{\partial t}=\frac{D_c n_{c,eq}}{d}\cdot\frac{\partial^2 n_{c,N}}{\partial y^2}-R_N\cdot(n_{c,N}-1)^\gamma+G_N e^{\alpha_t dy} \tag{4.34}$$

$$T_{red,N}\cdot\frac{\partial c_{red,N}}{\partial t}=\frac{D_{red}c_{red,eq}}{S_{red}d}\cdot\frac{\partial^2 c_{red,N}}{\partial y^2}+R_N\cdot(n_{c,N}-1)^\gamma-G_N\cdot e^{\alpha_t dy} \tag{4.35}$$

$$T_{ox,N}\cdot\frac{\partial c_{ox,N}}{\partial t}=\frac{D_{ox}c_{ox,eq}}{S_{ox}d}\cdot\frac{\partial^2 c_{ox,N}}{\partial y^2}-R_N\cdot(n_{c,N}-1)^\gamma+G_N\cdot e^{\alpha_t dy} \tag{4.36}$$

$$T_{red,N} \cdot \frac{\partial c_{red,F,N}}{\partial t} = \frac{D_{red,F} c_{red,eq}}{S_{red} d} \cdot \frac{\partial^2 c_{red,F,N}}{\partial y^2} \tag{4.37}$$

$$T_{ox,F} \cdot \frac{\partial c_{ox,F,N}}{\partial t} = \frac{D_{ox,F} c_{ox,eq}}{S_{ox} d} \cdot \frac{\partial^2 c_{ox,F,N}}{\partial y^2} \tag{4.38}$$

where

$$T_{c,N} = n_{c,eq} d + n_{t,eq} d \beta_T \cdot n_{c,N}^{\beta_T - 1} \tag{4.39}$$

$$T_{red,N} = \frac{c_{red,eq} d}{S_{red}} \tag{4.40}$$

$$T_{ox,N} = \frac{c_{ox,eq} d}{S_{ox}} \tag{4.41}$$

$$R_N = k_r d n_{c,eq}^{\gamma} \tag{4.42}$$

$$G_N = \eta_{LH} \eta_{INJ} \phi \cdot \left(1 + \frac{k_e n_{c,eq}}{k_{REG} c_{red,eq}} \cdot \frac{n_{c,N}}{c_{red,N}} \right)^{-1} \cdot \frac{\alpha_t d}{e^{\alpha_t d} - 1} \tag{4.43}$$

The advantage of the normalized formalism is that it reduces the number of independent parameters. Note that the redox ion equations have been divided by either S_{ox} or S_{red} in order to group these numbers with the diffusion coefficients.

4.2.10 DC and AC Equations

As the continuity equations are nonlinear and have two independent variables, solving the time-dependent cases are somewhat demanding problems. For sinusoidal small perturbations, however, it is possible to find a solution that simplifies the system to a linear one with one independent variable. This is one of the main reasons why this report focuses on impedance spectroscopy as analysing sinusoidal data is much easier compared to other waveforms or transient measurements.

Deriving the small perturbation equations begins with stating that electron and ion concentrations can be divided into steady-state (DC) and time-dependent (AC) parts. Here, photon flux is considered to remain constant.

$$n_{c,N}(y,t) = n_{DC}(y) + n_{AC}(y,t) \tag{4.44}$$

$$c_{red,N}(y,t) = c_{red,DC}(y) + c_{red,AC}(y,t) \tag{4.45}$$

$$c_{ox,N}(y,t) = c_{ox,DC}(y) + c_{ox,AC}(y,t) \tag{4.46}$$

$$c_{red,F,N}(y,t) = c_{red,F,DC}(y) + c_{red,F,AC}(y,t) \tag{4.47}$$

$$c_{ox,F,N}(y,t) = c_{ox,F,DC}(y) + c_{ox,F,AC}(y,t) \tag{4.48}$$

Linear terms separate easily into DC and AC terms but for nonlinear terms first-order Taylor polynomial approximations are necessary.

$$\begin{aligned}&\frac{c_{acc,DC}+c_{acc,AC}}{c_{acc,eq}}\cdot\left(n_{DC}+n_{AC}-1\right)^{\gamma} \approx \frac{c_{acc,DC}}{c_{acc,eq}}\cdot\left(n_{DC}-1\right)^{\gamma}\\ &+\frac{c_{acc,AC}}{c_{acc,eq}}\cdot\left(n_{DC}-1\right)^{\gamma}+\gamma\cdot\frac{c_{acc,DC}}{c_{acc,eq}}\cdot\left(n_{DC}-1\right)^{\gamma-1}n_{AC}\end{aligned} \tag{4.49}$$

$$\left(n_{DC}+n_{AC}\right)^{\beta_T-1}\cdot\frac{\partial\left(n_{DC}+n_{AC}\right)}{\partial t} \approx n_{DC}^{\beta_T-1}\cdot\frac{\partial n_{AC}}{\partial t} \tag{4.50}$$

$$\begin{aligned}&\left(1+\frac{k_e n_{c,eq}}{k_{REG}c_{red,eq}}\cdot\frac{n_{DC}+n_{AC}}{c_{red,DC}+c_{red,AC}}\right)^{-1} \approx \left(1+\frac{k_e n_{c,eq}}{k_{REG}c_{red,eq}}\cdot\frac{n_{DC}}{c_{red,DC}}\right)^{-1}\\ &-\left(1+\frac{k_e n_{c,eq}}{k_{REG}c_{red,eq}}\cdot\frac{n_{DC}}{c_{red,DC}}\right)^{-2}\cdot\frac{k_e n_{c,eq}}{k_{REG}c_{red,eq}}\cdot\frac{1}{c_{red,DC}}\cdot n_{AC}\\ &+\left(1+\frac{k_e n_{c,eq}}{k_{REG}c_{red,eq}}\cdot\frac{n_{DC}}{c_{red,DC}}\right)^{-2}\cdot\frac{k_e n_{c,eq}}{k_{REG}c_{red,eq}}\cdot\frac{n_{DC}}{c_{red,DC}^2}\cdot c_{red,AC}\end{aligned} \tag{4.51}$$

Inserting these approximations into the continuity equations results in separate DC and AC equations.

DC equations are:

$$\begin{aligned}&\frac{D_c n_{c,eq}}{d}\cdot\frac{\partial^2 n_{DC}}{\partial y^2}-k_r d n_{c,eq}^{\gamma}\cdot\frac{c_{acc,DC}}{c_{acc,eq}}\cdot\left(n_{DC}-1\right)^{\gamma}\\ &+\eta_{LH}\eta_{INJ}\phi\cdot\eta_{REG,DC}\cdot\frac{\alpha_t d}{e^{\alpha_t d}-1}e^{\alpha_t dy}=0\end{aligned} \tag{4.52}$$

$$\begin{aligned}&\frac{D_{red}c_{red,eq}}{S_{red}d}\cdot\frac{\partial^2 c_{red,DC}}{\partial y^2}+k_r d n_{c,eq}^{\gamma}\cdot\frac{c_{acc,DC}}{c_{acc,eq}}\cdot\left(n_{DC}-1\right)^{\gamma}\\ &-\eta_{LH}\eta_{INJ}\phi\cdot\eta_{REG,DC}\cdot\frac{\alpha_t d}{e^{\alpha_t d}-1}e^{\alpha_t dy}=0\end{aligned} \tag{4.53}$$

$$\frac{D_{ox}c_{ox,eq}}{S_{ox}d}\cdot\frac{\partial^2 c_{ox,DC}}{\partial y^2}-k_r d n_{c,eq}^{\gamma}\cdot\frac{c_{acc,DC}}{c_{acc,eq}}\cdot(n_{DC}-1)^{\gamma}$$
$$+\eta_{LH}\eta_{INJ}\phi\cdot\eta_{REG,DC}\cdot\frac{\alpha_t d}{e^{\alpha_t d}-1}e^{\alpha_t dy}=0 \tag{4.54}$$

$$\frac{D_{red,F}c_{red,eq}}{S_{red}d}\cdot\frac{\partial^2 c_{red,F,DC}}{\partial y^2}=0 \tag{4.55}$$

$$\frac{D_{ox,F}c_{ox,eq}}{S_{ox}d}\cdot\frac{\partial^2 c_{ox,F,DC}}{\partial y^2}=0 \tag{4.56}$$

AC equations are:

$$\left(n_{c,eq}d+n_{t,eq}d\beta_T\cdot n_{DC}^{\beta_T-1}\right)\cdot\frac{\partial n_{AC}}{\partial t}=\frac{D_c n_{c,eq}}{d}\cdot\frac{\partial^2 n_{AC}}{\partial y^2}$$
$$-k_r d n_{c,eq}^{\gamma}\cdot\frac{c_{acc,AC}}{c_{acc,eq}}\cdot(n_{DC}-1)^{\gamma}-k_r d n_{c,eq}^{\gamma}\cdot\gamma\cdot\frac{c_{acc,DC}}{c_{acc,eq}}\cdot(n_{DC}-1)^{\gamma-1}n_{AC}$$
$$+\eta_{LH}\eta_{INJ}\phi\cdot(\eta_{REG,AC,n}+\eta_{REG,AC,red})\cdot\frac{\alpha_t d}{e^{\alpha_t d}-1}e^{\alpha_t dy} \tag{4.57}$$

$$\frac{c_{red,eq}d}{S_{red}}\cdot\frac{\partial c_{red,AC}}{\partial t}=\frac{D_{red}c_{red,eq}}{S_{red}d}\cdot\frac{\partial^2 c_{red,AC}}{\partial y^2}+k_r d n_{c,eq}^{\gamma}\cdot\frac{c_{acc,AC}}{c_{acc,eq}}\cdot(n_{DC}-1)^{\gamma}$$
$$+k_r d n_{c,eq}^{\gamma}\cdot\gamma\cdot\frac{c_{acc,DC}}{c_{acc,eq}}\cdot(n_{DC}-1)^{\gamma-1}n_{AC}$$
$$-\eta_{LH}\eta_{INJ}\phi\cdot(\eta_{REG,AC,n}+\eta_{REG,AC,red})\cdot\frac{\alpha_t d}{e^{\alpha_t d}-1}e^{\alpha_t dy} \tag{4.58}$$

$$\frac{c_{ox,eq}d}{S_{ox}}\cdot\frac{\partial c_{ox,AC}}{\partial t}=\frac{D_{ox}c_{red,eq}}{S_{ox}d}\cdot\frac{\partial^2 c_{ox,AC}}{\partial y^2}-k_r d n_{c,eq}^{\gamma}\cdot\frac{c_{acc,AC}}{c_{acc,eq}}\cdot(n_{DC}-1)^{\gamma}$$
$$-k_r d n_{c,eq}^{\gamma}\cdot\gamma\cdot\frac{c_{acc,DC}}{c_{acc,eq}}\cdot(n_{DC}-1)^{\gamma-1}n_{AC}$$
$$+\eta_{LH}\eta_{INJ}\phi\cdot(\eta_{REG,AC,n}+\eta_{REG,AC,red})\cdot\frac{\alpha_t d}{e^{\alpha_t d}-1}e^{\alpha_t dy} \tag{4.59}$$

$$\frac{c_{red,eq}d}{S_{red}}\cdot\frac{\partial c_{red,F,AC}}{\partial t}=\frac{D_{red,F}c_{red,eq}}{S_{red}d}\cdot\frac{\partial^2 c_{red,F,AC}}{\partial y^2} \tag{4.60}$$

$$\frac{c_{ox,eq}d}{S_{ox}}\cdot\frac{\partial c_{ox,F,AC}}{\partial t}=\frac{D_{ox,F}c_{ox,eq}}{S_{ox}d}\cdot\frac{\partial^2 c_{ox,F,AC}}{\partial y^2} \tag{4.61}$$

where

$$\eta_{REG,DC} = \left(1 + \frac{k_e n_{c,eq}}{k_{REG} c_{red,eq}} \cdot \frac{n_{DC}}{c_{red,DC}}\right)^{-1} \tag{4.62}$$

$$\eta_{REG,AC,n} = -\left(1 + \frac{k_e n_{c,eq}}{k_{REG} c_{red,eq}} \cdot \frac{n_{DC}}{c_{red,DC}}\right)^{-2} \cdot \frac{k_e n_{c,eq}}{k_{REG} c_{red,eq}} \cdot \frac{1}{c_{red,DC}} \cdot n_{AC} \tag{4.63}$$

$$\eta_{REG,AC,red} = \left(1 + \frac{k_e n_{c,eq}}{k_{REG} c_{red,eq}} \cdot \frac{n_{DC}}{c_{red,DC}}\right)^{-2} \cdot \frac{k_e n_{c,eq}}{k_{REG} c_{red,eq}} \cdot \frac{n_{DC}}{c_{red,DC}^2} \cdot c_{red,AC}. \tag{4.64}$$

The AC equations are linear which enables solutions of the form

$$f(y,t) = g(y)e^{i\omega t} \Rightarrow \frac{\partial f}{\partial t} = i\omega g(y)e^{i\omega t} \tag{4.65}$$

where f is the concentration of any of the charge carriers, i is the imaginary unit and ω is the angular frequency of the AC signal. Inserting this solution makes it possible to divide the time-dependent exponential part out of the equations leaving position y as the only independent variable.

4.2.11 Boundary Conditions: DC problem

For the substrate–photoelectrode interface two alternative boundary conditions are used: Dirichlet-type condition for known voltage and Neumann-type for known current.

Voltage boundary condition fixes the normalized electron concentration at the interface:

$$n_{DC}(y=0) = e^{\frac{qV_{PE}}{k_B T}} \tag{4.66}$$

where n_{DC} is the normalized electron concentration and V_{PE} is the voltage applied to the photoelectrode (the difference between current electron Fermi level at the FTO contact and electron Fermi level at equilibrium both divided by elementary charge). Note that setting V_{PE} to zero correctly results in the equilibrium electron concentration because the normalized concentration is defined as the actual concentration divided by the equilibrium concentration ($n_{DC} = \frac{n_c}{n_{c,eq}}$). Also note that V_{PE} is not the same as measured cell voltage which includes voltage loss due to series resistance.

Current boundary condition fixes the electron flux:

$$\frac{D_c n_{c,eq}}{d} \cdot \frac{\partial n_{DC}(y=0)}{\partial y} = \frac{I_{cell} + I_{surf}}{qA_{cell}} \tag{4.67}$$

where I_{cell} is the current in the external circuit and I_{surf} is the substrate recombination current. In this report the DC current boundary condition is used only for the analytical approximations in chapter 5, where the sum of cell and substrate recombination currents is specified.

Electrons are not permitted to flow through the back "wall" of the photoelectrode as elec-

trons will transfer into the electrolyte only by recombination or via the counter electrode. Therefore the flux at the right hand side is zero.

$$\frac{D_c n_{c,eq}}{d} \cdot \frac{\partial n_{DC}(y=1)}{\partial y} = 0 \tag{4.68}$$

As for the redox ions in the electrolyte, substrate recombination causes oxidized ions to turn into reduced ions. Thus at the substrate there is a flux boundary condition for both ion types.

$$\frac{D_{red} c_{red,eq}}{S_{red} d} \cdot \frac{\partial c_{red,DC}(y=0)}{\partial y} = -\frac{I_{surf}}{q A_{cell}} \tag{4.69}$$

$$\frac{D_{ox} c_{ox,eq}}{S_{ox} d} \cdot \frac{\partial c_{ox,DC}(y=0)}{\partial y} = \frac{I_{surf}}{q A_{cell}} \tag{4.70}$$

Substrate recombination current I_{surf} is given in equation 4.28.

At the boundary between photoelectrode and free electrolyte layer ion concentrations and their fluxes must be continuous.

$$c_{red,DC}(y=1) = c_{red,F,DC}(y=1) \tag{4.71}$$

$$c_{ox,DC}(y=1) = c_{ox,F,DC}(y=1) \tag{4.72}$$

$$\frac{D_{red} c_{red,eq}}{d} \cdot \frac{\partial c_{red,DC}(y=1)}{\partial y} = \frac{D_{red,F} c_{red,eq}}{d} \cdot \frac{\partial c_{red,F,DC}(y=1)}{\partial y} \tag{4.73}$$

$$\frac{D_{ox} c_{ox,eq}}{d} \cdot \frac{\partial c_{ox,DC}(y=1)}{\partial y} = \frac{D_{ox,F} c_{ox,eq}}{d} \cdot \frac{\partial c_{ox,F,DC}(y=1)}{\partial y} \tag{4.74}$$

The fact that total number of atoms taking part in the redox reactions in the cell must remain unchanged at all times gives the final conditions. Assuming that electron accumulation in the photoelectrode has a negligible effect on overall charge in the electrolyte, atomic conservation leads to the conservation of both reduced and oxidized ions individually. Mathematically this means that the integrals of both redox ion concentrations across the entire cell are always constant,

$$\int_0^1 P c_{red,DC}\, dy + \int_1^{\frac{d_{el}}{d}+1} c_{red,F,DC}\, dy = 1 \tag{4.75}$$

$$\int_0^1 P c_{ox,DC}\, dy + \int_1^{\frac{d_{el}}{d}+1} c_{ox,F,DC}\, dy = 1 \tag{4.76}$$

where d_{el} is the length of the free electrolyte layer. The photoelectrode porosity P is used to take into account the lower volume of electrolyte per unit of total volume in the photoelectrode compared to the free electrolyte layer as some of the space is taken by the solid semiconductor.

The integrals can be converted into differential equation form for the purpose of implement-

ing them in numerical differential equation solvers.

$$\frac{dI_{red}}{dy} = \begin{cases} Pc_{red,DC} & \text{if } 0 \leq y \leq 1 \\ c_{red,F,DC} & \text{if } 1 \leq y \leq 1 + \frac{d_{el}}{d} \end{cases} \tag{4.77}$$

$$\frac{dI_{ox}}{dy} = \begin{cases} Pc_{ox,DC} & \text{if } 0 \leq y \leq 1 \\ c_{ox,F,DC} & \text{if } 1 \leq y \leq 1 + \frac{d_{el}}{d} \end{cases} \tag{4.78}$$

where I_{red} and I_{ox} and the integrated redox ion concentrations.

The boundary conditions are

$$I_{red}(y = 0) = 0 \tag{4.79}$$

$$I_{red}(y = 1 + \frac{d_{el}}{d}) = 1 \tag{4.80}$$

$$I_{ox}(y = 0) = 0 \tag{4.81}$$

$$I_{ox}(y = 1 + \frac{d_{el}}{d}) = 1 \tag{4.82}$$

4.2.12 Boundary Conditions: AC problem

In this report the only alternate current measurement considered is impedance spectroscopy. Most boundary conditions remain the same as in the steady-state case.

Starting with electron boundary conditions, both sides have current boundary conditions.

$$\frac{D_c n_{c,eq}}{d} \cdot \frac{\partial n_{AC}(y = 0)}{\partial y} = \frac{I_{cell,AC} e^{i\omega t} + I_{surf,AC} e^{i\omega t}}{qA_{cell}} \tag{4.83}$$

where $I_{cell,AC}$ and $I_{surf,AC}$ are the amplitudes of the external and substrate recombination currents, respectively.

$$\frac{D_c n_{c,eq}}{d} \cdot \frac{\partial n_{AC}(y = 1)}{\partial y} = 0 \tag{4.84}$$

It was previously assumed in the derivation of the continuity equations that redox ion concentrations are not affected by capacitive effects on the photoelectrode surface. The same simplification is also made for substrate and counter electrode capacitances. Therefore only electron transfer across the interfaces (faradaic current) contributes to redox ion concentration fluxes.

$$\frac{D_{red}c_{red,eq}}{S_{red}d} \cdot \frac{\partial c_{red,AC}(y=0)}{\partial y} = -\frac{I_{surf,AC,R}e^{i\omega t}}{qA_{cell}} \tag{4.85}$$

$$\frac{D_{ox}c_{ox,eq}}{S_{ox}d} \cdot \frac{\partial c_{ox,AC}(y=0)}{\partial y} = \frac{I_{surf,AC,R}e^{i\omega t}}{qA_{cell}} \tag{4.86}$$

where $I_{surf,AC,R}$ is the faradaic part of the substrate recombination current amplitude. In the next section this will be linked to the electron and redox ion concentrations at the substrate.

Continuity of redox ion concentrations and fluxes remain valid for the free electrolyte layer interface.

$$c_{red,AC}(y=1) = c_{red,F,AC}(y=1) \tag{4.87}$$

$$c_{ox,AC}(y=1) = c_{ox,F,AC}(y=1) \tag{4.88}$$

$$\frac{D_{red}c_{red,eq}}{d} \cdot \frac{\partial c_{red,AC}(y=1)}{\partial y} = \frac{D_{red,F}c_{red,eq}}{d} \cdot \frac{\partial c_{red,F,AC}(y=1)}{\partial y} \tag{4.89}$$

$$\frac{D_{ox}c_{ox,eq}}{d} \cdot \frac{\partial c_{ox,AC}(y=1)}{\partial y} = \frac{D_{ox,F}c_{ox,eq}}{d} \cdot \frac{\partial c_{ox,F,AC}(y=1)}{\partial y} \tag{4.90}$$

The same arguments used in redox ion concentration gradients at the substrate are also valid for the counter electrode:

$$\frac{D_{red}c_{red,eq}}{S_{red}d} \cdot \frac{\partial c_{red,AC}(y=\frac{d_{el}}{d})}{\partial y} = \frac{I_{cell,AC,R}e^{i\omega t}}{qA_{cell}} \tag{4.91}$$

$$\frac{D_{ox}c_{ox,eq}}{S_{ox}d} \cdot \frac{\partial c_{ox,AC}(y=\frac{d_{el}}{d})}{\partial y} = -\frac{I_{cell,AC,R}e^{i\omega t}}{qA_{cell}} \tag{4.92}$$

where $I_{cell,AC,R}$ is the faradaic part of the cell external current amplitude.

4.2.13 Substrate Recombination and Counter Electrode Responses for Small Perturbations

Earlier in sections 4.2.5 and 4.2.6 steady-state expressions for counter electrode overpotential and substrate recombination were presented. For a small perturbation these must be linearized in order to obtain the AC response.

In the previous section current was used in the boundary conditions. Therefore it is natural to use current as the perturbing signal here as well.

Differentiating both sides of equation 4.27 by cell current and rearranging leads to

$$\frac{\partial V_{CE}}{\partial I_{cell}} = \frac{k_B T}{q i_0 A_{cell}} \left(\beta_{CE} \sqrt{\frac{c_{ox,N}}{c_{red,N}}} e^{\beta_{CE} \frac{qV_{CE}}{k_B T}} + (1-\beta_{CE}) \cdot c_{red,N} e^{-(1-\beta_{CE}) \frac{qV_{CE}}{k_B T}} \right)^{-1}$$
$$\cdot \left(1 + \left(\frac{i_0 A_{cell}}{2} \sqrt{\frac{c_{ox,N}}{c_{red,N}^3}} e^{\beta_{CE} \frac{qV_{CE}}{k_B T}} + i_0 A_{cell} e^{-(1-\beta_{CE}) \frac{qV_{CE}}{k_B T}} \right) \cdot \frac{\partial c_{red,N}}{\partial I_{cell}} \right.$$
$$\left. - \frac{i_0 A_{cell}}{2} \sqrt{\frac{1}{c_{ox,N} c_{red,N}}} e^{\beta_{CE} \frac{qV_{CE}}{k_B T}} \cdot \frac{\partial c_{ox,N}}{\partial I_{cell}} \right) \tag{4.93}$$

AC voltage loss can be approximated by

$$V_{AC} = \frac{\partial V}{\partial I}(V_{DC}) \cdot I_{AC} = R(V_{DC}) \cdot I_{AC} \tag{4.94}$$

where $R(V_{DC})$ is the differential resistance of the system at voltage V_{DC}. Therefore counter electrode AC voltage loss is

$$V_{CE,AC} = \frac{k_B T}{q i_0 A_{cell}}$$
$$\cdot \left(\beta_{CE} \sqrt{\frac{c_{ox,DC}}{c_{red,DC}}} e^{\beta_{CE} \frac{qV_{CE,DC}}{k_B T}} + (1-\beta_{CE}) \cdot c_{red,DC} e^{(\beta_{CE}-1) \frac{qV_{CE,DC}}{k_B T}} \right)^{-1}$$
$$\cdot \left(I_{cell,AC,R} + \left(\frac{i_0 A_{cell}}{2} \sqrt{\frac{c_{ox,DC}}{c_{red,DC}^3}} e^{\beta_{CE} \frac{qV_{CE,DC}}{k_B T}} + i_0 A_{cell} e^{(\beta_{CE}-1) \frac{qV_{CE,DC}}{k_B T}} \right) \cdot c_{red,AC} \right.$$
$$\left. - \frac{i_0 A_{cell}}{2} \sqrt{\frac{1}{c_{ox,DC} c_{red,DC}}} e^{\beta_{CE} \frac{qV_{CE,DC}}{k_B T}} \cdot c_{ox,AC} \right) \tag{4.95}$$

where the simplification

$$\frac{\partial (c_{red/ox,DC} + c_{red/ox,AC})}{\partial I_{cell,AC,R}} \cdot I_{cell,AC,R} = \frac{c_{red/ox,AC}}{I_{cell,AC,R}} \cdot I_{cell,AC,R} = c_{red/ox,AC} \tag{4.96}$$

is used. This is valid because the AC continuity equations are linear so redox ion concentrations are proportional to the perturbing currents.

Substrate recombination is governed by the same mathematics so

$$V_{PE,AC} = \frac{k_B T}{q i_{0,s} A_{cell}}$$
$$\cdot \left(\beta_{PE} \sqrt{\frac{c_{ox,DC}}{c_{red,DC}}} e^{\beta_{PE} \frac{qV_{PE,DC}}{k_B T}} + (1-\beta_{PE}) \cdot c_{red,DC} e^{-(1-\beta_{PE}) \frac{qV_{PE,DC}}{k_B T}} \right)^{-1}$$
$$\cdot \left(I_{surf,AC,R} + \left(\frac{i_{0,s} A_{cell}}{2} \sqrt{\frac{c_{ox,DC}}{c_{red,DC}^3}} e^{\beta_{PE} \frac{qV_{PE,DC}}{k_B T}} + i_{0,s} A_{cell} e^{-(1-\beta_{PE}) \frac{qV_{PE,DC}}{k_B T}} \right) \cdot c_{red,AC} \right.$$
$$\left. - \frac{i_{0,s} A_{cell}}{2} \sqrt{\frac{1}{c_{ox,DC} c_{red,DC}}} e^{\beta_{PE} \frac{qV_{PE,DC}}{k_B T}} \cdot c_{ox,AC} \right) \tag{4.97}$$

The previous section required linking the faradaic parts of the substrate and external currents to the electron and redox ion concentrations. In the simulations presented in this report, it is noted that the substrate and counter electrode capacitances are sufficiently small that for low frequencies capacitive currents are actually insignificant compared to the faradaic currents. At high frequencies redox ion concentration changes are negligible meaning that the relative magnitudes of faradaic and capacitive currents are irrelevant. Therefore

$$I_{cell,AC,R} \approx I_{cell,AC} \tag{4.98}$$

$$I_{surf,AC,R} \approx I_{surf,AC} \tag{4.99}$$

Substrate recombination current $I_{surf,AC}$ is not known before the model is solved. However, knowledge of its value is unnecessary as it simply links redox ion gradients (equations 4.89 and 4.90) to photoelectrode voltage (equation 4.97).

4.2.14 Electron Concentration and Photoelectrode Voltage

Solid state physics states (see equation 2.19) that the normalized electron concentration at the photoelectrode–substrate interface has the form

$$n_{c,N}(y=0) = e^{\frac{qV_{PE}}{k_B T}} \tag{4.100}$$

where $n_{c,N}$ is the normalized electron concentration (absolute electron concentration divided by equilibrium concentration) and V_{PE} is the photoelectrode voltage (difference between current and equilibrium electron quasi-Fermi levels divided by elementary charge). The measured cell voltage is given in the next section.

Rearranging for voltage results in

$$V_{PE} = \frac{k_B T}{q} \cdot \ln(n_{c,N}(y=0)) \tag{4.101}$$

Dividing both voltage and electron concentration into DC and AC terms gives

$$V_{PE,DC} + V_{PE,AC} = \frac{k_B T}{q} \cdot \ln\left(n_{DC}(y=0) + n_{AC}(y=0)\right)$$
$$\approx \frac{k_B T}{q} \cdot \left(\ln\left(n_{DC}(y=0)\right) + \frac{n_{AC}(y=0)}{n_{DC}(y=0)}\right) \tag{4.102}$$

Thus AC voltage is

$$V_{PE,AC} = \frac{k_B T}{q} \cdot \frac{n_{AC}(y=0)}{n_{DC}(y=0)} \tag{4.103}$$

4.2.15 Reference Electrode Potential

As stated before, differences in electrochemical potential of electrons between two points can be measured as voltage. In the previous section photoelectrode voltage was expressed as a function of electron concentration. The reference level against which photoelectrode electrochemical potential is compared in this picture is the equilibrium level at zero bias in the dark as determined by the electrolyte electrochemical potential. However, during cell operation redox ion concentrations differ from their equilibrium values and subsequently the electrolyte electrochemical potential becomes position-dependent.

For a two electrode measurement this has already been taken into account in the counter electrode overpotential as equation 4.27 actually gives the potential difference between the counter electrode and the equilibrium level. Thus in the cell voltage equation the photoelectrode and counter electrode reference potentials cancel out.

$$\begin{aligned} V_{cell} &= \frac{1}{q} \cdot (E_{F,PE} - E_{F,eq} - E_{F,CE} + E_{F,eq}) - V_S \\ &= \frac{1}{q} \cdot (E_{F,PE} - E_{F,CE}) - V_S \\ &= V_{PE} - V_{CE} - V_S \end{aligned} \tag{4.104}$$

where V_{PE} is the photoelectrode voltage, V_{CE} counter electrode voltage and V_S voltage loss due to series resistance.

Three electrode measurements enable the measurement of photoelectrode and counter electrode voltages separately by adding a new electrode that is assumed to be in equilibrium with the electrolyte (no current is allowed to flow through it) and measuring its potential with respect to either the photoelectrode or the counter electrode (or both if the series resistance between the two is negligible). The potential difference between this reference electrode and equilibrium potential is given by the Nernst equation

$$V_{REF} = \frac{k_B T}{zq} \ln\left(\left(\frac{c_{ox,eq}}{c_{ox}}\right)^{v_{ox}} \cdot \left(\frac{c_{red}}{c_{red,eq}}\right)^{v_{red}}\right) \tag{4.105}$$

where z is the number electrons transferred in the reaction from reduced ion to oxidized ion or vice versa, v_{ox} the number of oxidized ions involved in the reaction and v_{red} the number of

reduced ions involved. Note that, as stated before, in the case of the tri-iodide/iodide redox couple, the counter electrode reaction involves iodine atoms and iodide. Therefore one can use $z = 1$ and the oxidized ion concentration can be calculated using the law of mass action (equation 4.26). The result is the same if one considers only the iodide/tri-iodide equilibrium reaction.

$$V_{REF,DC} = \frac{k_B T}{zq} \ln \left(\sqrt{\frac{c_{I_{3,eq}^-}}{c_{I_{3,DC}^-}} \cdot \frac{c_{I_{DC}^-}}{c_{I_{eq}^-}}} \cdot \frac{c_{I_{DC}^-}}{c_{I_{eq}^-}} \right) \tag{4.106}$$

For the AC case the reference voltage should be linearized in the same way as photoelectrode voltage, giving

$$V_{REF,AC} = \frac{k_B T}{q} \cdot \left(-\frac{1}{2} \cdot \frac{c_{I_3^-,AC}}{c_{I_3^-,DC}} + \frac{3}{2} \cdot \frac{c_{I^-,AC}}{c_{I^-,DC}} \right) \tag{4.107}$$

where the law of mass action has been used to obtain the redox ion concentrations. This equation can also be obtained from the counter electrode overpotential equation by taking the limit of infinite exchange current density.

In this report the reference electrode is assumed to be located at the counter electrode. Measurable voltages are therefore

$$V_{PE/REF} = V_{PE} - V_{REF} \tag{4.108}$$

and

$$V_{CE/REF} = V_{CE} - V_{REF} \tag{4.109}$$

Redox ion concentrations are naturally evaluated at the counter electrode ($y = 1 + \frac{d_{el}}{d}$).

4.2.16 Impedance

Impedance is defined as the ratio of AC voltage and current. Overall cell impedance Z_{TOT} is the external AC voltage divided by the external AC current.

$$Z_{TOT} = -\frac{V_{cell,AC}}{I_{cell,AC}} \tag{4.110}$$

where the minus sign is due to the signs chosen for voltage and current in this report.

Cell voltage comprises of photoelectrode voltage and counter electrode voltage resulting in two impedance elements (three if series resistance is also included). In the photoelectrode model only faradaic substrate and counter electrode currents were taken into account. Therefore the impedances are corrected for the presence capacitance via parallel connections.

$$Z_{TOT} = Z_{PE+SU} + Z_{CE} = \left(-\frac{I_{cell,AC}}{V_{PE,AC} - V_{REF,AC}} + i\omega C_{SU} \right)^{-1} + \left(\frac{I_{cell,AC}}{V_{CE,AC} - V_{REF,AC}} + i\omega C_{CE} \right)^{-1} \quad (4.111)$$

4.3 Results

4.3.1 Parameter Values

Parameter values for the model were chosen so that simulated experiments would give roughly the same results as reported in most of the references as well as the experimental results in the next chapter. Basic parameters are given in table 4.1 and the derived normalized ones in table 4.2. Most of the normalized parameters can be, at least in principle, measured using purely electrical measurements, whereas measuring any of the basic values will require other methods as well.

Recombination rate coefficient k_r was set to produce a reasonable open circuit voltage (about 0.8 V at a light intensity roughly comparable to one sun). Electron equilibrium and trapped electron equilibrium concentrations were set so that transport resistance and photoelectrode capacitance values derived from simulated impedance spectra were reasonably close to the ones measured from the experimental cell (see next chapter for details). Trap distribution parameter was also based on the same measurements. Light absorption coefficient was set to correspond to moderate absorption corresponding to the fact the typical N719 dye absorbs only weakly at high wavelengths [32]. Regeneration coefficients were set to give similar dye regeneration efficiencies as given by Anderson et al. [43]. Redox ion diffusion coefficients in the film were based on free electrolyte layer values for acetonitrile solvent [48] reduced by a factor of three due to the porosity, tortuosity and constrictivity of the film. Equilibrium concentrations corresponded to the electrolyte recipe used in the experimental work reported in the next chapter (30 mM I_2 and 0.6 M I^- with all iodine forming tri-iodide). Counter electrode exchange current density was set to produce a very low counter electrode differential resistance of about 1 Ωcm^2 [18] at zero bias current. Substrate exchange current density was simply set to a value where it was a significant but not dominant recombination source. Symmetry factors were set to 0.5 as this is the simplest case.

Parameter description	Symbol	Unit	Value	Reference
Photoelectrode parameters				
Electron diffusion coefficient	D_c	m^2/s	$2.0 \cdot 10^{-9}$	[49]
Recombination rate coefficient	k_r	$m^{3\gamma-2}/s$	$5.0 \cdot 10^{7}$	assumption
Recombination order	γ	–	0.7	[18]
Electron equilibrium concentration	$n_{c,eq}$	$1/m^3$	$3.0 \cdot 10^{9}$	assumption
Trapped electrons at equilibrium	$n_{t,eq}$	$1/m^3$	$5.0 \cdot 10^{20}$	assumption
Trap distribution parameter	β_T	–	0.3	assumption
Film thickness	d	m	$10 \cdot 10^{-6}$	[34]
Film porosity	P	–	0.5	[50]
Optical parameters				
Total light absorption coefficient	α_t	1/m	$1.0 \cdot 10^{5}$	assumption
Light harvesting efficiency	η_{LH}	–	0.7	assumption
Injection efficiency	η_{INJ}	–	1.0	assumption
Regeneration rate coefficient	k_{REG}	$1/(m^2s)$	$7.28 \cdot 10^{-13}$	assumption
Dye recombination rate coefficient	k_e	$1/(m^2s)$	$1.0 \cdot 10^{-12}$	assumption
Electrolyte parameters				
Iodide diffusion coefficient in photoelectrode	D_{red}	m^2/s	$3.0 \cdot 10^{-10}$	assumption
Tri-iodide diffusion coefficient in photoelectrode	D_{ox}	m^2/s	$3.0 \cdot 10^{-10}$	assumption
Iodide diffusion coefficient in free electrolyte	$D_{red,F}$	m^2/s	$9.0 \cdot 10^{-10}$	[48]
Tri-iodide diffusion coefficient in free electrolyte	$D_{ox,F}$	m^2/s	$9.0 \cdot 10^{-10}$	[48]
Iodide equilibrium concentration	$c_{red,eq}$	$1/m^3$	$3.43 \cdot 10^{26}$	assumption
Tri-iodide equilibrium concentration	$c_{ox,eq}$	$1/m^3$	$1.81 \cdot 10^{25}$	assumption
Iodide reaction coefficient	S_{red}	–	1.5	
Tri-iodide reaction coefficient	S_{ox}	–	0.5	
Free electrolyte layer thickness	d_{el}	m	$30 \cdot 10^{-6}$	assumption
Counter electrode parameters				
Exchange current density	i_0	A/m^2	$2.0 \cdot 10^{-2}$	assumption
Symmetry factor	β_{CE}	–	0.5	assumption
Capacitance	C_{CE}	F	$1.5 \cdot 10^{-4}$	assumption
Substrate parameters				
Exchange current density	$i_{0,s}$	A/m^2	$3.0 \cdot 10^{-6}$	assumption
Symmetry factor	β_{PE}	–	0.5	assumption
Capacitance	C_{PE}	F	$5.0 \cdot 10^{-5}$	assumption
Cell and external parameters				
Cell area	A_{cell}	m^2	$1 \cdot 10^{-4}$	assumption
Cell temperature	T	K	298	assumption
Incident photon flux	φ	$1/(m^2s)$	$2.0 \cdot 10^{21}$	

Table 4.1: Base parameter values used in dye solar cell modelling.

Parameter description	Symbol	Unit	Value
Photoelectrode parameters			
Normalized electron diffusion coefficient	$D_c n_{c,eq}/d$	$1/(\mathrm{m}^2\mathrm{s})$	$1.8 \cdot 10^8$
Normalized recombination rate coefficient	$k_r n_{c,eq}^{\gamma} d$	$1/(\mathrm{m}^2\mathrm{s})$	$1.29 \cdot 10^{11}$
Recombination order	γ	–	0.7
Normalized electron equilibrium concentration	$n_{c,eq} d$	$1/\mathrm{m}^2$	$3.0 \cdot 10^4$
Normalized trapped electrons at equilibrium	$n_{t,eq} d$	$1/\mathrm{m}^2$	$1.5 \cdot 10^{15}$
Trap distribution parameter	β_T	–	0.3
Film porosity	P	–	0.5
Optical parameters			
Normalized total light absorption coefficient	$\alpha_t d$	–	$1.0 \cdot 10^5$
Light harvesting efficiency	η_{LH}	–	0.7
Injection efficiency	η_{INJ}	–	1.0
Normalized dye recombination rate coefficient	$k_e n_{c,eq}/(k_{REG} c_{red,eq})$		$4.0 \cdot 10^{-15}$
Electrolyte parameters			
Normalized iodide diffusion coefficient	D_{red}/d^2	1/s	3.0
Normalized tri-iodide diffusion coefficient	D_{ox}/d^2	1/s	3.0
Iodide diffusion coefficient ratio	$D_{red}/D_{red,F}$	–	0.333
Tri-iodide diffusion coefficient ratio	$D_{ox}/D_{ox,F}$	–	0.333
Normalized iodide equilibrium concentration	$c_{red,eq} d/S_{red}$	$1/\mathrm{m}^2$	$2.29 \cdot 10^{21}$
Normalized tri-iodide equilibrium concentration	$c_{ox,eq} d/S_{ox}$	$1/\mathrm{m}^2$	$3.61 \cdot 10^{20}$
Normalized free electrolyte layer thickness	$\frac{d_{el}}{d}$		3.00
Counter electrode parameters			
Exchange current density	i_0	$\mathrm{A/m}^2$	$3.0 \cdot 10^{-6}$
Symmetry factor	β_{CE}	–	0.5
Capacitance	C_{CE}	F	$5.0 \cdot 10^{-6}$
Substrate parameters			
Exchange current density	$i_{0,s}$	$\mathrm{A/m}^2$	$3.0 \cdot 10^{-6}$
Symmetry factor	β_{PE}	–	0.5
Capacitance	C_{PE}	F	$5.0 \cdot 10^{-6}$
Cell and external parameters			
Cell area	A_{cell}	m^2	$1 \cdot 10^{-4}$
Cell temperature	T	K	298
Incident photon flux	φ	$1/(\mathrm{m}^2\mathrm{s})$	$2.0 \cdot 10^{21}$

Table 4.2: Base case normalized parameter values used in dye solar cell modelling.

4.3.2 Charge Carrier Concentrations

Figures 4-3, 4-4 and 4-5 show simulated (see appendix C for a brief description of the model solver) electron, iodide and tri-iodide concentrations in the cell at short circuit, maximum power point and at open circuit. A key finding from the calculations is that beyond maximum power point electron and iodide concentrations remain fairly flat whereas tri-iodide concentration is approximately constant only near open circuit. These results are consistent with earlier work by various authors [9, 13, 19, 37, 50].

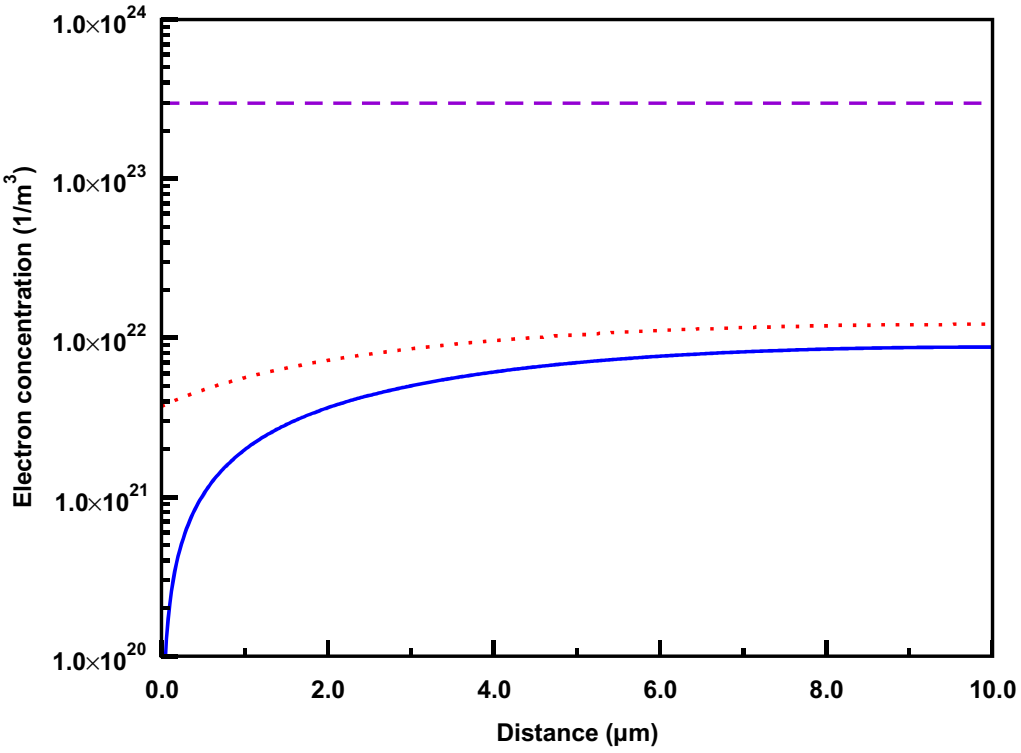

Figure 4-3: Simulated photoelectrode conduction band electron concentrations at short circuit (solid line), maximum power point (dotted line) and open circuit (dashed line).

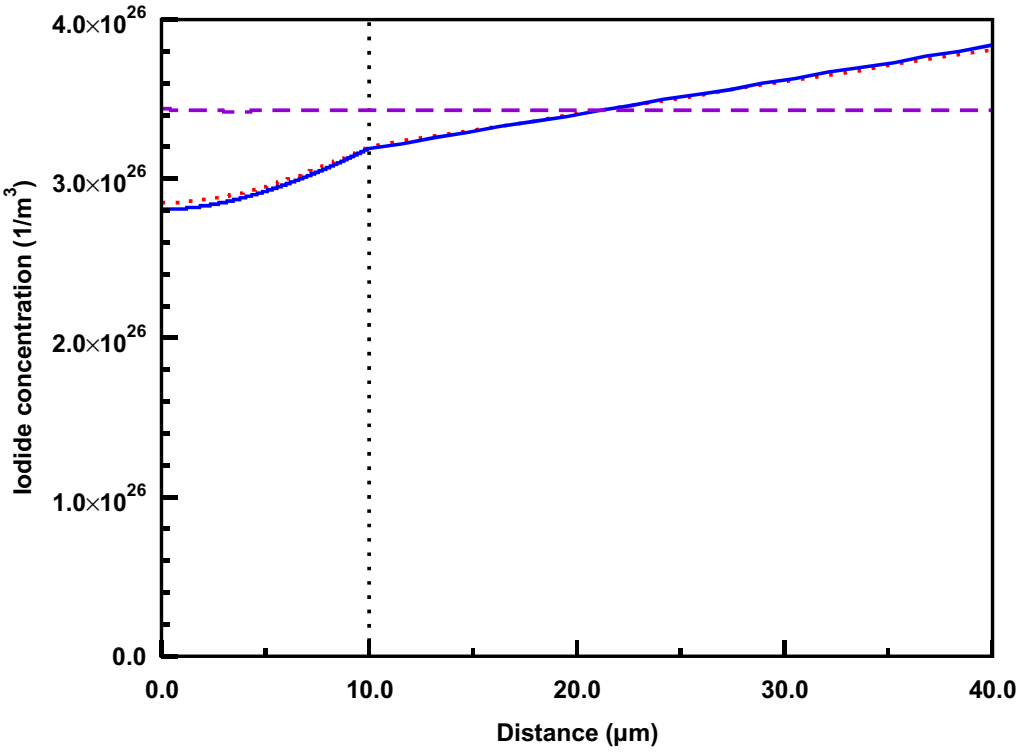

Figure 4-4: Simulated iodide concentrations at short circuit (solid line), maximum power point (dotted line) and open circuit (dashed line). $3.0 \cdot 10^{26}$ ions per cubic metre is approximately 0.5 M (moles per litre).

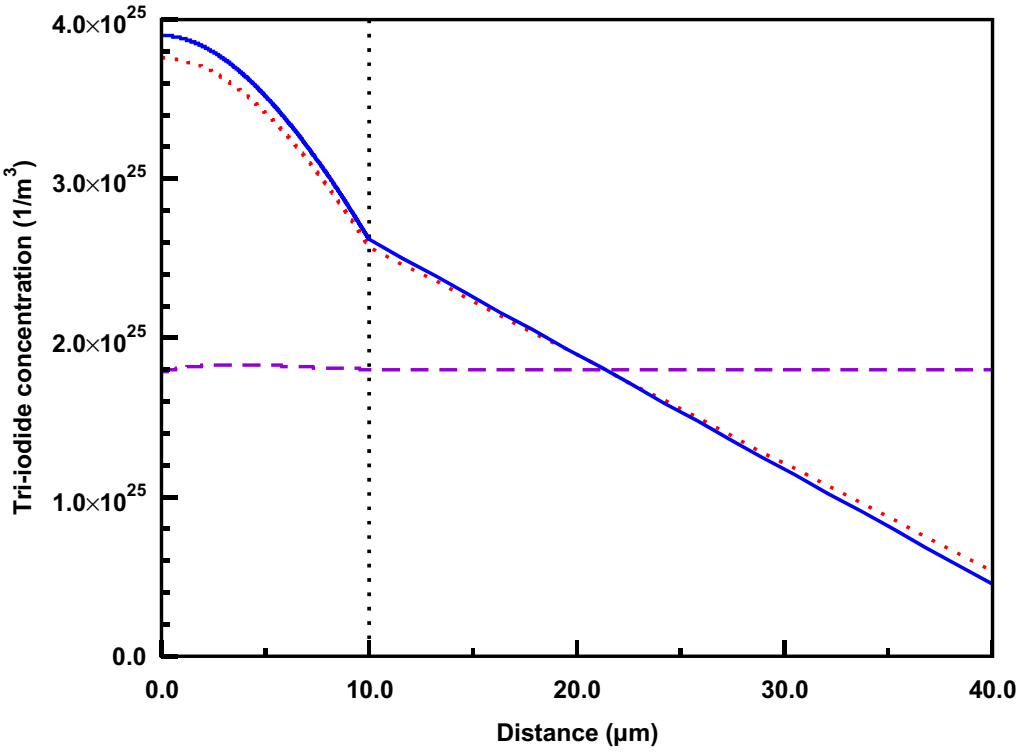

Figure 4-5: Simulated tri-iodide concentrations at short circuit (solid line), maximum power point (dotted line) and open circuit (dashed line). $3.0 \cdot 10^{25}$ ions per cubic metre is approximately 50 mM (millimoles per litre).

4.3.3 Light Intensity Dependence of Short Circuit Current and Open Circuit Voltage

The light intensity dependence of short circuit current and open circuit voltage were simulated for four different cell variations: in the base case all parameter values were as they are given in table 4.2, in the perfect regeneration case normalized dye recombination rate coefficient was set to zero, in the no substrate recombination case subtrate exchange current was additionally set to zero, and in the last case the the entire electrolyte model was omitted in addition to the previous changes.

Figure 4-6 shows the simulated incident photon to collected electron (IPCE) values for the model variations. Substrate recombination was calculated to be insignificant and therefore the results from the model variant with no substrate recombination are not plotted in the figure. In this case short circuit refers to the voltage applied to the photoelectrode meaning that cell voltage is slightly negative due to series resistance at the counter electrode. At low light intensities all models result in effectively the same IPCE values. At high light intensities tri-iodide concentration increases at the photoelectrode (see figure 4-5) leading to increased recombination. In the base case model variant IPCE is lowered even further by the decrease of regeneration efficiency due to both higher electron and lower iodide concentrations at the photoelectrode (see equation 4.24).

The most important finding is that IPCE increases with light intensity as long as electrolyte mass transport and dye recombination effects are small enough to be negligible. The reason is that current density is proportional to the gradient of electron concentration whereas photoelectrode recombination is sublinear with respect to electron concentration. However, if electron collection is already 100% effective at low light intensities, then IPCE will remain constant. These results indicate that plotting IPCE as a function of light intensity is a simple and useful way of obtaining qualitative information about electron collection and mass transport in the electrolyte.

Calculated open circuit voltages are plotted in figure 4-7. Diffusion of redox ions in the electrolyte had a negligible effect on simulated open circuit voltages so the no electrolyte model variant has been omitted from the figure. Consistent with results at short circuit, regeneration efficiency was effectively perfect below 0.75 V. Substrate recombination, on the other hand, lowers open circuit voltages the most at low light intensities. All models result in voltages that are well-described by linear fits to the logarithm of light intensity indicating that plotting open circuit voltage as a function of light intensity cannot be used to differentiate between different recombination mechanisms.

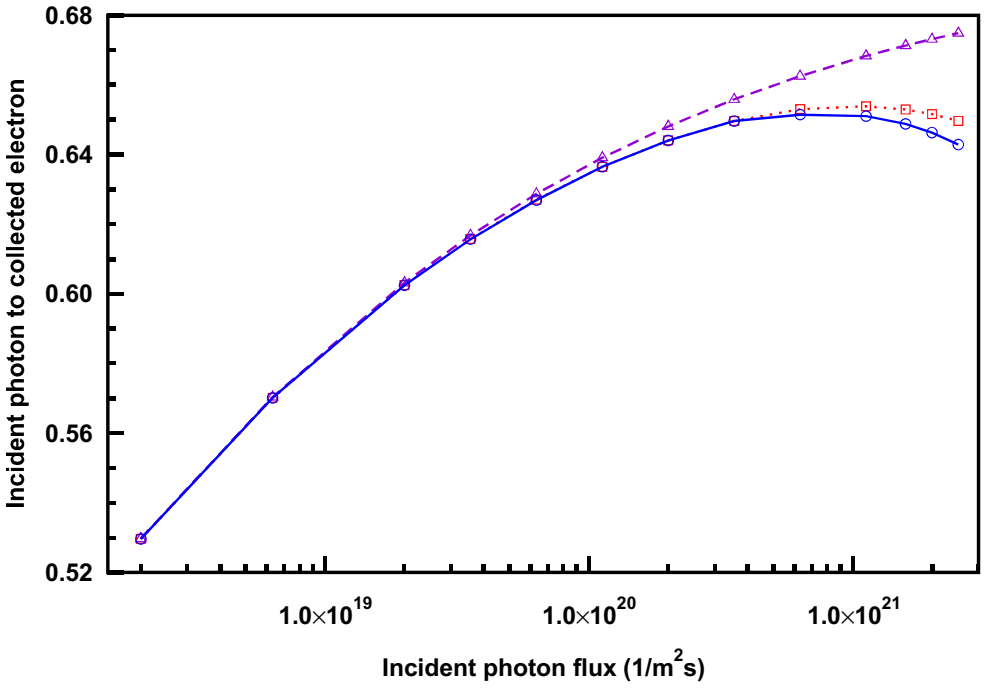

Figure 4-6: Simulated IPCE values for base case (circles and solid line), perfect regeneration (squared and dotted line) and no electrolyte mass transport (triangles and dashed line) model variations. Removing substrate recombination had an insignificant effect on short circuit currents compared to the perfect regeneration case and is therefore not shown.

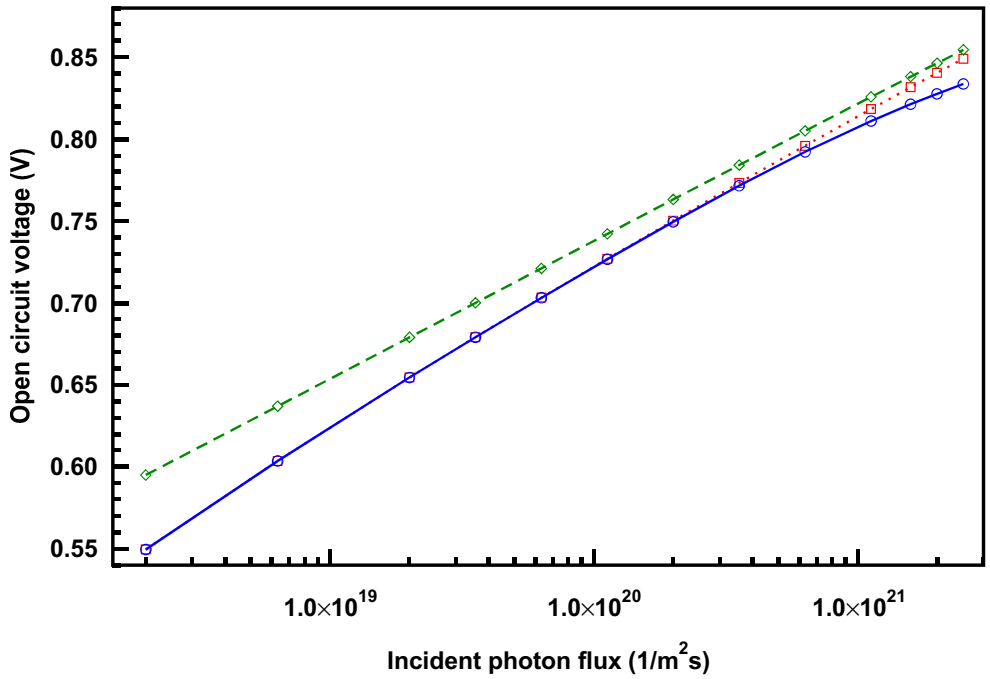

Figure 4-7: Simulated open circuit voltages for the base (circles and solid line), perfect regeneration (squares and dotted line) and no substrate recombination (diamonds and dashed line) model variations. Electrolyte concentrations at open circuit were essentially the same as equilibrium concentrations meaning that the no electrolyte mass transport model (not shown in figure) resulted in the same values as the no substrate recombination variation. A straight line fit gives an ideality factor of 1.54 for the base case model, 1.61 for the perfect recombination case and 1.42 for the no substrate recombination case.

Chapter 5

Solving the Dye-Sensitized Solar Cell Device Model Inverse Problem at Low Light Intensities

In this chapter a scheme utilizing steady-state and impedance spectroscopy measurements is developed in order solve the inverse problem set up by the device model of the previous chapter. As the model is quite complicated, the scheme assumes that diffusion of ions in the electrolyte can be neglected which greatly simplifies the problem. The downside of the assumption is that the scheme is valid only at low current densities limiting it to low light intensities.

In principle one could use a brute force approach in solving the inverse problem by setting up an optimization routine that varies the parameter values, numerically calculates the DC and AC solutions for all the measurements and then compares the difference between the calculated and measured data before starting a new iteration. However, in practice one finds that the numerical solutions are quite expensive in terms of computing power compared to what is available on a single desktop. Additionally the optimization methods required in both the numerical solutions and the parameter value search are not necessarily robust enough to be left running for long periods of time without human intervention. While these problems could be overcome with enough effort, in this report is has been deemed better to use approximations that enable dividing the problem into several smaller ones. These smaller problems are then simplified until a combination of analytical solutions and numerical optimization using spreadsheet programs can be used to solve them.

First the model is simplified until it can be solved analytically. Then analytical solutions describing the I-V curve (DC solution) and electrical impedance (AC solution) measurements are found. The time-dependent solution is formulated using just a few electric circuit element values. Finally the circuit element values are related to the model parameter values. In addition to the photoelectrode described by the continuity equation, substrate recombination and series resistance are also taken into account.

In section 5.2 the method is applied to simulated data in order to show that the inverse problem can be solved before analysing experimental data in section 5.3.

5.1 Theory

5.1.1 The Simplified Model at Low Current Densities

As shown in figures 4-4 and 4-5, ion concentrations in the electrolyte at open circuit are effectively the same as equilibrium concentrations. Therefore at low current densities it can be assumed that redox ion concentrations do not change from their equilibrium values at all, reducing the number of continuity equations to be solved from five to just the one describing electrons.

Using the division into DC and AC equations from the previous chapter, the electron equations simplify to

$$\begin{aligned}&\frac{D_c n_{c,eq}}{d}\cdot\frac{\partial^2 n_{DC}}{\partial y^2}-k_r d n_{c,eq}^{\gamma}\cdot\left(n_{DC}-1\right)^{\gamma}\\&+\eta_{LH}\eta_{INJ}\phi\cdot\left(1+\frac{k_e n_{c,eq}}{k_{REG}c_{red,eq}}\cdot n_{DC}\right)^{-1}\cdot\frac{\alpha_t d}{e^{\alpha_t d}-1}e^{\alpha_t d y}=0\end{aligned}\tag{5.1}$$

$$\begin{aligned}&\left(n_{c,eq}d+n_{t,eq}d\beta_T\cdot n_{DC}^{\beta_T-1}\right)\frac{\partial n_{AC}}{\partial t}=\frac{D_c n_{c,eq}}{d}\cdot\frac{\partial^2 n_{AC}}{\partial y^2}\\&-k_r d n_{c,eq}^{\gamma}\cdot\gamma\cdot\left(n_{DC}-1\right)^{\gamma-1}n_{AC}\\&+\eta_{LH}\eta_{INJ}\phi\cdot\left(1+\frac{k_e n_{c,eq}}{k_{REG}c_{red,eq}}\cdot n_{DC}\right)^{-2}\cdot\frac{k_e n_{c,eq}n_{AC}}{k_{REG}c_{red,eq}}\cdot\frac{\alpha_t d}{e^{\alpha_t d}-1}e^{\alpha_t d y}\end{aligned}\tag{5.2}$$

The recombination and regeneration terms are nonlinear with respect to normalized electron concentration n_{DC} meaning that analytical solutions are not possible. However, as shown in figure 4-3, beyond maximum power point electron concentration is almost constant. Hence replacing the nonlinear terms with first-order Taylor approximations appears to be a viable strategy in finding an analytical solution.

A first guess for the steady-state equation is calculated by assuming constant electron concentration.

$$n_{DC}(y)\approx n_{fg}\tag{5.3}$$

where n_{fg} is the constant first guess for electron concentration.

Regeneration term is simplified with the following approximation

$$\eta_{REG} = \left(1 + \frac{k_e n_{c,eq}}{k_{REG} c_{red,eq}} n_{fg}\right)^{-1} \approx \left(1 + \frac{k_e n_{c,eq}}{k_{REG} c_{red,eq}} n_{reg,0}\right)^{-1}$$
$$- \left(1 + \frac{k_e n_{c,eq}}{k_{REG} c_{red,eq}} n_{reg,0}\right)^{-2} \cdot \frac{k_e n_{c,eq}}{k_{REG} c_{red,eq}} \cdot \frac{n_{reg,0}^{1-\gamma}}{\gamma} \cdot (n_{fg}^{\gamma} - n_{reg,0}^{\gamma})$$

$$= \eta_{REG,0} \left(1 + \gamma - \gamma \eta_{REG,0}\right)$$
$$- \eta_{REG,0}^2 \cdot \left(\frac{1}{\eta_{REG,0}} - 1\right)^{1-\gamma} \cdot \left(\frac{k_e n_{c,eq}}{k_{REG} c_{red,eq}}\right)^{\gamma} \cdot \frac{n_{fg}^{\gamma}}{\gamma} \tag{5.4}$$

where $\eta_{REG,0}$ is the regeneration efficiency value around which the Taylor approximation is made and $n_{reg,0}$ is the corresponding electron concentration.

Integrating recombination and generation terms across the photoelectrode film thickness gives the current that is extracted at the contact (the sum of cell current and surface recombination current)

$$\int_0^1 \Bigg\{ - k_r d n_{eq}^{\gamma} n_{fg}^{\gamma} + \eta_{REG,0} \left(1 + \gamma - \gamma \eta_{REG,0}\right) \cdot \frac{\phi \eta_{LH} \eta_{INJ} \alpha_t d}{e^{\alpha_t d} - 1} e^{\alpha_t y}$$
$$- \eta_{REG,0}^2 \cdot \left(\frac{1}{\eta_{REG,0}} - 1\right)^{1-\gamma} \cdot \left(\frac{k_e n_{c,eq}}{k_{REG} c_{red,eq}}\right)^{\gamma} \cdot \frac{n_{fg}^{\gamma}}{\gamma} \cdot \frac{\phi \eta_{LH} \eta_{INJ} \alpha_t d}{e^{\alpha_t d} - 1} e^{\alpha_t y} \Bigg\} dy$$
$$= \frac{I_{cell} + I_{surf}}{q A_{cell}}$$
$$\Rightarrow n_{fg} = \left(\frac{\phi \eta_{LH} \eta_{INJ} \cdot (1 + \gamma - \gamma \eta_{REG,0}) - \frac{I_{cell} + I_{surf}}{q A_{cell}}}{k_r d n_{c,eq}^{\gamma} + \eta_{REG,0}^2 \cdot \left(\frac{1}{\eta_{REG,0} - 1}\right)^{1-\gamma} \cdot \left(\frac{k_e n_{c,eq}}{k_{REG} c_{red,eq}}\right)^{\gamma} \cdot \frac{\phi \eta_{LH} \eta_{INJ}}{\gamma}} \right)^{\frac{1}{\gamma}} \tag{5.5}$$

This expression is very important as it relates the (weighted) average electron concentration in the photoelectrode to light intensity, cell current and model parameters.

Now recombination and generation terms can be simplified using Taylor approximations around the first guess n_{fg}. The additional -1 in the recombination term is also removed as electron concentration under illumination or when current is flowing is always so high that it makes no difference (i.e. $n_{DC} \approx n_{fg} \gg 1$) .

For the DC equation the approximations are

$$k_r d n_{c,eq}^{\gamma} \left(n_{DC} - 1\right)^{\gamma} \approx k_r d n_{c,eq}^{\gamma} \left(n_{fg} - 1\right)^{\gamma} + k_r d n_{c,eq}^{\gamma} \gamma \cdot \left(n_{fg} - 1\right)^{\gamma - 1} \cdot \left(n_{DC} - n_{fg}\right)$$
$$\approx k_r d n_{c,eq}^{\gamma} n_{fg}^{\gamma} + k_r d n_{c,eq}^{\gamma} \gamma n_{fg}^{\gamma - 1} \cdot \left(n_{DC} - n_{fg}\right) \tag{5.6}$$

$$\begin{aligned}
&\eta_{LH}\eta_{INJ}\phi \cdot \left(1 + \frac{k_e n_{c,eq}}{k_{REG} c_{red,eq}} \cdot n_{DC}\right)^{-1} \cdot \frac{\alpha_t d}{e^{\alpha_t d} - 1} e^{\alpha_t dy} \\
&\approx \eta_{LH}\eta_{INJ}\phi \cdot \left(1 + \frac{k_e n_{c,eq}}{k_{REG} c_{red,eq}} \cdot n_{fg}\right)^{-1} \cdot \frac{\alpha_t d}{e^{\alpha_t d} - 1} e^{\alpha_t dy} \\
&- \eta_{LH}\eta_{INJ}\phi \cdot \left(1 + \frac{k_e n_{c,eq}}{k_{REG} c_{red,eq}} \cdot n_{fg}\right)^{-2} \cdot \frac{k_e n_{c,eq}}{k_{REG} c_{red,eq}} \cdot (n_{DC} - n_{fg})
\end{aligned} \tag{5.7}$$

and for the AC equation

$$k_r d n_{c,eq}^{\gamma} \gamma \left(n_{DC} - 1\right)^{\gamma} \approx k_r d n_{c,eq}^{\gamma} \gamma n_{fg}^{\gamma} \tag{5.8}$$

$$\begin{aligned}
&\eta_{LH}\eta_{INJ}\phi \cdot \left(1 + \frac{k_e n_{c,eq}}{k_{REG} c_{red,eq}} \cdot n_{DC}\right)^{-2} \cdot \frac{k_e n_{c,eq} n_{AC}}{k_{REG} c_{red,eq}} \cdot \frac{\alpha_t d}{e^{\alpha_t d} - 1} e^{\alpha_t dy} \\
&\approx \eta_{LH}\eta_{INJ}\phi \cdot \left(1 + \frac{k_e n_{c,eq}}{k_{REG} c_{red,eq}} \cdot n_{fg}\right)^{-2} \cdot \frac{k_e n_{c,eq} n_{AC}}{k_{REG} c_{red,eq}}
\end{aligned} \tag{5.9}$$

$$n_{DC}^{\beta_T - 1} \approx n_{fg}^{\beta_T - 1} \tag{5.10}$$

Note that the decay of light intensity in the film is no longer modeled in the generation terms describing recombination to the excited dye (last terms in equations 5.7 and 5.9). Therefore this approximation is accurate only when recombination to the excited state of the dye is negligible or when light is only weakly absorbed in the cell.

The final simplified equations are

$$\begin{aligned}
&\frac{D_c n_{c,eq}}{d} \cdot \frac{\partial^2 n_{DC}}{\partial y^2} - k_r d n_{c,eq}^{\gamma} \cdot \gamma n_{fg}^{\gamma} \cdot (n_{DC} - n_{fg}) - k_r d n_{c,eq}^{\gamma} \cdot n_{fg}^{\gamma} \\
&+ \eta_{LH}\eta_{INJ}\phi \cdot \left(1 + \frac{k_e n_{c,eq}}{k_{REG} c_{red,eq}} \cdot n_{fg}\right)^{-1} \cdot \frac{\alpha_t d}{e^{\alpha_t d} - 1} e^{\alpha_t dy} \\
&- \eta_{LH}\eta_{INJ}\phi \cdot \left(1 + \frac{k_e n_{c,eq}}{k_{REG} c_{red,eq}} \cdot n_{fg}\right)^{-2} \cdot \frac{k_e n_{c,eq}}{k_{REG} c_{red,eq}} \cdot (n_{DC} - n_{fg}) = 0
\end{aligned} \tag{5.11}$$

and

$$\begin{aligned}
&\left(n_{c,eq} d + n_{t,eq} d \beta_T \cdot n_{fg}^{\beta_T - 1}\right) \cdot \frac{\partial n_{AC}}{\partial t} = \frac{D_c n_{c,eq}}{d} \cdot \frac{\partial^2 n_{AC}}{\partial y^2} \\
&- k_r d n_{c,eq}^{\gamma} \cdot \gamma \cdot n_{fg}^{\gamma - 1} n_{AC} \\
&+ \eta_{LH}\eta_{INJ}\phi \cdot \left(1 + \frac{k_e n_{c,eq}}{k_{REG} c_{red,eq}} \cdot n_{fg}\right)^{-2} \cdot \frac{k_e n_{c,eq} n_{AC}}{k_{REG} c_{red,eq}}
\end{aligned} \tag{5.12}$$

The simplified photoelectrode model is expected to be a good approximation when both electron and redox ion concentrations are nearly constant. These conditions occur at low current densities and high voltages. However, at very high voltages redox ion diffusion will affect the gradient of the I-V curve limiting this simplification to low light intensities.

5.1.2 DC Solution for I-V Curves

The simplified DC equation is linear with respect to normalized electron concentration meaning that an analytical solution can be found.

The boundary conditions are the same as in section 4.2.11 of the previous chapter. The analytical solution uses the current boundary condition at the photoelectrode contact.

The solution is

$$\begin{aligned} n_{DC}(y) = & \frac{\lambda}{d} \cdot \frac{d}{D_c n_{c,eq}} \cdot \frac{I_{cell} + I_{surf}}{qA_{cell}} \cdot \left(\sinh(\frac{d}{\lambda}y) - \frac{\cosh(\frac{d}{\lambda}y)}{\tanh(\frac{d}{\lambda})} \right) \\ & + \frac{d}{D_c n_{c,eq}} \cdot \frac{\eta_{LH}\eta_{INJ}\phi}{e^{\alpha_t d} - 1} \cdot \frac{\alpha_t d}{(\alpha_t d)^2 - (\frac{d}{\lambda})^2} \cdot \left(\frac{\alpha_t d e^{\alpha_t d}}{\sinh(\frac{d}{\lambda})} \cdot \frac{\lambda}{d} \cdot \cosh(\frac{d}{\lambda}y) \right. \\ & \left. - e^{\alpha_t dy} + \alpha_t d \sinh(\frac{d}{\lambda}y) - \alpha_t d \cdot \frac{\cosh(\frac{d}{\lambda}y)}{\tanh(\frac{d}{\lambda})} \right) \\ & + n_{fg} - k_r d n_{eq}^{\gamma} \cdot \left(\frac{\lambda}{d} \right)^2 \cdot \frac{d}{D_c n_{c,eq}} \cdot n_{fg}^{\gamma} \end{aligned} \tag{5.13}$$

where

$$\frac{\lambda}{d} = \sqrt{\frac{D_c n_{c,eq}}{d} \cdot \left(k_r d n_{c,eq}^{\gamma} \gamma n_{fg}^{\gamma-1} + \eta_{LH}\eta_{INJ}\phi \cdot \left(1 + \frac{k_e n_{c,eq} \cdot n_{fg}}{k_{REG} c_{red,eq}} \right)^{-2} \cdot \frac{k_e n_{c,eq}}{k_{REG} c_{red,eq}} \right)^{-1}} \tag{5.14}$$

is the differential diffusion length λ [17] divided by film thickness d. The first guess electron concentration n_{fg} is given in equation 5.5.

The significance of this solution is that one only needs to guess the correct regeneration efficiency $n_{REG,0}$ and specify the sum of cell and substrate currents in order to obtain an explicit expression for photoelectrode voltage. Surface recombination and series resistance can be added as correction terms to obtain cell current and voltage.

5.1.3 AC Solution for Impedance Spectroscopy

The boundary conditions for the simplified model are the same as the ones for the full model (see section 4.2.12).

The solution is

$$n_{AC}(y) = \frac{I_{cell,AC} + I_{surf,AC}}{qA_{cell}} \cdot a \cdot \frac{d}{D_c n_{c,eq}} \cdot \left(\sinh(ay) - \frac{\cosh(ay)}{\tanh(a)} \right) \tag{5.15}$$

where

$$a = \sqrt{\left(\frac{d}{\lambda}\right)^2 + i\omega \cdot (n_{c,eq} d + n_{t,eq} d \beta_T n_{fg}^{\beta_T - 1}) \cdot \frac{d}{D_c n_{c,eq}}} \tag{5.16}$$

Impedance of the photoelectrode is defined as

$$\begin{aligned} Z_{PE} &= -\frac{\partial V_{PE,AC}}{\partial (I_{cell,AC} + I_{surf,AC})} \approx -\frac{V_{PE,AC}}{I_{cell,AC} + I_{surf,AC}} \\ &= -\frac{k_B T}{q} \cdot \frac{n_{AC}(y=0)}{n_{DC}(y=0)} \cdot \frac{1}{I_{cell,AC} + I_{surf,AC}} \end{aligned} \tag{5.17}$$

Photoelectrode impedance can be expressed using resistances and capacitances by defining

$$R_T = \frac{k_B T}{q^2 A_{cell}} \cdot \frac{d}{D_c n_{c,eq}} \cdot \frac{1}{n_{DC}(y=0)} \tag{5.18}$$

$$R_{REC,E} = \frac{k_B T}{q^2 A_{cell}} \cdot \frac{n_{fg}^{1-\gamma}}{k_r d n_{c,eq}^{\gamma}} \cdot \frac{1}{\gamma n_{DC}(y=0)} \tag{5.19}$$

$$R_{REC,D} = \frac{k_B T}{q^2 A_{cell}} \cdot \frac{1}{\eta_{LH} \eta_{INJ} \phi} \cdot \left(1 + \frac{k_e n_{c,eq} \cdot n_{fg}}{k_{REG} c_{red,eq}}\right)^2 \cdot \left(\frac{k_e n_{c,eq}}{k_{REG} c_{red,eq}}\right)^{-1} \cdot \frac{1}{n_{DC}(y=0)} \tag{5.20}$$

$$C_T = \frac{q^2 A_{cell}}{k_B T} \cdot (n_{c,eq} d + n_{t,eq} d \beta_T n_{fg}^{\beta_T - 1}) \cdot n_{DC}(y=0) \tag{5.21}$$

where R_T is transport resistance, $R_{REC,E}$ and $R_{REC,D}$ electrolyte and dye recombination resistances, and C_T photoelectrode capacitance.

The resulting impedance is

$$Z_{PE} = \frac{R_T}{\sqrt{\frac{R_T}{R_{REC,E}} + \frac{R_T}{R_{REC,D}} + i\omega C_T} \cdot \tanh \sqrt{\frac{R_T}{R_{REC,E}} + \frac{R_T}{R_{REC,D}} + i\omega C_T}} \tag{5.22}$$

The simplified AC model gives mathematically the same result as the transmission line model [45]. The only difference is that in this model dye recombination is also present although the model has been simplified to the point where it is indistinguishable from recombination to the electrolyte.

The model is not yet complete as the effect of the substrate must also be taken into account. Although substrate recombination is small, that does not mean it or substrate capacitance are negligible. Therefore the photoelectrode impedance element must be placed in parallel with the substrate impedance element Z_{SU}.

$$Z_{PE+SU} = \left(\frac{1}{Z_{PE}} + \frac{1}{Z_{SU}} \right)^{-1} \tag{5.23}$$

$$Z_{SU} = \left(\frac{1}{R_{SU}} + i\omega C_{SU} \right)^{-1} \tag{5.24}$$

where R_{SU} is the substrate differential resistance and C_{SU} is the substrate capacitance.

Substrate differential resistance is derived by differentiating equation 4.28 with photoelectrode voltage V_{PE}

$$R_{SU} = \frac{\partial V_{PE}}{\partial I_{surf}} = \frac{k_B T}{q} \cdot \frac{1}{i_{0,s} A_{cell}} \cdot \left(\beta_{PE} e^{\beta_P E \frac{qV_{PE,DC}}{k_B T}} + (1 - \beta_{PE}) e^{(1-\beta_P E)\frac{qV_{PE,DC}}{k_B T}} \right)^{-1} \tag{5.25}$$

The solution to the simplified model enables fitting impedance spectra individually with each spectrum producing a set of resistances and capacitances that can be used for further analysis.

5.1.4 Model Parameter Values and Circuit Element Values

In the previous section the photoelectrode response to impedance spectroscopy measurement was expressed in terms of one capacitance and three resistance values. In this section these values are related to the model parameters and obsevables such as incident photon flux as well as cell current and voltage.

Remembering the relationship between normalized steady-state electron concentration and voltage applied to the photoelectrode

$$n_{DC}(y = 0) = e^{\frac{qV_{PE}}{k_B T}} \tag{5.26}$$

one can insert this into equations 5.18, 5.19, 5.20 and 5.21 to obtain

$$R_T = \frac{k_B T}{q^2 A_{cell}} \cdot \frac{d}{D_c n_{c,eq}} \cdot e^{-\frac{qV_{PE}}{k_B T}} \tag{5.27}$$

$$R_{REC,E} = \frac{k_B T}{q^2 A_{cell}} \cdot \frac{n_{fg}^{1-\gamma}}{k_r d n_{c,eq}^{\gamma}} \cdot \frac{e^{\frac{-qV_{PE}}{k_B T}}}{\gamma} \tag{5.28}$$

$$R_{REC,D} = \frac{k_B T}{q^2 A_{cell}} \cdot \frac{1}{\eta_{LH} \eta_{INJ} \phi} \cdot \left(1 + \frac{k_e n_{c,eq} \cdot n_{fg}}{k_{REG} c_{red,eq}} \right)^2 \cdot \left(\frac{k_e n_{c,eq}}{k_{REG} c_{red,eq}} \right)^{-1} \cdot e^{-\frac{qV_{PE}}{k_B T}} \tag{5.29}$$

$$C_T = \frac{q^2 A_{cell}}{k_B T} \cdot (n_{c,eq} d + n_{t,eq} d \beta_T n_{fg}^{\beta_T - 1}) \cdot e^{\frac{qV_{PE}}{k_B T}} \tag{5.30}$$

At open circuit photoelectrode voltage equals cell voltage ($V_{PE} = V_{cell}$) meaning that

impedance measurements at open circuit can be fitted to the model parameters. For impedance spectra where DC current is not zero a correction for series resistance must be made.

Note that fitting a single impedance spectrum does not distinguish between recombination to the electrolyte ($R_{REC,E}$) and recombination to the excited dye ($R_{REC,D}$). Only their combination can be measured. In this report this is called photoelectrode recombination resistance R_{REC}.

$$R_{REC} = \left(\frac{1}{R_{REC,E}} + \frac{1}{R_{REC,D}} \right)^{-1} \tag{5.31}$$

5.1.5 Correcting For Substrate Recombination

In the previous sections substrate recombination current was assumed to be known for the methods to work. Here a method to evaluate substrate recombination is presented.

At low cell voltages recombination throughout the photoelectrode film is either negligible or effectively constant. Therefore the curvature of the I-V curve at low voltages is due to substrate recombination as long as current densities are low enough for redox ion concentrations to remain approximately constant.

The result is that in the dark at low voltages the I-V curve can be approximated using a simple diode equation.

$$\begin{aligned} I_{cell} = -I_{surf} &= -A_{cell} \cdot i_{0,s} e^{\beta_{PE} \frac{q(V_{cell}+V_s)}{k_B T}} \\ \Rightarrow \ln(-I_{cell}) &= \ln(A_{cell} \cdot i_{0,s}) + \beta_{PE} \cdot \frac{q(V_{cell}+V_s)}{k_B T} \end{aligned} \tag{5.32}$$

where V_s is the voltage loss due to series resistance.

The importance of this equation is that it enables fitting the symmetry factor β_{PE} and exchange current $i_{0,s}$ if the effect of series resistance can be quantified. Impedance spectroscopy can be used to do this.

An estimate for the differential substrate resistance used in impedance spectroscopy can be calculated by differentiating equation 5.32

$$R_{SU} = \left(\frac{\partial I_{surf}}{\partial (V_{cell}+V_s)} \right)^{-1} = \frac{1}{A_{cell} \cdot i_{0,s} \beta_{PE}} \cdot \frac{k_B T}{q} \cdot e^{-\beta_{PE} \frac{q(V_{cell}+V_s)}{k_B T}} \tag{5.33}$$

5.2 Results From Simulated Data

Before the theory was applied to experimental results, it was validated on simulated data. I-V curves and impedance spectra were simulated using the full numerical model described in the previous chapter. Both photoelectrode and counter electrode impedance values were given separately as this corresponds to a measurement with a reference electrode. Simulated frequencies were approximately from 0.05 Hz to 1000 Hz.

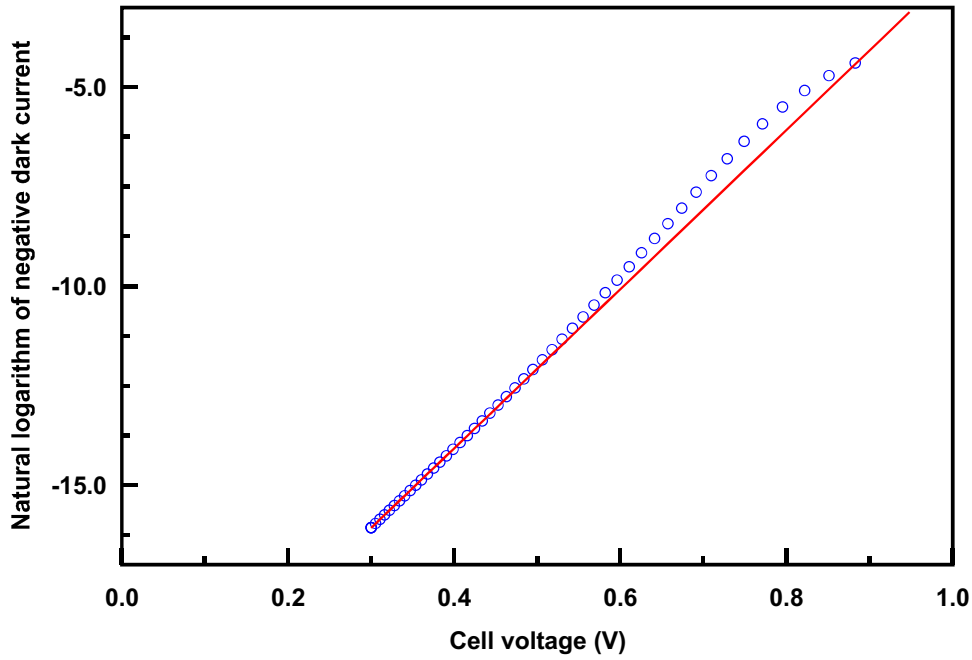

Figure 5-1: Simulated (circles) dark current and a fit to equation 5.32 (solid line). At high cell voltages photoelectrode recombination and electrolyte diffusion start to dominate dark current and equation 5.32 is no longer valid.

5.2.1 Substrate Recombination

Figure 5-1 shows the natural logarithm of simulated dark current as a function of series resistance corrected cell voltage. Fitting a straight line to the low voltage data points yielded reasonable estimates for both the symmetry factor β_{PE} and the exchange current $i_{0,s}$. The substrate resistance values calculated from the fit using equation 5.33 were low enough to make a significant impact to the fitting of simulated impedance spectra.

5.2.2 Impedance Spectra

Photoelectrode impedance data was fitted to equation 5.23 using Microsoft Excel. Counter electrode resistance was assumed to have a constant value based on low frequency counter electrode impedance values calculated from simulated potential differences between counter and reference electrodes.

At low cell voltages the substrate capacitance visibly distorts the high frequency part of the impedance spectrum (figure 5-2). This highlights the importance of including substrate capacitance in the impedance model. The impedance spectra could be fitted to several combi-

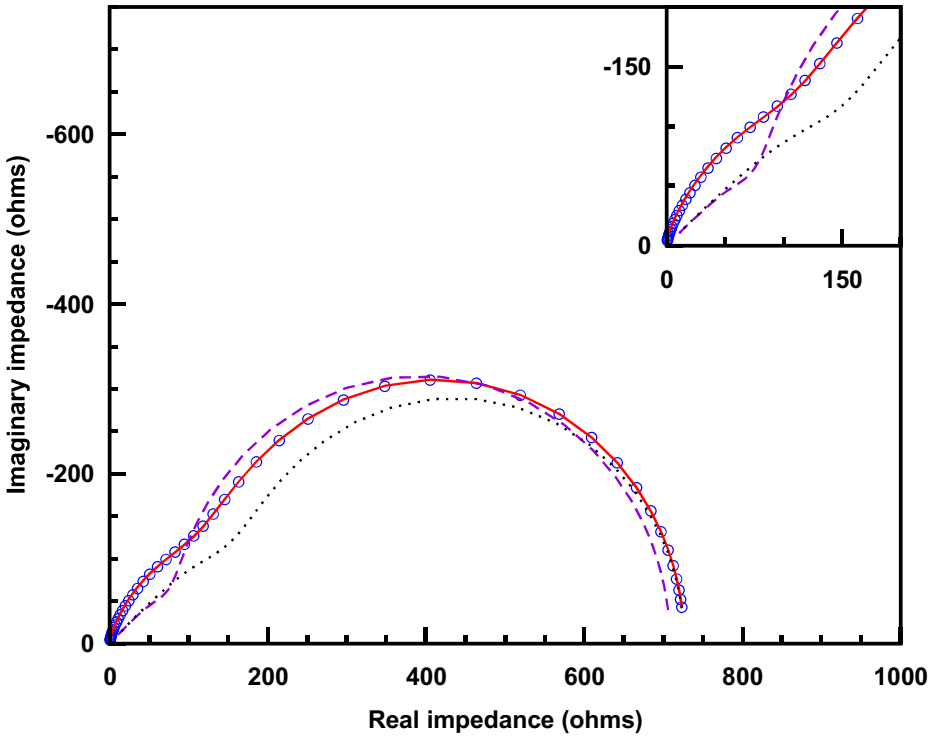

Figure 5-2: Simulated (circles with substrate capacitance, dotted line without substrate capacitance) photoelectrode impedance values at 603 mV bias voltage. At high frequencies (lower left corner in the main figure; also shown in the inset) substrate capacitance causes distortion of the photoelectrode response. Fitting the analytical model without substrate capacitance (dashed line) results in a bad fit with incorrect photoelectrode transport resistance value whereas including substrate capacitance (solid line) gives a good fit and a correct value for transport resistance.

nations of recombination and substrate resistances indicating that the measurement does not adequately distinguish between the two. The solution was that substrate resistance values were taken from the dark current estimate and kept constant throughout the fitting process. Unfortunately this correction did not yield reliable photoelectrode resistance values as the substrate resistances could not be determined to a sufficiently high degree of accuracy.

At high cell voltages tri-iodide diffusion starts to affect the low frequency part of the spectrum which makes fits over the entire frequency range progressively worse. This problem can be alleviated by dropping some of the low frequency data points from the fit entirely as the analytical model does not take into account any redox ion diffusion. Figure 5-3 shows results from the numerical both with and without ion diffusion as well as the obtained fit using the analytical model.

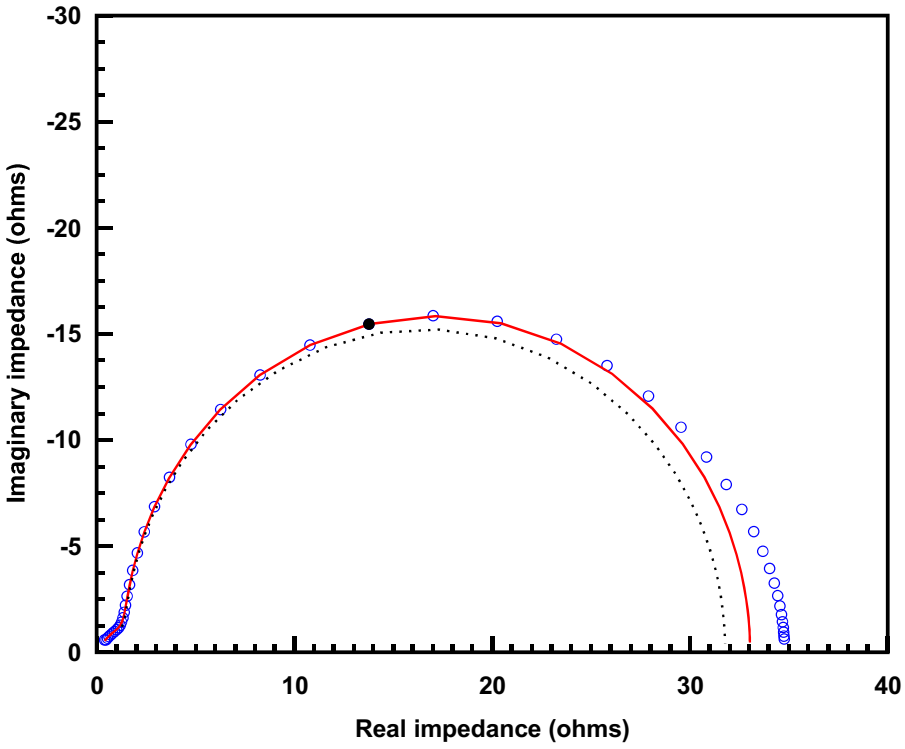

Figure 5-3: Simulated (circles with tri-iodide diffusion, dotted line without) and fitted (solid line) photoelectrode impedance values at 728 mV bias voltage. Dropping low frequency data points (lower right corner) from the fitting partially compensates for the missing ion diffusion in the analytical model resulting in a better fit to the underlying physics. The last data point included in the fitting is shown as a filled circle.

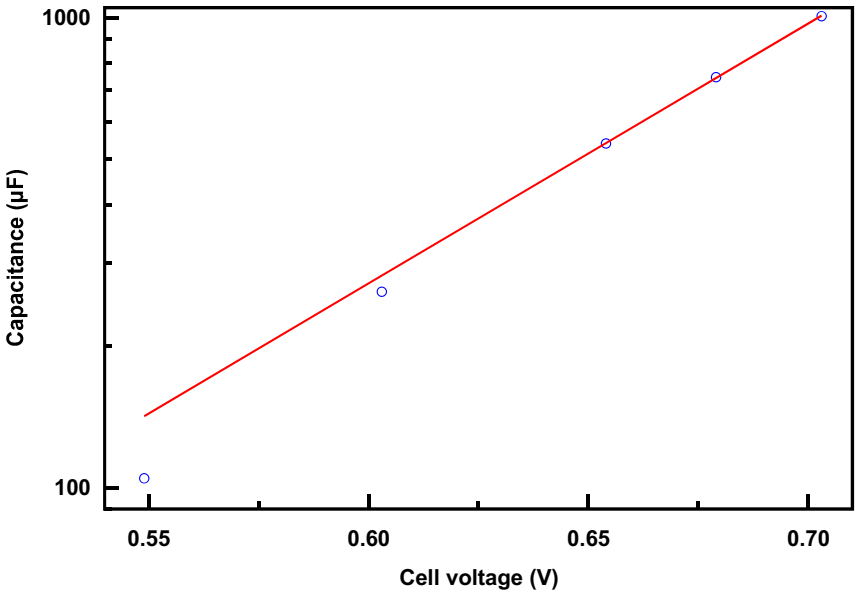

Figure 5-4: Photoelectrode capacitance values derived from simulated impedance measurements (circles) and fit to equation 5.30 (solid line). At low voltages electron concentration is not uniform in the photoelectrode leading to position-dependent capacitance (capacitance is dominated by the nonlinear trapping term defined in equation 4.17) and unreliable fits. Therefore two lowest capacitance values were excluded from fitting.

5.2.3 Circuit Element Fits

Circuit element values were obtained from fitting open circuit impedance spectra to equations 5.27 and 5.30. As it was not possible to get reliable fits for photoelectrode recombination resistances, photoelectrode resistance was combined with the substrate resistance to fit the resulting resistance element by combining equations 5.28, 5.29, 5.31, 5.33 and 5.34.

$$R_{REC+SU} = \left(\frac{\sqrt{\frac{R_T}{R_{REC}}} \cdot \tanh\left(\sqrt{\frac{R_T}{R_{REC}}}\right)}{R_T} + \frac{1}{R_{SU}} \right)^{-1} \tag{5.34}$$

The model parameters were also fit to open circuit voltages using equation 5.13. All fits were performed simultaneously by minimizing the sum of squared relative error. Fits are shown in figures 5-4, 5-5, 5-6 and 5-7.

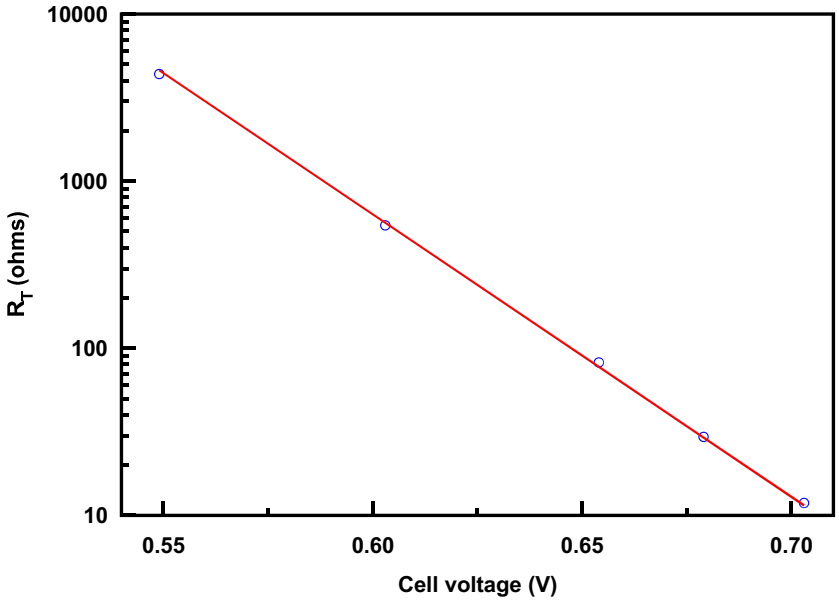

Figure 5-5: Photoelectrode transport resistance values derived from simulated impedance measurements (circles) and fit to equation 5.27 (solid line).

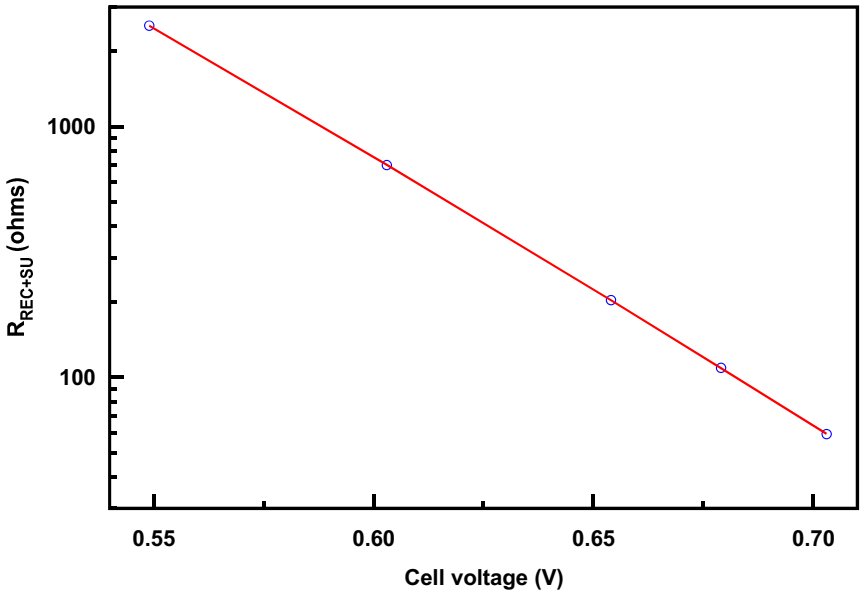

Figure 5-6: Combined photoelectrode and substrate resistance values derived from simulated impedance measurements (circles) and fit to equation 5.34 (solid line).

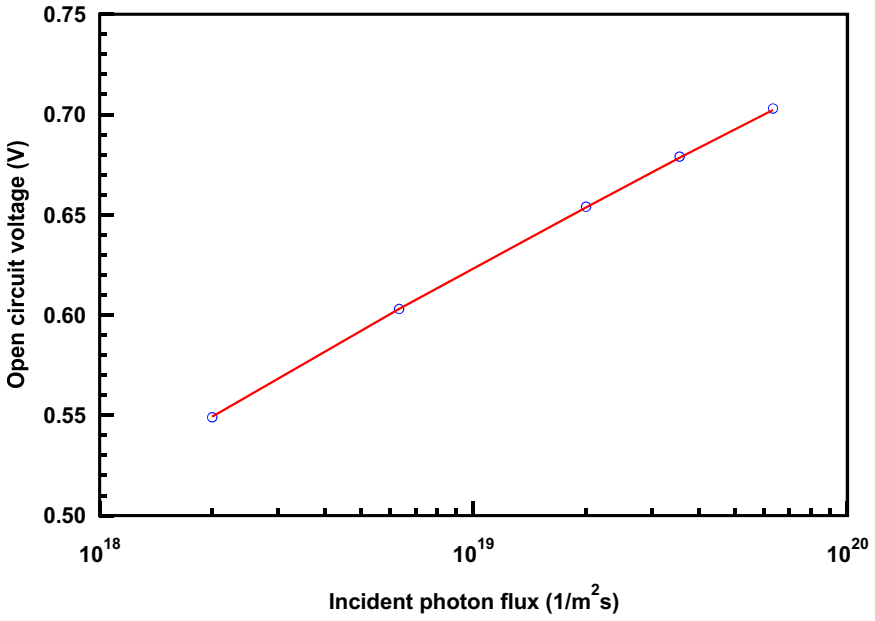

Figure 5-7: Open circuit voltages from numerical simulations (circles) and model fit (solid line, equation 5.13).

5.2.4 Parameter Values and Recreated J-V Curves

Comparison of actual and fitted model parameters is shown in table 5.1. The fitting procedure reproduces the original parameter values with very high accuracy indicating that it is a viable way to solve the inverse problem. Electron equilibrium concentration ($n_{c,eq}$) and dye recombination coefficients ($k_e n_{c,eq}/(k_{REG} c_{red,eq})$) could not be fitted as they have negligible effect on cell operation at the studied voltages. Additionally the model is not sensitive enough to the light absorption coefficient ($\alpha_t d$) to allow it be fitted. Therefore its value was chosen to be the same as in the numerical simulations.

Figure 5-8 compares the I-V curves resulting from the fitted parameters values calculated using the analytical approximation to the original numerical ones. The curves match almost exactly indicating that at low light intensities the analytical approximation is valid even at short circuit.

Parameter description	Symbol	Original value	Fitted value
Photoelectrode parameters			
Normalized electron diffusion coefficient	$D_c n_{c,eq}/d$	$1.80 \cdot 10^8$	$1.81 \cdot 10^8$
Normalized recombination rate coefficient	$k_r n_{c,eq}^{\gamma} d$	$1.29 \cdot 10^{11}$	$0.752 \cdot 10^{11}$
Recombination order	γ	0.7	0.717
Normalized electron equilibrium concentration	$n_{c,eq} d$	$3.0 \cdot 10^4$	0
Normalized trapped electrons at equilibrium	$n_{t,eq} d$	$1.5 \cdot 10^{15}$	$0.635 \cdot 10^{15}$
Trap distribution	β_T	0.3	0.327
Optical parameters			
Normalized total light absorption coefficient	$\alpha_t d$	-1	-1
Light harvesting and injection efficiency	$\eta_{LH}\eta_{INJ}$	0.7	0.689
Normalized dye recombination rate coefficient	$\frac{k_e n_{c,eq}}{k_{REG} c_{red,eq}}$	$4.0 \cdot 10^{-15}$	0
Substrate parameters			
Exchange current density	$i_{0,s}$	$3.00 \cdot 10^{-6}$	$2.93 \cdot 10^{-6}$
Symmetry factor	β_{PE}	0.5	0.504

Table 5.1: Original and fitted parameter values for the simulated dye solar cell.

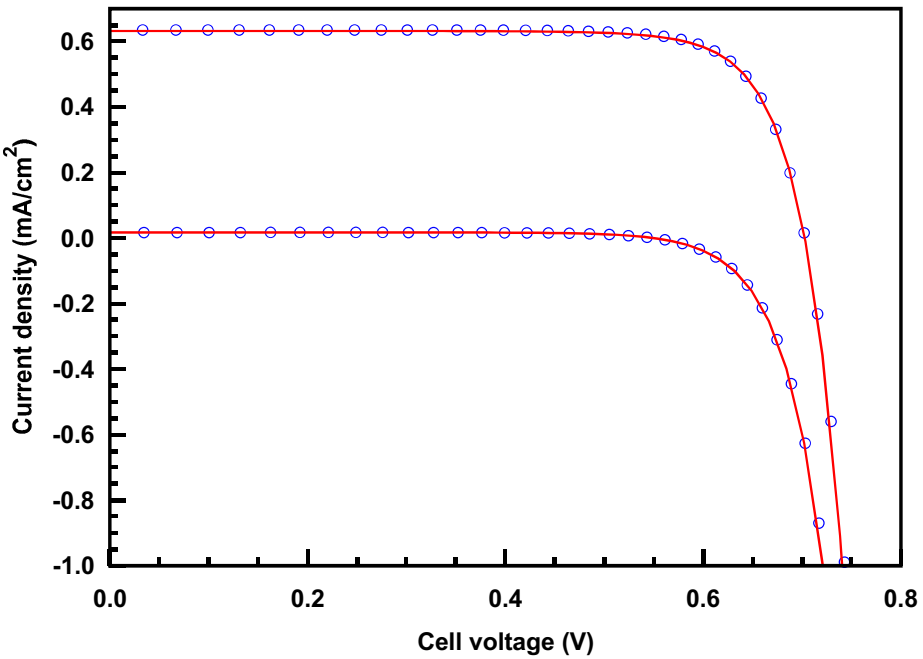

Figure 5-8: Numerically calculated (circles) and analytically recreated (solid line) I-V curves. The simulated incident photon flux for the upper curve is $6.32 \cdot 10^{19}$ $1/(\mathrm{m}^2\mathrm{s})$ and $2.00 \cdot 10^{18}$ $1/(\mathrm{m}^2\mathrm{s})$ for the lower one.

5.3 Results From Experimental Data

After validating the inverse problem solution using simulated data, the method was applied to experimental data obtained from a single dye solar cell.

5.3.1 Experimental

A dye-sensitized solar cell was produced via the following procedure: FTO glass (Aldrich, TEC 15) was cleaned with Milli-RO water (In-house), DECON 90 (Decon), isopropanol (Fisher, LRG) and ethanol (Fisher, ARG). To prepare the photoanode, a blocking layer of TiO_2 was applied to the conducting side of the glass by spray pyrolysis on a hot plate at 400°C using a solution of 0.2M di-isopropoxytitanium bis(acetylacetonate) (Aldrich) in isopropanol. A layer of TiO_2 nanoparticles was then deposited onto this substrate by the doctor blade technique. 2 layers of magic tape (Scotch) were used to mark out a 1 cm wide strip on the glass, and TiO_2 paste (Dyesol, DSL 18NR-T) was applied. This was left in a saturated EtOH atmosphere for 30s then heated at 100°C. The film was then sintered at 500 °C for 30 minutes (in air). Films were dyed by submerging in $3 \cdot 10^{-4}$ M N719 dye (Dyesol) solution with 1:1 t-Butanol (Sigma-Aldrich, 99.7%):Acetonitrile (Fisher, HPLC) mixture used as solvent. Dye-sensitization was conducted overnight (ca. 16 hours) in blacked out containers. All chemicals were used as supplied.

To make the cathode, two 0.6mm diameter holes were drilled into FTO glass (Aldrich, TEC 7) which was then cleaned as described above. Platinum was then deposited by dropping several drops of $5 \cdot 10^{-3}$ M Hexachloroplatinate (Aldrich, 99.995%) solution in isopropanol on the conductive side of the glass. This was then heated at 390°C for 15 minutes. To assemble the cell, a hot-melt Surlyn (Solaronix, SX1170-25PF) gasket was used, and once the two sides were sealed together, a small quantity of electrolyte was introduced through the drilled holes. This consisted of 0.03M I_2 (Aldrich, 99.999%), 0.6M 3-propyl-1-methylimidazolium iodide (Alfa Aesar), 0.1M guanidine thiocyanate (Fluka, 99%) and 0.5M tert-butylpyridine(Aldrich, 99%) in an acetonitrile:valeronitrile (Aldrich) solvent in the ratio 85:15. The open back holes were sealed using Surlyn and a piece of coverslip glass (SLS). Finally, a layer of silver conductive paint (RS Components) was applied to the two electrodes to reduce series resistance. Cell fabrication was conducted by Thomas Risbridger from University of Bath Department of Chemistry.

Impedance spectra were recorded at open circuit using a frequency response analyser (Solartron 1250) connected to a potentiostat (Solartron 1287). Both devices were computer controlled using ZPlot 3.0a software (Scribner Associates). Recorded frequencies were from 65535 Hz to 0.5 Hz and the amplitude of the voltage perturbation was 10 mV. After changing the bias voltage, cell current was monitored for several minutes until the cell could be seen to reach a steady-state. I-V curves were measured before and after EIS measurements using the same setup. Illumination was provided by a green LED (peak emission wavelength at 525nm) powered by a LED custom-built driver. Photon flux data was taken from the voltage supplied to the LED driver. This was calibrated by measuring the emission spectrum of the LED and comparing it to the current output of a silicon photodiode (Thorlabs FDS1010, external quantum

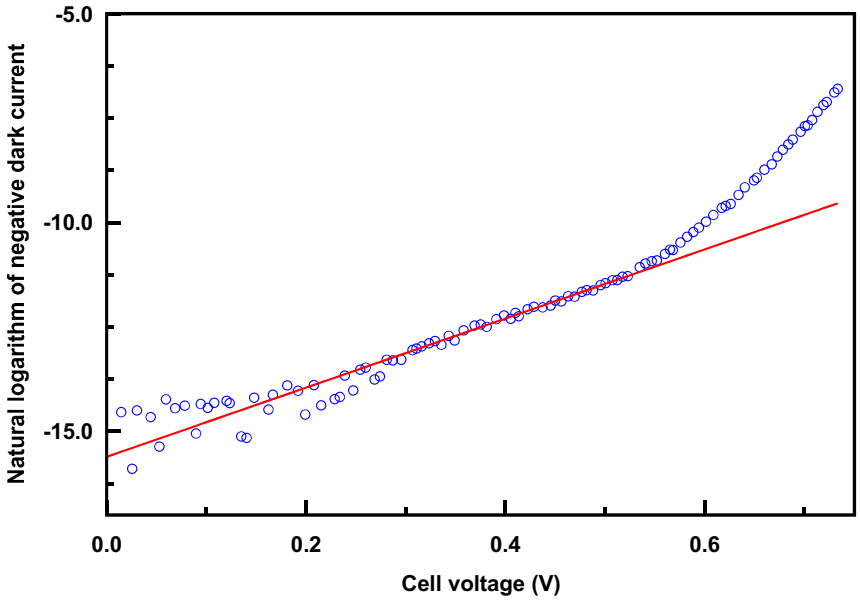

Figure 5-9: Measured (circles) dark current and a fit to equation 5.32 (solid line). At low voltages the current is too low to be measured accurately. At high voltages photoelectrode recombination starts to dominate dark current and equation 5.32 is no longer valid.

efficiency provided by the manufacturer). In order to improve stability, the cell was illuminated at open circuit overnight before measurements.

5.3.2 Substrate Recombination

Figure 5-9 shows the natural logarithm of measured dark current as a function of series resistance corrected cell current as well as the fit to equation 5.32. Unlike in the simulated cell, the substrate resistance values calculated from the fit were so large that they had only a minor effect on the overall differential resistance of the cell at high voltages.

5.3.3 Impedance Spectra

Impedance was measured at open circuit at sixteen different light intensities. Unlike in the simulated case, the experimental cell did not have a separate reference electrode so the impedance model also had to include the counter electrode. Series resistance caused by the FTO glass electrode substrates was also included.

$$Z_{cell} = R_s + Z_{CE} + Z_{PE+SU} \tag{5.35}$$

where Z_{cell} is the overall cell impedance, R_s the substrate series resistance, Z_{CE} counter electrode impedance and Z_{PE+SU} the combined photoelectrode and photoelectrode substrate impedance. Counter electrode impedance was modelled as a simple resistor in parallel with a capacitor.

$$Z_{CE} = \left(\frac{1}{R_{CE}} + i\omega C_{CE} \right)^{-1} \tag{5.36}$$

where R_{CE} is the counter electrode resistance and C_{CE} the capacitance.

At low voltages the substrate capacitance distorts the high frequency part of the impedance spectrum just as predicted in the simulations (see figure 5-10). However, substrate capacitances were fitted to consistent values only at low bias voltages which indicates that the two-electrode measurement cannot accurately distinguish between the various high frequency effects caused by the counter electrode, substrate and electron transport at the photoelectrode.

High voltages also show behaviour predicted by the simulations as at low frequencies the fits underestimated the total differential resistance of the cell possibly indicating a small contribution from electrolyte diffusion (figure 5-11). However, it is also possible that the spectra are somewhat distorted by the distributed series resistance caused by device geometry (see section 4.2.8) or overall heterogeneity of the photoelectrode. The fits could have been improved by replacing the capacitors with constant phase elements [45] but this was considered to be undesirable as the constant phase element contains an additional parameter that has no straightforward physical meaning.

5.3.4 Parameter Values and Recreated J-V Curves

The fitting of the model parameters was conducted in the same way as in the simulated case. The only difference was that fitted recombination resistance values were deemed to be sufficiently reliable to be used in parameter fitting. Therefore recombination resistances were fitted to equations 5.19, 5.20 and 5.31.

Table 5.2 shows the fitted parameter values. The data could be fitted without any recombination to the dye implying that at the measured voltages and light intensities dye regeneration is perfect. The combined light harvesting and injection efficiency was about 77% which is only slightly below the transparency of the conductive glass given by the manufacturer (81% [46]) indicating that generation of free charge is almost ideal in the photoelectrode film. It is also consistent with previous studies of incident photon to collected electron efficiencies at wavelengths corresponding to green light [32].

Measured and fitted circuit element as well as open circuit voltage values are given in figures 5-12, 5-13, 5-14 and 5-15. Model fits are generally quite good, although there appears to be a disagreement between measured and predicted slopes of photoelectrode transport resistance versus open circuit voltage. Considering that transport resistance values are fitted from the impedance spectra, the difference could be due to systematic error in fitting. Another possibility is the resistance of the recombination blocking layer which is ignored in the model.

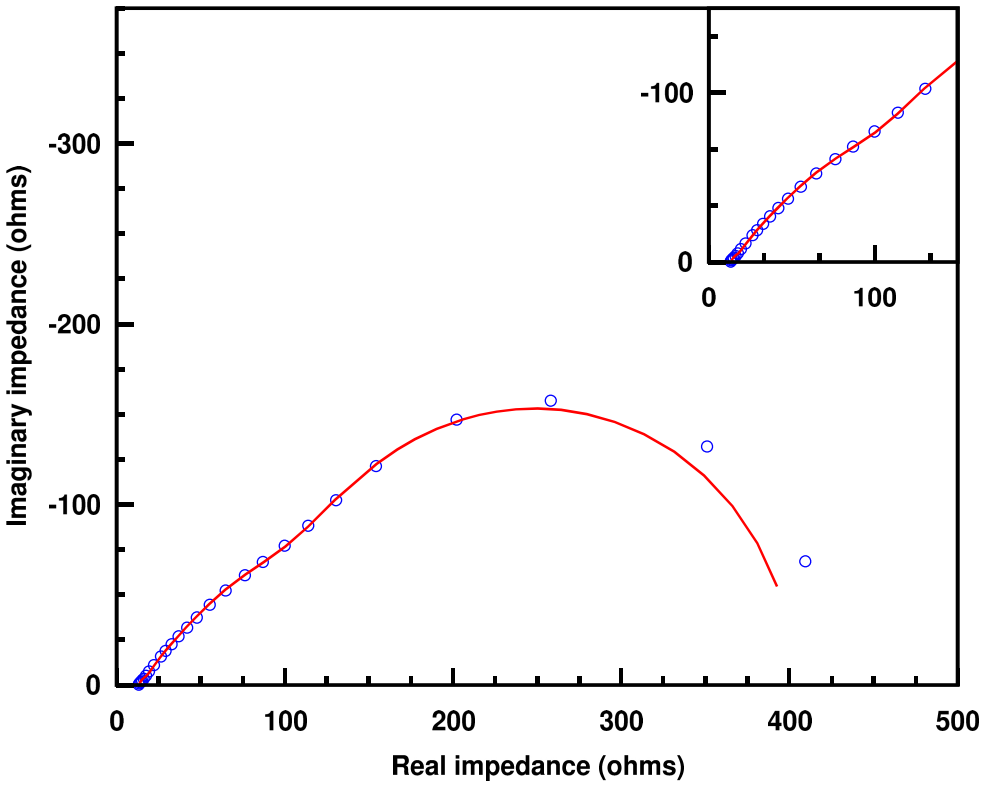

Figure 5-10: Measured (circles) and fitted (solid line) impedance spectrum at 648mV bias voltage. Substrate capacitance is needed to fit the high frequency part of the spectrum (lower left corner and inset).

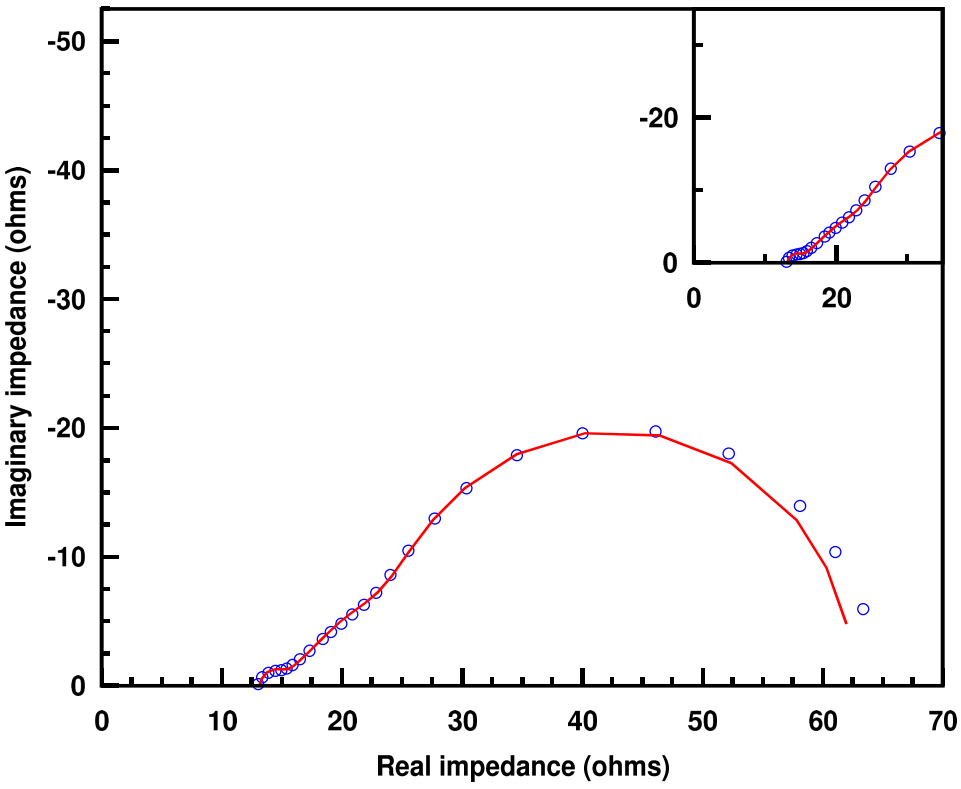

Figure 5-11: Measured (circles) and fitted (solid line) impedance spectrum at 718 mV bias voltage. The low frequency part (lower right corner) of the measured spectrum may indicate some contribution from electrolyte diffusion. Another possibility is that the cell is not homogeneous.

Parameter description	Symbol	Fitted value
Photoelectrode parameters		
Normalized electron diffusion coefficient	$D_c n_{c,eq}/d$	$4.4 \cdot 10^7$
Normalized recombination rate coefficient	$k_r n_{c,eq}^{\gamma} d$	$1.4 \cdot 10^{10}$
Recombination order	γ	0.79
Normalized electron equilibrium concentration	$n_{c,eq} d$	0
Normalized trapped electrons at equilibrium	$n_{t,eq} d$	$3.0 \cdot 10^{15}$
Trap distribution	β_T	0.27
Optical parameters		
Normalized total light absorption coefficient	$\alpha_t d$	-3
Light harvesting and injection efficiency	$\eta_{LH}\eta_{INJ}$	0.77
Normalized dye recombination rate coefficient	$\frac{k_e n_{c,eq}}{k_{REG} c_{red,eq}}$	0
Substrate parameters		
Exchange current density	$i_{0,s}$	$1.7 \cdot 10^{-7}$
Symmetry factor	β_{PE}	0.21
Cell parameters		
Counter electrode resistance	R_{CE}	1.8
Series resistance	R_S	13

Table 5.2: Fitted parameter values for the experimental dye solar cell.

Fitting open circuit voltages to the diode equation (equation 3.3), gives a nonideality factor of 1.38. Impedance data indicates that this is caused by the combination of photoelectrode recombination (nonideality factor of 1.27 calculated from the inverse of the recombination order) and substrate recombination (nonideality factor of 4.76 calculated from the inverse of the symmetry factor).

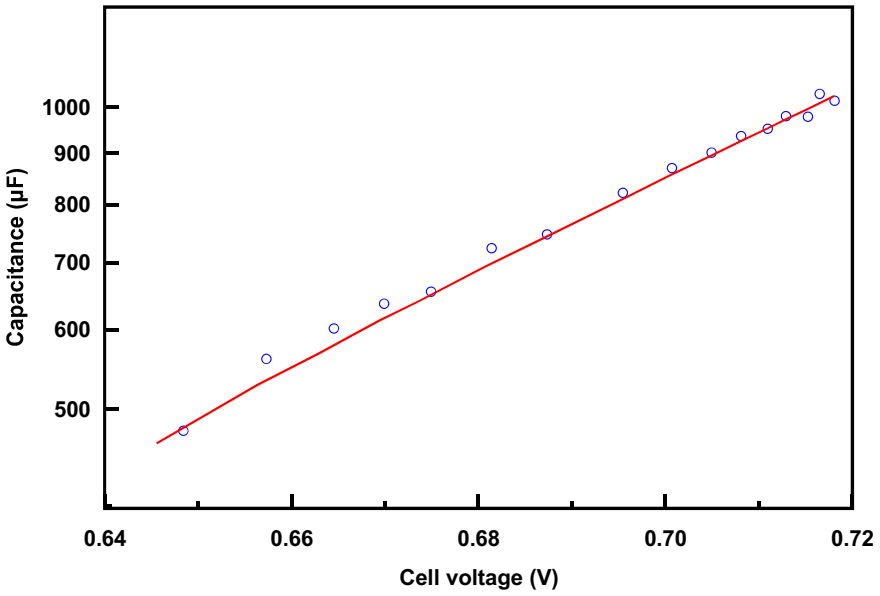

Figure 5-12: Photoelectrode capacitance values derived from impedance measurements (circles) and fit to equation 5.21 (solid line).

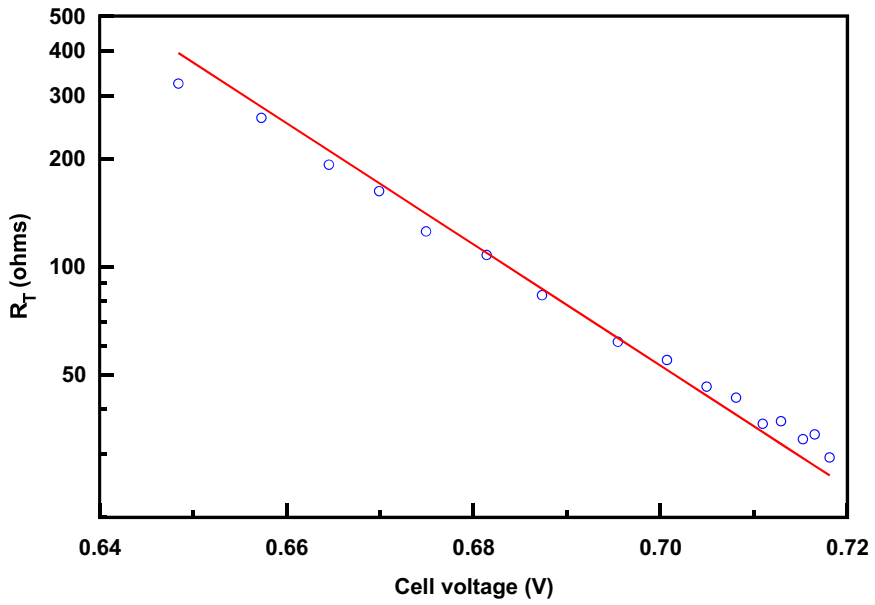

Figure 5-13: Photoelectrode transport resistance values derived from impedance measurements (circles) and fit to equation 5.18 (solid line).

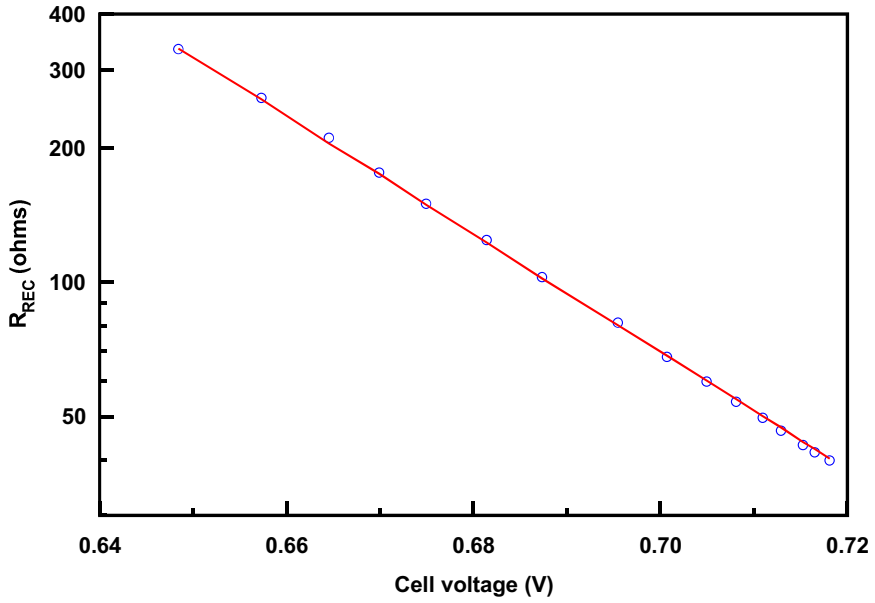

Figure 5-14: Photoelectrode recombination resistance values derived from impedance measurements (circles) and fit to equation 5.31 (solid line).

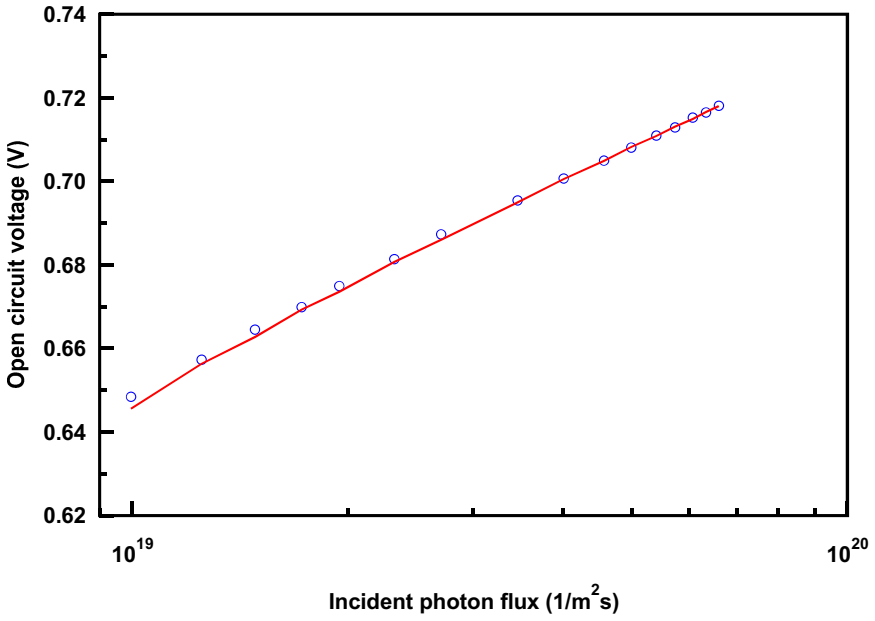

Figure 5-15: Measured (circles) and fitted (solid line) open circuit voltages. A straight line fit (not shown) gives a nonideality factor of 1.38.

Measured and predicted J-V curves for four different light intensities are given in figure 5-16. Although from this figure it would appear that the model is almost perfect in predicting short circuit currents, comparing experimental and predicted IPCE ratios (figure 5-17) shows that this is not the case. Still, the model predictions are very good when taking into account that no short circuit information was used in the fitting. Including this information is very likely to improve results but given how the model is formulated, solving short circuit conditions requires numerical iteration as the boundary conditions specify the sum of cell current and substrate recombination current instead of cell voltage. Therefore short circuit data was not included in the fitting.

At the maximum power point with the highest measured photon flux ($6.61 \cdot 10^{19}$ $1/(\mathrm{m}^2\mathrm{s})$) the model predicts that approximately 76% of generated electrons are collected in the external circuit, whereas about 4% and 21% are lost to substrate and photoelectrode recombination. At higher light intensities the maximum power point voltage increases resulting in substrate recombination becoming even less important. However, it should be noted that the measured cell had much higher transport to recombination resistance ratios than what have been reported in high efficiency cells [14] indicating that for good dye cells electron collection is not limited by the conductivity of the photoelectrode. Therefore in these cells substrate recombination could be the dominant recombination pathway although overall recombination is low.

5.4 Conclusions

In this chapter a simplified dye solar cell model is used to solve the inverse problem posed by the numerical model described in the previous chapter using impedance spectroscopy. Applying the method to experimental data showed good agreement between predicted and measured data indicating that the continuity equation model is an accurate description of the device. The model predicts that the current output of the measured cell is somewhat limited by the conductivity of the photoelectrode, but experimental evidence from others [14] shows that this is not the case in general. The observed nonideal behaviour of open circuit voltage versus light intensity can be explained by a combination of substrate recombination and nonlinear recombination from the photoelectrode.

However, as the simplified model assumes uniform redox ion concentration in the electrolyte, it is only valid at low light intensities and current densities. Therefore an improved model that includes diffusion of ions in the electrolyte is needed to quantify the role electrolyte conductivity and regeneration of dye molecules play in limiting device efficiency.

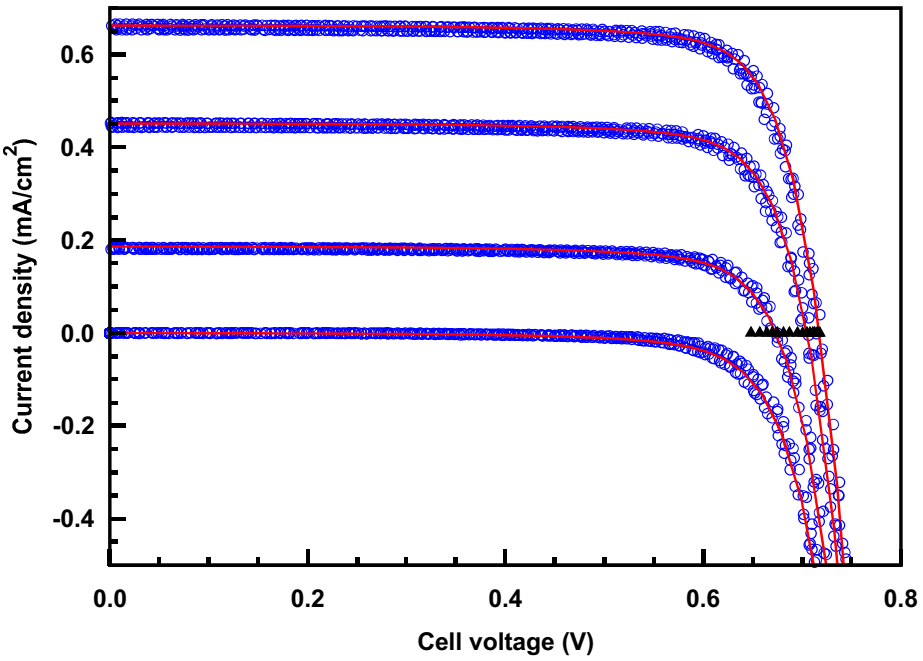

Figure 5-16: Measured (circles) and predicted (solid lines) J-V curves at photon flux values of $6.61 \cdot 10^{19}$, $4.57 \cdot 10^{19}$ and $1.95 \cdot 10^{19}$ $1/(\mathrm{m}^2\mathrm{s})$ as well as in the dark. Open circuit voltages used in fitting the model parameters are shown as filled triangles.

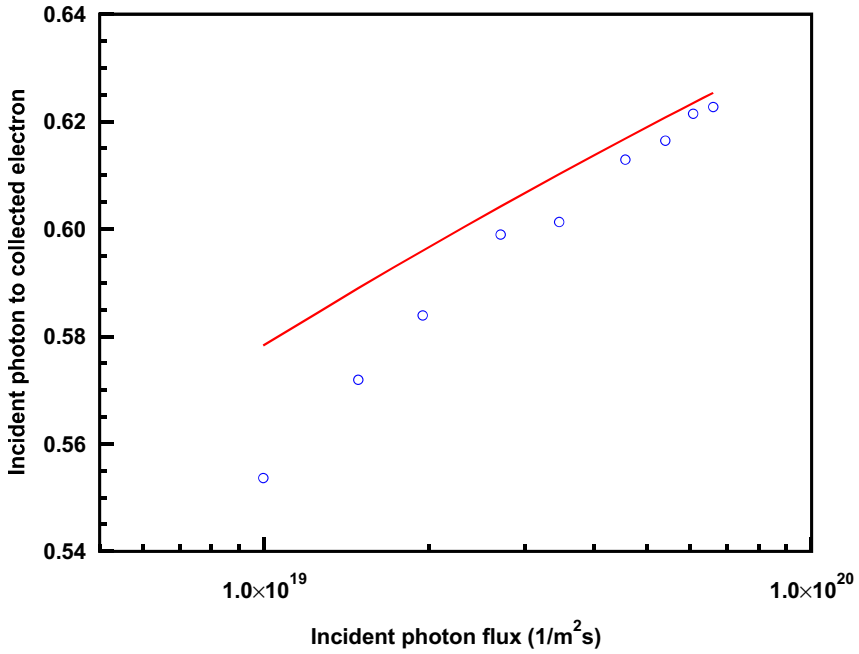

Figure 5-17: Measured (circles) and predicted (solid line) incident photon to collected electron (IPCE) values. Model predictions are close to the measured values but do not replicate the light intensity dependence accurately.

Chapter 6

Solving the Dye-Sensitized Solar Cell Device Model Inverse Problem at High Light Intensities

In the previous chapter the device model inverse problem was solved at low light intensities where diffusion of redox ions in the electrolyte could be ignored. In this chapter the model is improved by taking into account the diffusion of tri-iodide. The cost of this improvement is a significant increase in the complexity of the solutions.

6.1 Theory

6.1.1 Simplified Equations with Tri-iodide Diffusion

The continuity equations are simplified using the same principles as in the previous chapter: non-linear terms are linearized using first-order Taylor approximations. Only the recombination term differs from the previously considered case, the rest can be found in the previous chapter.

The DC approximation is

$$\begin{aligned} & k_r dn_{c,eq}^{\gamma} \cdot c_{ox,DC} \cdot n_{DC}^{\gamma} \\ & \approx k_r dn_{c,eq}^{\gamma} \cdot n_{fg}^{\gamma} \cdot c_{ox,DC} + k_r dn_{c,eq}^{\gamma} \cdot c_{ox,fg} \cdot \gamma \cdot n_{fg}^{\gamma-1} \cdot (n_{DC} - n_{fg}) \end{aligned} \tag{6.1}$$

and the AC one

$$\begin{aligned} & k_r dn_{c,eq}^{\gamma} \cdot c_{ox,AC} \cdot n_{DC}^{\gamma} + k_r dn_{c,eq}^{\gamma} \cdot c_{ox,DC} \cdot \gamma \cdot n_{DC}^{\gamma-1} \cdot n_{AC} \\ & \approx k_r dn_{c,eq}^{\gamma} \cdot c_{ox,AC} \cdot n_{fg}^{\gamma} + k_r dn_{c,eq}^{\gamma} \cdot c_{ox,fg} \cdot \gamma \cdot n_{fg}^{\gamma-1} \cdot n_{AC} \end{aligned} \tag{6.2}$$

where n is the normalized conduction band electron concentration and c_{ox} the normalized tri-iodide concentration. The subscript fg indicates a constant first guess for the concentrations.

The resulting simplified continuity equations are

$$\begin{aligned}
&\frac{D_c n_{c,eq}}{d} \cdot \frac{\partial^2 n_{DC}}{\partial y^2} - k_r d n_{c,eq}^{\gamma} \cdot c_{ox,DC} \cdot n_{fg}^{\gamma} - k_r d n_{c,eq}^{\gamma} \cdot c_{ox,fg} \cdot \gamma n_{fg}^{\gamma-1} \cdot (n_{DC} - n_{fg}) \\
&+ \eta_{LH}\eta_{INJ}\phi \cdot \left(1 + \frac{k_e n_{c,eq}}{k_{REG} c_{red,eq}} \cdot n_{fg}\right)^{-1} \cdot \frac{\alpha_t d}{e^{\alpha_t d} - 1} e^{\alpha_t dy} \\
&- \eta_{LH}\eta_{INJ}\phi \cdot \left(1 + \frac{k_e n_{c,eq}}{k_{REG} c_{red,eq}} \cdot n_{fg}\right)^{-2} \cdot \frac{k_e n_{c,eq}}{k_{REG} c_{red,eq}} \cdot (n_{DC} - n_{fg}) = 0
\end{aligned} \tag{6.3}$$

$$\begin{aligned}
&\frac{D_{ox} c_{ox,eq}}{S_{ox} d} \cdot \frac{\partial^2 c_{ox,DC}}{\partial y^2} - k_r d n_{c,eq}^{\gamma} \cdot c_{ox,DC} \cdot n_{fg}^{\gamma} - k_r d n_{c,eq}^{\gamma} \cdot c_{ox,fg} \cdot \gamma n_{fg}^{\gamma-1} \cdot (n_{DC} - n_{fg}) \\
&+ \eta_{LH}\eta_{INJ}\phi \cdot \left(1 + \frac{k_e n_{c,eq}}{k_{REG} c_{red,eq}} \cdot n_{fg}\right)^{-1} \cdot \frac{\alpha_t d}{e^{\alpha_t d} - 1} e^{\alpha_t dy} \\
&- \eta_{LH}\eta_{INJ}\phi \cdot \left(1 + \frac{k_e n_{c,eq}}{k_{REG} c_{red,eq}} \cdot n_{fg}\right)^{-2} \cdot \frac{k_e n_{c,eq}}{k_{REG} c_{red,eq}} \cdot (n_{DC} - n_{fg}) = 0
\end{aligned} \tag{6.4}$$

for the DC case and

$$\begin{aligned}
&\left(n_{c,eq} d + n_{t,eq} d \beta_T \cdot n_{fg}^{\beta_T - 1}\right) \cdot \frac{\partial n_{AC}}{\partial t} = \frac{D_c n_{c,eq}}{d} \cdot \frac{\partial^2 n_{AC}}{\partial y^2} \\
&- k_r d n_{c,eq}^{\gamma} \cdot c_{ox,AC} \cdot n_{fg}^{\gamma} - k_r d n_{c,eq}^{\gamma} \cdot c_{ox,fg} \cdot \gamma \cdot n_{fg}^{\gamma-1} n_{AC} \\
&+ \eta_{LH}\eta_{INJ}\phi \cdot \left(1 + \frac{k_e n_{c,eq}}{k_{REG} c_{red,eq}} \cdot n_{fg}\right)^{-2} \cdot \frac{k_e n_{c,eq} n_{AC}}{k_{REG} c_{red,eq}}
\end{aligned} \tag{6.5}$$

$$\begin{aligned}
&\frac{c_{ox,eq} d}{S_{ox}} \cdot \frac{\partial c_{ox,AC}}{\partial t} = \frac{D_{ox} c_{red,eq}}{S_{ox} d} \cdot \frac{\partial^2 c_{ox,AC}}{\partial y^2} - k_r d n_{c,eq}^{\gamma} \cdot c_{ox,AC} \cdot n_{fg}^{\gamma} \\
&- k_r d n_{c,eq}^{\gamma} \cdot \gamma \cdot c_{ox,fg} \cdot n_{fg}^{\gamma-1} n_{AC} \\
&- \eta_{LH}\eta_{INJ}\phi \cdot \left(1 + \frac{k_e n_{c,eq}}{k_{REG} c_{red,eq}} \cdot n_{fg}\right)^{-2} \cdot \frac{k_e n_{c,eq}}{k_{REG} c_{red,eq}} \cdot n_{AC}
\end{aligned} \tag{6.6}$$

for the AC one.

The first guess for electron concentration is again calculated by assuming that it is constant and integrating over the film thickness. However, now the recombination term includes the tri-iodide concentration as well.

$$\int_0^1 \Big\{ - k_r d n_{eq}^{\gamma} c_{ox,fg} n_{fg}^{\gamma} + \eta_{REG,0} \left(1 + \gamma - \gamma \eta_{REG,0}\right) \cdot \frac{\phi \eta_{LH} \eta_{INJ} \alpha_t d}{e^{\alpha_t d} - 1} e^{\alpha_t dy}$$
$$- \eta_{REG,0}^2 \cdot \left(\frac{1}{\eta_{REG,0}} - 1 \right)^{1-\gamma} \cdot \left(\frac{k_e n_{c,eq}}{k_{REG} c_{red,eq}} \right)^{\gamma} \cdot \frac{n_{fg}^{\gamma}}{\gamma} \cdot \frac{\phi \eta_{LH} \eta_{INJ} \alpha_t d}{e^{\alpha_t d} - 1} e^{\alpha_t dy} \Big\} dy$$
$$= \frac{I_{cell} + I_{surf}}{q A_{cell}}$$
$$\Rightarrow n_{fg} = \left(\frac{\phi \eta_{LH} \eta_{INJ} \cdot \left(1 + \gamma - \gamma \eta_{REG,0}\right) - \frac{I_{cell} + I_{surf}}{q A_{cell}}}{k_r d n_{c,eq}^{\gamma} c_{ox,fg} + \eta_{REG,0}^2 \cdot \left(\frac{1}{\eta_{REG,0} - 1} \right)^{1-\gamma} \cdot \left(\frac{k_e n_{c,eq}}{k_{REG} c_{red,eq}} \right)^{\gamma} \cdot \frac{\phi \eta_{LH} \eta_{INJ}}{\gamma}} \right)^{\frac{1}{\gamma}} \tag{6.7}$$

The first guess for tri-iodide concentration is a little more complicated. It is calculated by assuming a constant recombination term and noting that substracting total recombination (both from the photoelectrode and substrate) from total generation yields cell current.

$$\int_0^1 \Big\{ - k_r d n_{eq}^{\gamma} c_{ox,fg} n_{fg}^{\gamma} + \eta_{REG,0} \left(1 + \gamma - \gamma \eta_{REG,0}\right) \cdot \frac{\phi \eta_{LH} \eta_{INJ} \alpha_t d}{e^{\alpha_t d} - 1} e^{\alpha_t dy} \Big\} dy = \frac{I_{cell} + I_{surf}}{q A_{cell}}$$
$$\Rightarrow k_r d n_{eq}^{\gamma} c_{ox,fg} n_{fg}^{\gamma} = \eta_{REG,0} \left(1 + \gamma - \gamma \eta_{REG,0}\right) \phi \eta_{LH} \eta_{INJ} - \frac{I_{cell} + I_{surf}}{q A_{cell}} \tag{6.8}$$

This simplifies the continuity equation for tri-iodide to

$$\frac{D_{ox} c_{ox,eq}}{S_{ox} d} \cdot \frac{\partial^2 c_{ox,fx,y}}{\partial y^2} - \eta_{REG,0} \left(1 + \gamma - \gamma \eta_{REG,0}\right) \phi \eta_{LH} \eta_{INJ} + \frac{I_{cell} + I_{surf}}{q A_{cell}}$$
$$\eta_{REG,0} \left(1 + \gamma - \gamma \eta_{REG,0}\right) \cdot \frac{\phi \eta_{LH} \eta_{INJ} \alpha_t d}{e^{\alpha_t d} - 1} e^{\alpha_t dy} = 0 \tag{6.9}$$

where $c_{ox,fg,y}$ is the first guess tri-iodide concentration that has not yet been set to a constant by averaging.

The boundary conditions, the same as given in chapter 4, require solution also in the free electrolyte layer. Using these, the overall solution is

$$c_{ox,fg,y}(y) = Ay^2 + By + Ce^{\alpha_t dy} + E \tag{6.10}$$

where

$$A = \frac{1}{2} \cdot \frac{S_{ox} d}{D_{ox} c_{ox,eq}} \cdot \left(\eta_{REG,0} \left(1 + \gamma - \gamma \eta_{REG,0}\right) \phi \eta_{LH} \eta_{INJ} - \frac{I_{cell} + I_{surf}}{q A_{cell}} \right) \tag{6.11}$$

$$B = \frac{I_{surf}}{q A_{cell}} \cdot \frac{S_{ox} d}{D_{ox} c_{ox,eq}} \tag{6.12}$$

$$C = -\frac{S_{ox}d}{D_{ox}c_{ox,eq}} \cdot \frac{1}{\alpha_t d} \cdot \frac{\eta_{LH}\eta_{INJ}\phi}{e^{\alpha_t d}-1} \cdot \eta_{REG,0}\left(1+\gamma-\gamma\eta_{REG,0}\right) \tag{6.13}$$

$$\begin{aligned} E = c_{ox,eq} + \left(P+\frac{d_{el}}{d}\right)^{-1} \cdot \Bigg(& -A\left(\frac{P}{3}+\frac{d_{el}}{d}\right) - B\left(\frac{P}{2}+\frac{d_{el}}{d}\right) \\ & - C\left(P\cdot\frac{e^{\alpha_t d}-1}{\alpha_t d} + e^{\alpha_t d}\cdot\frac{d_{el}}{d}\right) + \frac{I_{cell}}{qA_{cell}} \cdot \frac{S_{ox}d}{D_{ox}c_{ox,eq}} \cdot \frac{1}{2} \cdot \left(\frac{d_{el}}{d}\right)^2 \Bigg) \end{aligned} \tag{6.14}$$

The substrate recombination current is calculated from the solution, so at first it must be guessed. In this report, the first guess is zero.

The first guess tri-iodide concentration $c_{ox,fg}$ must be constant in order to keep the solutions manageable. Therefore the average of the position-dependent first guess $c_{ox,fg,y}$ is used.

$$c_{ox,fg} = \int_0^1 c_{ox,fg,y}(y)\,dy = \frac{A}{3} + \frac{B}{2} + C\cdot\frac{e^{\alpha_t d}-1}{\alpha_t d} + E \tag{6.15}$$

6.1.2 DC Solution

Using the boundary conditions found in chapter 4 (analytical solutions use the current boundary condition at the photoelectrode substrate), the solutions to the simplified DC equations are

$$n_{DC} = A_n\sinh(ay) + B_n\cosh(ay) + C_n e^{\alpha_t dy} + F_n y + H_n \tag{6.16}$$

$$c_{ox,DC} = A_{ox}\sinh(ay) + B_{ox}\cosh(ay) + C_{ox} e^{\alpha_t dy} + F_{ox} y + H_{ox} \tag{6.17}$$

$$c_{ox,F,DC} = A_{ox,F}(y-1) + B_{ox,F,DC} \tag{6.18}$$

where

$$a = \sqrt{\left(\frac{d}{\lambda_n}\right)^2 + \left(\frac{d}{\lambda_{ox}}\right)^2} \tag{6.19}$$

$$\frac{\lambda_n}{d} = \sqrt{\frac{D_c n_{c,eq}}{d}\left(k_r d n_{c,eq}^{\gamma} c_{ox,fg}\gamma n_{fg}^{\gamma-1} + \eta_{LH}\eta_{INJ}\phi\cdot\left(1+\frac{k_e n_{c,eq}\cdot n_{fg}}{k_{REG}c_{red,eq}}\right)^{-2}\cdot\frac{k_e n_{c,eq}}{k_{REG}c_{red,eq}}\right)^{-1}} \tag{6.20}$$

$$\frac{\lambda_{ox}}{d} = \sqrt{\frac{D_{ox}c_{ox,eq}}{S_{ox}d}\cdot\frac{1}{k_r d n_{c,eq}^{\gamma} n_{fg}^{\gamma}}} \tag{6.21}$$

$$A_n = \frac{1}{a}\cdot\left(\frac{I_{cell}+I_{surf}}{qA_{cell}}\cdot\frac{d}{D_c n_{c,eq}} - \alpha_t d C_n - F_n\right) \tag{6.22}$$

$$B_n = -\frac{A_n}{\tanh(a)} - C_n \cdot \frac{\alpha_t d e^{\alpha_t d}}{a \sinh(a)} - \frac{F_n}{a \sinh(a)} \tag{6.23}$$

$$C_n = -\frac{d}{D_c n_{c,eq}} \cdot \eta_{LH}\eta_{INJ}\phi \cdot \left(1 + \frac{k_e n_{c,eq} \cdot n_{fg}}{k_{REG} c_{red,eq}}\right)^{-1} \cdot \frac{1}{\alpha_t d} \cdot \frac{1}{e^{\alpha_t d} - 1} \tag{6.24}$$

$$F_n = -\frac{D_{ox} c_{ox,eq}}{S_{ox} d} \cdot \frac{d}{D_c n_{c,eq}} \cdot \left(\frac{\lambda_n}{d}\right)^2 \cdot \left(\frac{d}{\lambda_{ox}}\right)^2 \cdot F_{ox} \tag{6.25}$$

$$H_n = n_{fg} - \frac{D_{ox} c_{ox,eq}}{S_{ox} d} \cdot \frac{d}{D_c n_{c,eq}} \cdot \left(\frac{\lambda_n}{d}\right)^2 \cdot \left(\frac{d}{\lambda_{ox}}\right)^2 \cdot H_{ox} \tag{6.26}$$

$$A_{ox} = \frac{S_{ox} d}{D_{ox} c_{ox,eq}} \cdot \frac{D_c n_{c,eq}}{d} \cdot A_n \tag{6.27}$$

$$B_{ox} = \frac{S_{ox} d}{D_{ox} c_{ox,eq}} \cdot \frac{D_c n_{c,eq}}{d} \cdot B_n \tag{6.28}$$

$$C_{ox} = -\frac{S_{ox} d}{D_{ox} c_{ox,eq}} \cdot \eta_{LH}\eta_{INJ}\phi \cdot \left(1 + \frac{k_e n_{c,eq} \cdot n_{fg}}{k_{REG} c_{red,eq}}\right)^{-1} \cdot \frac{1}{\alpha_t d} \cdot \frac{1}{e^{\alpha_t d} - 1} \tag{6.29}$$

$$F_{ox} = -\left(1 + \left(\frac{\lambda_n}{d}\right)^2 \cdot \left(\frac{d}{\lambda_{ox}}\right)^2\right)^{-1} \cdot \frac{I_{cell}}{q A_{cell}} \cdot \frac{S_{ox} d}{D_{ox} c_{ox,eq}} \tag{6.30}$$

$$\begin{aligned} H_{ox} = 1 + \left(P + \frac{d_{el}}{d}\right)^{-1} \cdot \Bigg(& - A_{ox} \left(\frac{P}{a}(\cosh(a) - 1) + \frac{d_{el}}{d} \cdot \sinh(a)\right) \\ & - B_{ox} \left(\frac{P}{A} \sinh(a) + \frac{d_{el}}{d} \cdot \cosh(a)\right) - C_{ox} \left(\frac{P}{\alpha_t d}\left(e^{\alpha_t d} - 1\right)\right) - \frac{F_{ox}}{2} \cdot \left(\frac{d_{el}}{d}\right)^2 \Bigg) \end{aligned} \tag{6.31}$$

$$A_{ox,F} = -\frac{I_{cell}}{q A_{cell}} \cdot \frac{S_{ox} d}{D_{ox,F} c_{ox,eq}} \tag{6.32}$$

$$B_{ox,F} = A_{ox} \sinh(a) + B_{ox} \cosh(a) + C_{ox} e^{\alpha_t d} + F_{ox} + H_{ox} \tag{6.33}$$

6.1.3 AC Solution

The AC solution is so complicated that before giving the solutions, the equations are simplified further by expressing them in terms of voltages and equivalent circuit elements.

Multiplying both continuity equations with qA_{cell} and defining

$$R_{REC,E} = \frac{k_B T}{q^2 A_{cell}} \cdot \frac{n_{fg}^{1-\gamma}}{k_r d n_{c,eq}^{\gamma} c_{ox,fg}} \cdot \frac{1}{\gamma n_{DC}(y = 0)} \tag{6.34}$$

$$R_{T,ox} = \frac{1}{qA_{cell}} \cdot \frac{k_B T}{q} \cdot \frac{S_{ox} d}{D_{ox} c_{ox,eq}} \tag{6.35}$$

$$R_{REC,ox} = \frac{1}{qA_{cell}} \cdot \frac{k_B T}{q} \cdot \frac{1}{k_r d n_{c,eq}^{\gamma} n_{fg}^{\gamma}} \tag{6.36}$$

$$C_{ox} = qA_{cell} \cdot \frac{q}{k_B T} \cdot \frac{c_{ox,eq} d}{S_{ox}} \tag{6.37}$$

$$V_{ox} = \frac{k_B T}{q} \cdot c_{ox,AC} \tag{6.38}$$

the continuity equations become

$$C_T \cdot \frac{\partial V_{AC}}{\partial t} = \frac{1}{R_T} \cdot \frac{\partial^2 V_{AC}}{\partial y^2} - \frac{V_{AC}}{R_{REC}} - \frac{V_{ox}}{R_{REC,ox}} \tag{6.39}$$

$$C_{ox} \cdot \frac{\partial V_{ox}}{\partial t} = \frac{1}{R_{T,ox}} \cdot \frac{\partial^2 V_{ox}}{\partial y^2} - \frac{V_{AC}}{R_{REC}} - \frac{V_{ox}}{R_{REC,ox}} \tag{6.40}$$

V_{AC}, R_T, R_{REC} and C_T are defined in equations 4.103 (as $V_{PE,AC}$), 5.18, 5.31, 5.21, respectively.

The free electrolyte layer equation for tri-iodide becomes

$$C_{ox} \cdot \frac{\partial V_{ox,F}}{\partial t} = \frac{D_{ox,F}}{D_{ox} \cdot R_{T,ox}} \cdot \frac{\partial^2 V_{ox,F}}{\partial y^2} \tag{6.41}$$

The boundary conditions become

$$\frac{1}{R_T} \cdot \frac{\partial V_{AC}}{\partial y}(y = 0) = I_{cell,AC} + I_{surf,AC} \tag{6.42}$$

$$\frac{1}{R_T} \cdot \frac{\partial V_{AC}}{\partial y}(y = 1) = 0 \tag{6.43}$$

$$\frac{1}{R_{T,ox}} \cdot \frac{\partial V_{ox}}{\partial y}(y = 0) = I_{surf} \tag{6.44}$$

$$V_{ox}(y = 1) = V_{ox,F}(y = 1) \tag{6.45}$$

$$\frac{1}{R_{T,ox}} \cdot \frac{\partial V_{ox}}{\partial y}(y = 1) = \frac{D_{ox,F}}{D_{ox} \cdot R_{T,ox}} \cdot \frac{\partial V_{ox,F}}{\partial y}(y = 1) \tag{6.46}$$

$$\frac{D_{ox,F}}{D_{ox} \cdot R_{T,ox}} \cdot \frac{\partial V_{ox}}{\partial y}(y = 1 + \frac{d_{el}}{d}) = -I_{cell} \tag{6.47}$$

The solutions are

$$V_{AC} = \Big(A_n \sinh(a_1 y) + B_n \cosh(a_1 y) + E_n \sinh(a_2 y) + F_n \cosh(a_2 y)\Big) \cdot e^{i\omega t} \tag{6.48}$$

$$V_{ox} = \Big(A_{ox} \sinh(a_1 y) + B_{ox} \cosh(a_1 y) + E_{ox} \sinh(a_2 y) + F_{ox} \cosh(a_2 y)\Big) \cdot e^{i\omega t} \tag{6.49}$$

$$V_{ox,F} = \Big(A_{ox,F} \sinh(a_F(y-1)) + B_{ox,F} \cosh(a_F(y-1))\Big) \cdot e^{i\omega t} \tag{6.50}$$

where

$$a_1 = \frac{-M + \sqrt{M^2 + 4N}}{2} \tag{6.51}$$

$$a_2 = \frac{-M - \sqrt{M^2 + 4N}}{2} \tag{6.52}$$

$$M = \frac{R_{T,ox}}{R_{REC,ox}} + i\omega C_{ox} R_{T,ox} + \frac{R_T}{R_{REC}} + i\omega C_T R_T \tag{6.53}$$

$$N = \frac{R_T}{R_{REC}} \cdot \frac{R_{T,ox}}{R_{REC,ox}} \tag{6.54}$$

$$X_1 = \frac{a_1}{R_T} - \frac{1}{R_{REC}} - i\omega C_T \tag{6.55}$$

$$X_2 = \frac{a_2}{R_T} - \frac{1}{R_{REC}} - i\omega C_T \tag{6.56}$$

$$A_n = A_{ox} \cdot \frac{1}{X_1 R_{REC,ox}} \tag{6.57}$$

$$B_n = B_{ox} \cdot \frac{1}{X_1 R_{REC,ox}} \tag{6.58}$$

$$E_n = E_{ox} \cdot \frac{1}{X_2 R_{REC,ox}} \tag{6.59}$$

$$F_n = F_{ox} \cdot \frac{1}{X_2 R_{REC,ox}} \tag{6.60}$$

$$A_{ox} = \frac{R_{REC,ox}}{a_1} \cdot \left(\frac{1}{X_1} - \frac{1}{X_2}\right)^{-1} \cdot \left(R_T(I_{cell,AC} + I_{surf,AC}) - \frac{R_{T,ox} I_{surf,AC}}{R_{REC,ox} X_2}\right) \tag{6.61}$$

$$B_{ox} = -A_{ox} - E_{ox} \cdot \frac{X_1}{X_2} \cdot \frac{a_2 \cosh(a_2)}{a_1 \sinh(a_1)} - F_{ox} \cdot \frac{X_1}{X_2} \cdot \frac{a_2 \sinh(a_2)}{a_1 \sinh(a_1)} \tag{6.62}$$

$$E_{ox} = \frac{R_{T,ox} I_{surf,AC}}{a_2} - A_{ox} \cdot \frac{a_1}{a_2} \tag{6.63}$$

$$\begin{aligned} F_{ox} = & \left(a_2 \sinh(a_2) + a_F \tanh(a_F \frac{d_{el}}{d}) - \frac{X_1 a_2 \sinh(a_2)}{X_2 a_1 \sinh(a_1)} \cdot \left(a_1 \sinh(a_1) + a_F \tanh(a_F \frac{d_{el}}{d}) \right) \right)^{-1} \\ & \cdot \Bigg(- E_{ox} \left(a_2 \cosh(a_2) + a_F \tanh(a_F \frac{d_{el}}{d}) \right) - A_{ox} \left(a_1 \cosh(a_1) + a_F \tanh(a_F \frac{d_{el}}{d}) \right) \\ & + \left(A_{ox} + E_{ox} \cdot \frac{X_1}{X_2} \cdot \frac{a_2 \cosh(a_2)}{a_1 \cosh(a_1)} \right) \cdot \left(a_1 \sinh(a_1) + a_F \tanh(a_F \frac{d_{el}}{d}) \right) \\ & - I_{cell,AC} R_{T,ox} \cdot \frac{D_{ox}}{D_{ox,F}} \cdot \frac{1}{\cosh(a_F \frac{d_{el}}{d})} \Bigg) \end{aligned} \tag{6.64}$$

$$a_F = \sqrt{i\omega C_{ox} R_{T,ox} \cdot \frac{D_{ox,F}}{D_{ox}}} \tag{6.65}$$

$$A_{ox,F} = -I_{cell} R_{T,ox} \cdot \frac{D_{ox}}{D_{ox,F}} \cdot \frac{1}{a_F \cosh(a_F \frac{d_{el}}{d})} - B_{ox} \tanh(a_F \frac{d_{el}}{d}) \tag{6.66}$$

$$B_{ox,F} = A_{ox} \sinh(a_1) + B_{ox} \cosh(a_1) + E_{ox} \sinh(a_2) + F_{ox} \cosh(a_2) \tag{6.67}$$

Now that diffusion of tri-iodide in the electrolyte is taken into account, the redox potential of the electrolyte is no longer the same as in equilibrium. Therefore reference electrode potential should be taken into account in the voltage modelling.

Reference electrode potential is

$$\begin{aligned} V_{REF} &= \frac{k_B T}{q} \cdot \left(\frac{c_{red,AC}}{c_{red,DC}} + \frac{1}{2} \left(- \frac{c_{ox,AC}}{c_{ox,DC}} + \frac{c_{red,AC}}{c_{red,DC}} \right) \right) \\ &= - \frac{k_B T}{q} \cdot \frac{1}{2 c_{ox,DC}} \cdot \left(A_{ox,F} \sinh(a_F \frac{d_{el}}{d}) + B_{ox,F} \cosh(a_F \frac{d_{el}}{d}) \right) \end{aligned} \tag{6.68}$$

where iodide concentration has been assumed to be the same as in equilibrium.

The impedance becomes

$$Z_{PE+SU,EL} = - \frac{V_{AC} - V_{REF}}{I_{cell,AC}} \tag{6.69}$$

Note that substrate recombination affects voltage through the current term $I_{surf,AC}$ which must be determined through equation 4.103. In this report the model is simplified by setting substrate recombination current to zero in the continuity equations and placing a substrate impedance element in parallel with the photoelectrode impedance element. In effect this means

that substrate recombination current is not taken into account in the tri-iodide concentration.

$$Z_{PE+SU,EL} \approx \left(\frac{1}{Z_{PE,EL}} + \frac{1}{Z_{SU}} \right)^{-1} \tag{6.70}$$

where $Z_{PE,EL}$ refers to $Z_{PE+SU,EL}$ of equation 6.69 with $I_{surf,AC} = 0$. Substrate capacitance was already omitted in the original numerical model but later added via the same parallel element (see sections 4.2.13 and 4.2.16).

6.1.4 Tri-iodide Diffusion Coefficients in the Photoelectrode and Free Electrolyte Layer

In addition to the circuit elements, the analytical solution also requires the ratio of tri-iodide diffusion coefficients in the photoelectrode pores and free electrolyte layer. Although in principle this information is contained in the impedance data, in practice the data is not detailed enough to obtain this value. Fortunately measurement of diffusion limited currents can be used to determine the diffusion coefficient ratio assuming one knows the thicknesses of the layers and the porosity of the photoelectrode. Photoelectrode thickness can be measured mechanically using a profiler whereas the free electrolyte layer thickness depends on the thickness of the gasket used to separate the two electrodes. Porosity can be measured by nitrogen adsorption. The necessary assumption for this measurement is that tri-iodide (or in general the oxidized redox ion) is the ion that limits current flow.

At a very high forward bias in the dark recombination current is so high that the photoelectrode film pores are completely empty of tri-iodide and all ions coming near the back wall of the electrode are immediately reduced to iodide. In this case current flow is determined by diffusion in the free electrolyte layer.

At steady-state the tri-iodide concentration gradient is constant. Requiring that the overall number of tri-iodide ions is conserved, the concentration must integrate to the same number as at equilibrium.

$$\begin{aligned} &\int_1^{1+\frac{d_{el}}{d}} \frac{\partial c_{ox,F,DC}}{\partial y}\, dy = P + \frac{d_{el}}{d} \\ &\Rightarrow \frac{\partial c_{ox,F,DC}}{\partial y} = \left(P + \frac{d_{el}}{d} \right) \cdot \frac{d}{d_{el}} \end{aligned} \tag{6.71}$$

where $c_{ox,F,DC}$ is the normalized tri-iodide concentration in the free electrolyte layer. Converting the gradient into current yields

$$I_{max,fb} = -qA_{cell} \cdot \frac{D_{ox,F} c_{ox,eq}}{S_{ox} d} \cdot \frac{\partial c_{ox,DC}}{\partial y} = -qA_{cell} \cdot \frac{D_{ox,F} c_{ox,eq}}{S_{ox} d} \cdot \left(P + \frac{d_{el}}{d} \right) \cdot \frac{d}{d_{el}} \tag{6.72}$$

At a high reverse bias all current passes through the photoelectrode substrate because

electrons cannot jump to the semiconductor conduction band due to a very large energy barrier. In this case the continuity equation of tri-iodide gives

$$\frac{\partial c_{ox,F,DC}}{\partial y} = -\left(P + \frac{d_{el}}{d}\right) \cdot \left(P + \frac{d_{el}}{d} + P \cdot \frac{D_{ox}}{D_{ox,F}}\right)^{-1} \tag{6.73}$$

$$\begin{aligned} I_{max,rb} &= -qA_{cell} \cdot \frac{D_{ox,F} c_{ox,eq}}{S_{ox} d} \cdot \frac{\partial c_{ox,DC}}{\partial y} \\ &= qA_{cell} \cdot \frac{D_{ox,F} c_{ox,eq}}{S_{ox} d} \cdot \left(P + \frac{d_{el}}{d}\right) \cdot \left(P + \frac{d_{el}}{d} + P \cdot \frac{D_{ox}}{D_{ox,F}}\right)^{-1} \end{aligned} \tag{6.74}$$

The ratio is

$$\frac{I_{max,fb}}{I_{max,rb}} = -\frac{d}{d_{el}} \cdot \left(P + \frac{d_{el}}{d} + P \cdot \frac{D_{ox}}{D_{ox,F}}\right) \tag{6.75}$$

6.1.5 Counter Electrode Overpotential

In the previous chapter counter electrode voltage loss was modelled as a simple resistor as this is a valid approximation at low current densities. At higher currents, however, the full model should be used. This requires a model for the redox ion concentrations which is already described above as well as measurements of the exchange current and symmetry factor.

In this report symmetry factor is simply assumed to be 0.5 whereas the exchange current can be obtained from the counter electrode impedance arc. At open circuit the counter electrode differential resistance is

$$R_{CE} = \frac{\partial V_{CE}}{\partial I_{cell}} = \frac{k_B T}{q} \cdot \frac{1}{i_0 A_{cell}} \tag{6.76}$$

where i_0 is the exchange current.

6.2 Results From Simulated Data

As in the previous chapter, the inverse solution was validated using numerically simulated data. In addition to the five impedance data points used in the previous chapter, seven new data points were added using the full numerical solver. Again, it was assumed that photoelectrode and counter electrode responses could be measured separately by using a reference electrode. Photoelectrode porosity and thickness, free electrolyte layer thickness and ratio of tri-iodide diffusion coefficients in the photoelectrode pores and free electrolyte layer were assumed to be known (the numerical model could not be solved at extreme current densities which meant that the limiting current measurement could not be modelled).

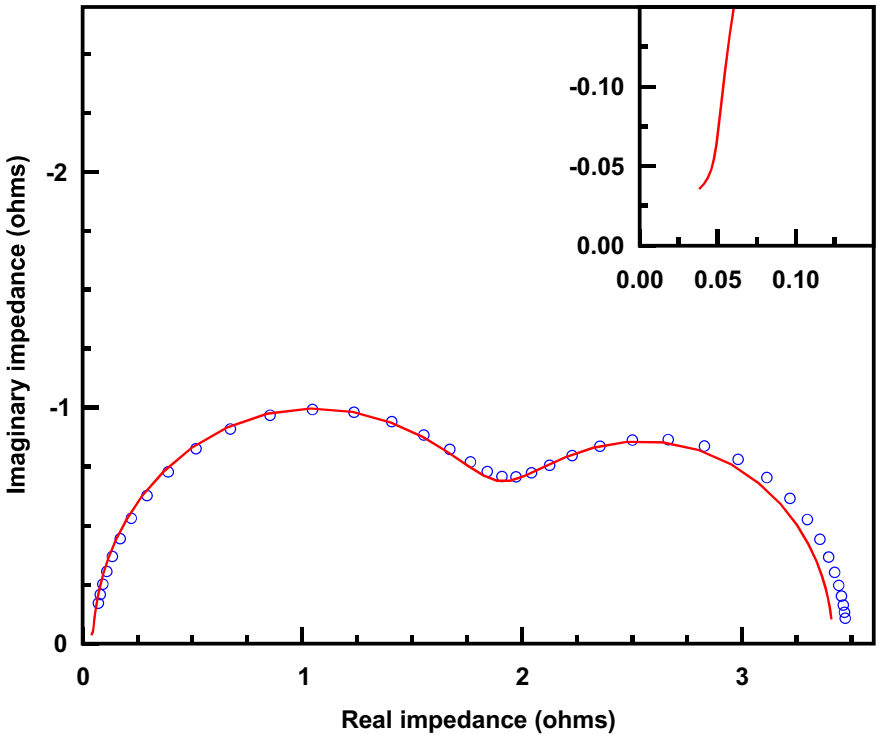

Figure 6-1: Simulated (circles) and fitted (solid line) photoelectrode impedance spectrum at 821mV bias voltage. Electrolyte diffusion is visible as an additional arc on the right. The numerical simulations failed to converge reliably at high frequencies and therefore this data is omitted (only data from the analytical model is shown in the inset).

6.2.1 Impedance Fitting

The seven new photoelectrode impedance spectra were fitted to equation 6.70 using Microsoft Excel. At high open circuit voltages diffusion of redox ions was clearly visible as an additional low frequency arc (figure 6-1). At lower voltages the electrolyte arc gradually blended into the photoelectrode arc until the electrolyte contribution could not be reliably distinguished (see figure 5-3). High frequency simulations were omitted as the numerical model did not reliably converge at these conditions. The result was that transport resistance could not be accurately fitted at high voltages as the characteristic line was not visible.

Both $R_{T,ox}$ and C_{ox} are defined to be constant in equations 6.35 and 6.37 but in the impedance fits their values varied more than two orders of magnitude. Their product, however, was approximately constant with the correct value. Therefore the equilibrium concentration could not be fitted from the impedance data (through C_{ox} assuming film thickness d is known), but tri-iodide diffusion coefficient value could be extracted via the product of $R_{T,ox}$ and C_{ox}.

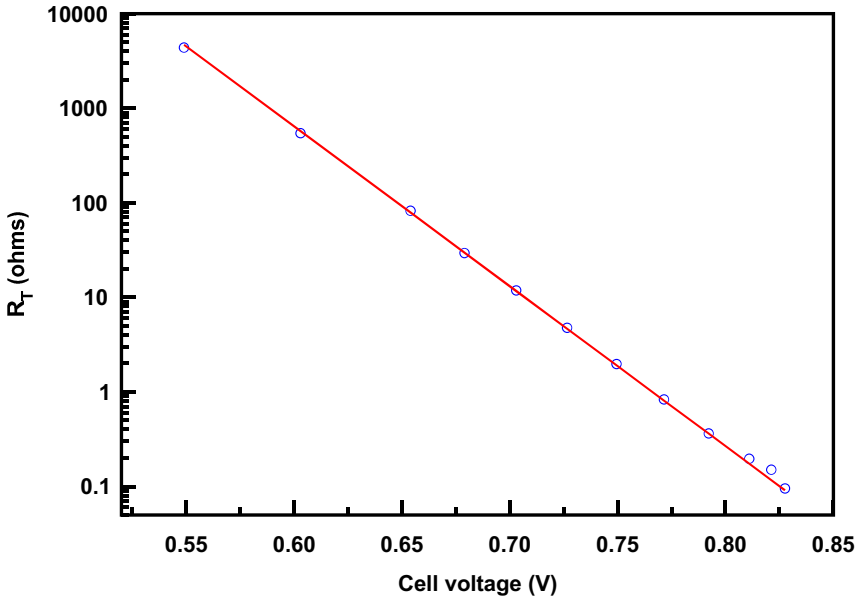

Figure 6-2: Simulated (circles) and fitted (solid line) photoelectrode transport resistance values.

6.2.2 Circuit Element Fits

Circuit element values obtained by fitting impedance values to equations 5.18 (figure 6-2) and 5.21 (figure 6-3). As it was not possible to get reliable fits for photoelectrode or tri-iodide recombination resistances, these resistances were combined with the substrate resistance to fit the resulting resistance elements using two versions of equation 6.70 in the limit of zero frequency. In the first version (figure 6-4), resistance was calculated without any diffusion effects (i.e. $R_{ox} = \infty$). The second version (also in figure 6-4) was the unaltered equation 6.70. Open circuit voltages were also fitted to the steady-state equation 6.16.

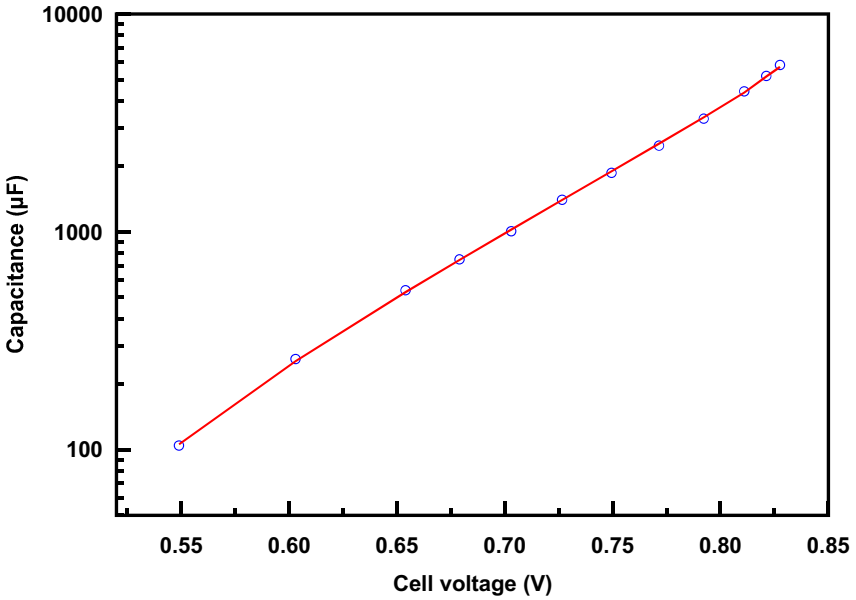

Figure 6-3: Simulated (circles) and fitted (solid line) photoelectrode capacitance values.

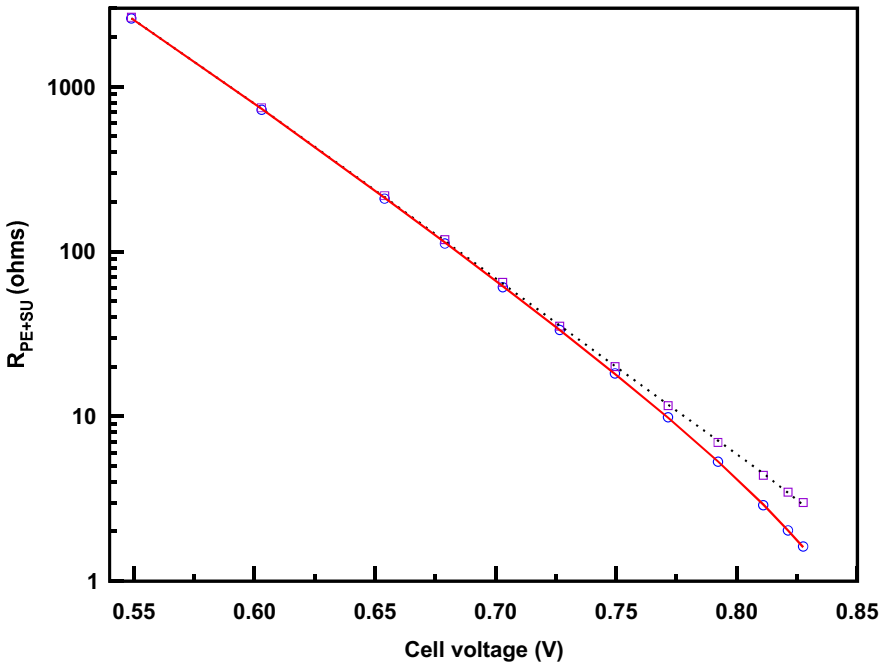

Figure 6-4: Simulated (circles and squares) and fitted (solid and dotted lines) photoelectrode differential resistance values with (squares and dotted line) and without (circles and solid line) electrolyte diffusion effects.

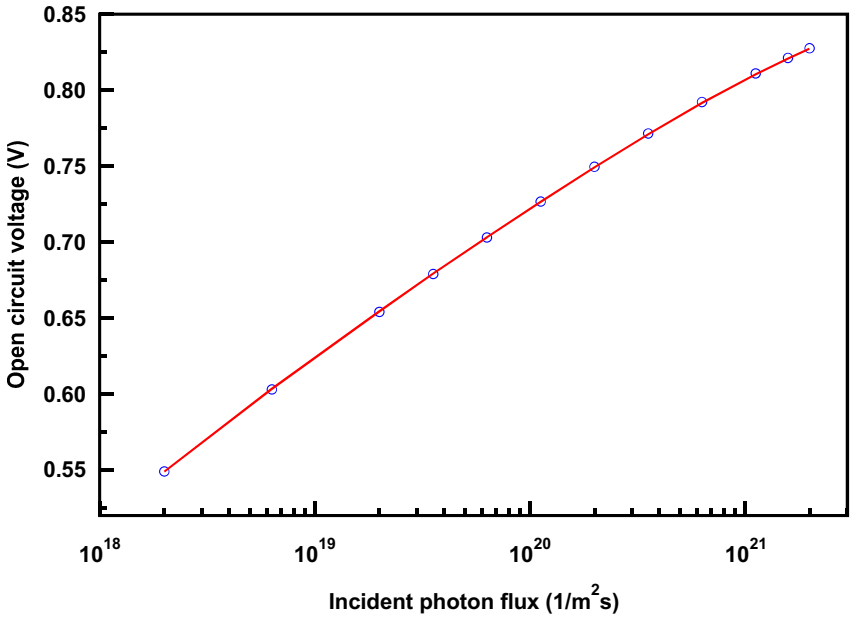

Figure 6-5: Simulated (circles) and fitted (solid line) dye solar cell open circuit voltages.

6.2.3 Parameter Values and Recreated J-V Curves

A comparison of actual and fitted model parameters is shown in table 6.1. As in the low light intensity case, the fitting procedure reproduces the original parameter values with reasonable accuracy indicating that it is a viable way to solve the inverse problem.

As was the case in the previous chapter, electron equilibrium concentration ($n_{c,eq}$) and light absorption coefficient ($\alpha_t d$) could not be fitted. Additionally photoelectrode porosity and the ratio of tri-iodide diffusion coefficients in the photoelectrode pores and free electrolyte layer were assumed to be known. Therefore all of these values were chosen to be the same as in the numerical simulations.

Figure 6-6 compares two J-V curves plotted using the fitted parameters values to ones using the original values. All J-V curves were calculated using the numerical model as the simplified analytical model does require some iteration to calculate the correct substrate recombination. As the fitted tri-iodide equilibrium concentration and diffusion coefficient are somewhat smaller than original values, the predicted fill factors and short circuit currents are lower than original ones at high light intensities. The same can also be seen when comparing original and predicted IPCE ratios (figure 6-7).

6.2.4 Recombination Pathways

The device model has three possible recombination reactions: substrate recombination, recombination to the electrolyte and recombination to the dye. Conceptually one can divide the electrolyte recombination into electron concentration (REC_e) and tri-iodide concentration (REC_{ox}) parts by calculating the difference in recombination with actual and equilibrium tri-iodide concentration.

$$REC = REC_e + REC_{ox} = k_r d n_{c,eq}^{\gamma} n_{DC}^{\gamma} + k_r d n_{c,eq}^{\gamma} n_{DC}^{\gamma} \cdot (c_{ox,DC} - 1) \tag{6.77}$$

Figure 6-8 shows the different recombination pathway currents as a function of applied cell voltage at roughly one sun light intensity. The predicted contribution to recombination due to tri-iodide diffusion is larger than the correct one but otherwise the inverse problem solution gives the correct magnitudes for the different recombination pathways. The simulated cell is mostly limited by electron transfer to the electrolyte with tri-iodide diffusion and substrate recombination playing significant roles. Insufficient regeneration of the dye is not a major source of recombination at maximum power point but is significant at open circuit.

6.3 Conclusions

In this chapter a method for solving the dye solar cell device model inverse problem has been introduced. The method was validated on simulated data and reproduced the original parameter values with good accuracy. Presently the method uses only open circuit data which makes it difficult to extract the correct parameter values affecting electrolyte conductivity.

Parameter description	Symbol	Actual value	Fitted value
Photoelectrode parameters			
Normalized electron diffusion coefficient	$D_c n_{c,eq}/d$	$1.80 \cdot 10^8$	$1.77 \cdot 10^8$
Normalized recombination rate coefficient	$k_r n_{c,eq}^{\gamma} d$	$1.29 \cdot 10^{11}$	$0.973 \cdot 10^{11}$
Recombination order	γ	0.7	0.708
Normalized electron equilibrium concentration	$n_{c,eq} d$	$3.0 \cdot 10^4$	0
Normalized trapped electrons at equilibrium	$n_{t,eq} d$	$1.50 \cdot 10^{15}$	$0.723 \cdot 10^{15}$
Trap distribution	β_T	0.3	0.324
Film porosity	P	0.5	0.5
Optical parameters			
Normalized total light absorption coefficient	$\alpha_t d$	-1	-1
Light harvesting and injection efficiency	$\eta_{LH}\eta_{INJ}$	0.700	0.689
Normalized dye recombination rate coefficient	$\frac{k_e n_{c,eq}}{k_{REG} c_{red,eq}}$	$4.00 \cdot 10^{-15}$	$3.86 \cdot 10^{-15}$
Electrolyte parameters			
Normalized tri-iodide diffusion coefficient	D_{ox}/d^2	3.00	2.81
Tri-iodide diffusion coefficient ratio	$D_{ox}/D_{ox,F}$	0.33	0.33
Normalized tri-iodide equilibrium concentration	$c_{ox,eq} d/S_{ox}$	$3.61 \cdot 10^{20}$	$2.82 \cdot 10^{20}$
Normalized free electrolyte layer thickness	$\frac{d_{el}}{d}$	3.00	3.00
Substrate parameters			
Exchange current density	$i_{0,s}$	$3.00 \cdot 10^{-6}$	$2.93 \cdot 10^{-6}$
Symmetry factor	β_{PE}	0.5	0.503
Counter electrode parameters			
Exchange current density	i_0	$2.00 \cdot 10^{-6}$	$2.01 \cdot 10^{-6}$
Symmetry factor	β_{PE}	0.5	0.5

Table 6.1: Actual and fitted parameter values for the simulated dye solar cell.

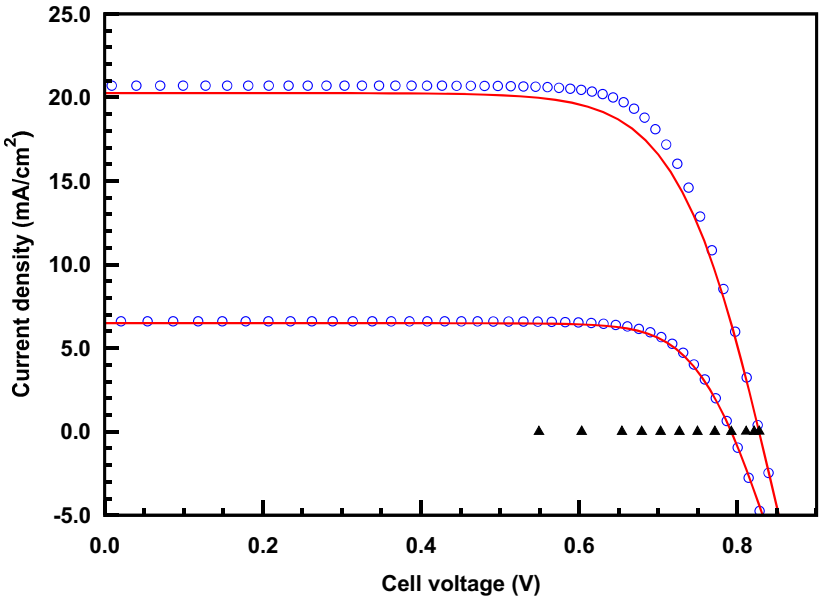

Figure 6-6: Simulated (circles) and predicted (solid line) dye solar cell J-V curves at photon fluxes of $2.0 \cdot 10^{21}$ and $6.3 \cdot 10^{20}$ $1/(\mathrm{m}^2\mathrm{s})$. Filled triangles indicate open circuit voltage points where impedance spectra were simulated. The fitted model predicts somewhat lower electrolyte conductivity which results in lower fill factors and short circuit currents at high light intensities.

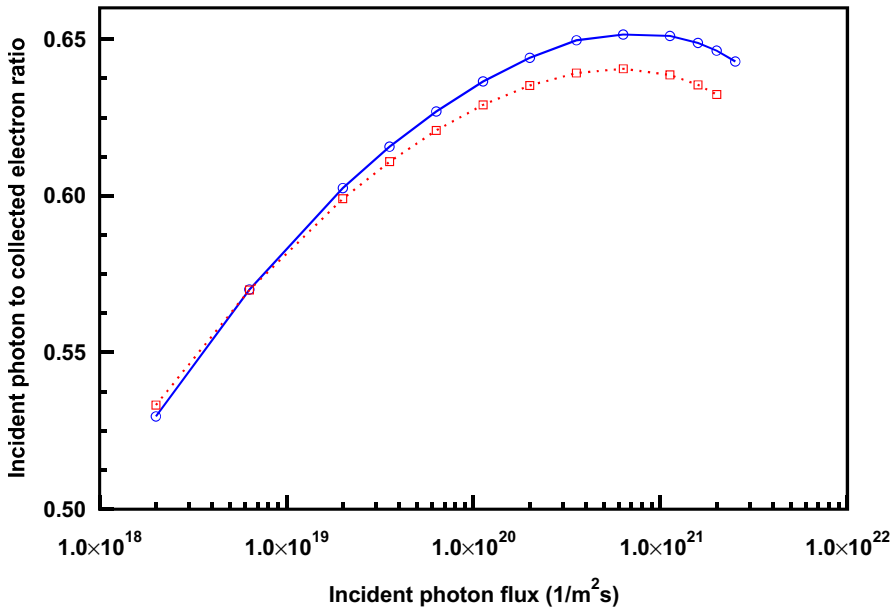

Figure 6-7: Simulated (circles and solid line) and predicted (squares and dotted line) dye solar cell IPCE ratios.

Improvements incorporating short circuit data would require numerical solutions but would undoubtedly improve model fits significantly.

A key feature of the inverse solution is that it enables the estimation of the relative importance of the different recombination pathways based on measurements that can be implemented on fully functional cells with standard electrochemical equipment. However, the modelling does require one to know the porosity and thickness of the photoelectrode film as well as the distance between the counter electrode and the photoelectrode. Porosity and photoelectrode thicknesses can be measured before sealing the cell whereas free electrolyte layer thickness can be inferred from the gasked thickness or possibly measured via absorption of light by tri-iodide. Additionally it was assumed that diffusion limited current could be used to measure the ratio of tri-iodide diffusion coefficients in the pores and in the free electrolyte layer. Given that this measurement requires very high applied voltages, it cannot taken for granted that the electrolyte remains stable throughout the scan. Therefore there is some doubt whether the presented data analysis can be carried out on an experimental cell with the high level of accuracy achieved here.

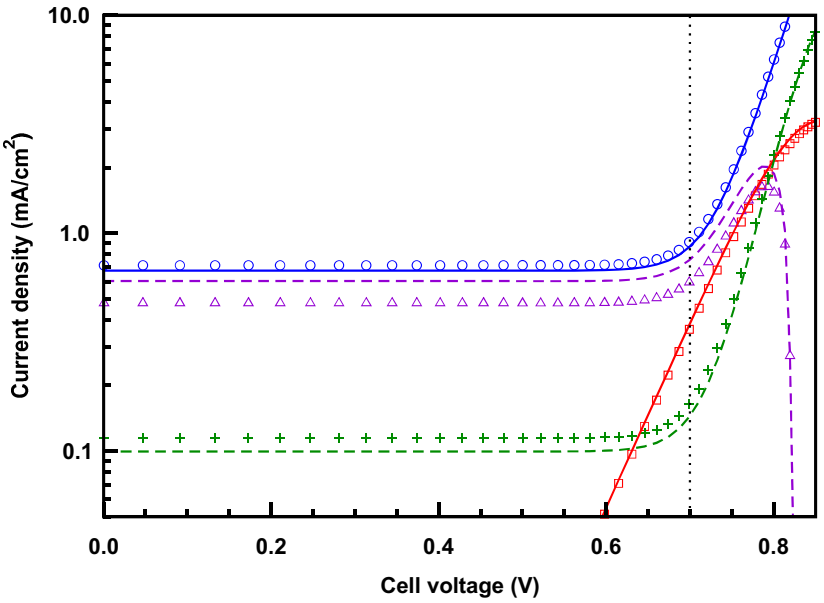

Figure 6-8: Simulated (markers) and predicted (solid and dashed lines) recombination currents. Circles indicate electrolyte recombination caused by electrons, triangles electrolyte recombination caused by the build-up of tri-iodide in the photoelectrode pores, squares substrate recombination and plus-signs recombination to oxidized dye molecules. Vertical dotted line indicates maximum power point. Photon flux is $1.59 \cdot 10^{21}$ $1/(\mathrm{m}^2\mathrm{s})$ which roughly corresponds to one sun light intensity. Simulated short circuit current was 16.5 mA/cm^2 compared to a photogeneration current of 17.8 mA/cm^2.

Chapter 7

Perovskite Solar Cell Device Model

At time of writing this thesis new thin film solar cells based on organometal halide perovskites have experienced an explosion of research interest over the past two years, enabled by a major breakthrough in 2012 by Kim et al [51] and Lee et al [52]. Since then perovskites have already surpassed the best dye cells in efficiency [35] while being easier to fabricate owing to their solid state structure. Based on this astounding progress, it appears likely that dye solar cell research will wither as scientists switch their attention to the more promising perovskite cells.

This chapter details the initial steps taken towards describing charge transport and recombination inside a perovskite solar cell. First the perovskite solar cell is briefly introduced and then basic material property information taken from literature is used to develop a continuum model describing a p-i-n heterojunction.

7.1 Organometal Halide Perovskite Solar Cell

A perovskite solar cell consists of four layers deposited on a transparent conductive surface — usually FTO or ITO (indium tin oxide) glass. These are, in order of deposition, n-type semiconductor, perovskite absorber, p-type semiconductor or other hole transporting material and a metal contact . The perovskite layer may also include nanoporous titanium dioxide or aluminium oxide [51, 52, 53].

In current state of the art the n-type semiconductor is the same as the blocking layer used in dye solar cells (i.e. a TiO_2 layer about 50 nm thick deposited by spray pyrolysis or spin coating [51, 52, 53]). To date the best absorber has been methylammonium lead tri-iodide ($CH_3NH_3PbI_3$) [51, 52, 53]. After spin coating a solution containing methylammonium iodide (CH_3NH_3I) and lead di-iodide (PbI_2) the two components form a perovskite structure, which is a face centered cubic structure with methylammonium in the center of the cube, lead in the corners and iodine in the center of the faces [51]. For the p-type material 2,2,7,7-tetrakis-(N,Ndi-

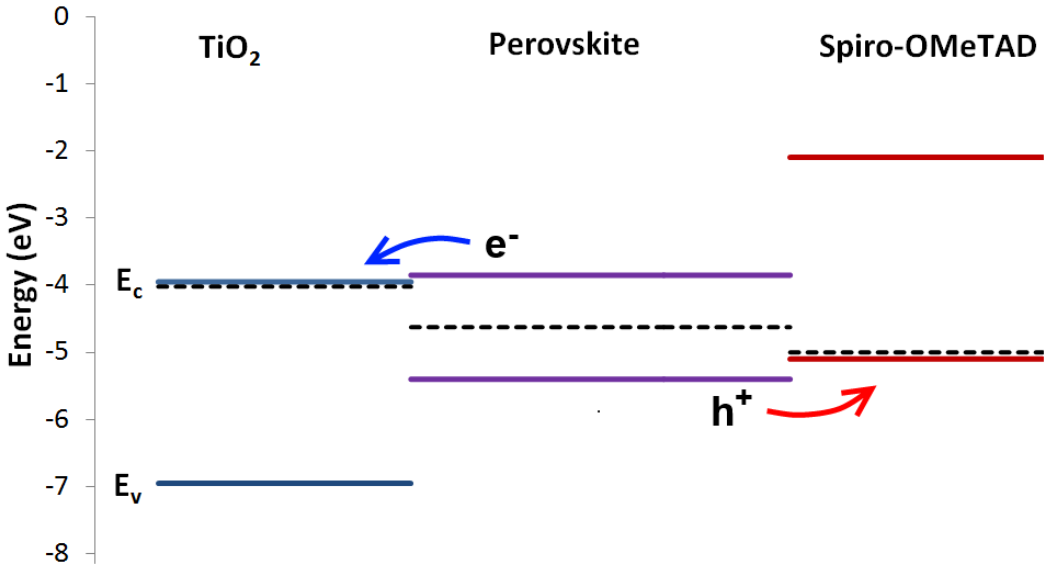

Figure 7-1: Approximate energy diagram of the key perovskite cell components. Light is absorbed in the perosvkite layer creating free holes (h^+) and electrons (e^-). The conduction band energy (E_c) of the TiO_2 is lower than that of the perovskite allowing electrons to move into it. The conduction band of spiro-OMeTAD, on the other hand, is much higher creating an effective energy barrier for electron transfer. Holes have an opposite electric charge to electrons and can therefore easily transfer into the valence band (E_v) of spiro-OMeTAD while seeing a large energy barrier opposing the transfer into TiO_2.

p-methoxyphenylamine)9,9-spirobifluorene (spiro-OMeTAD) conductive polymer is spin coated from solution [51]. Conductivity is enhanced by adding some suitable salt into the solution, which causes p-type doping [54].

Visible light is absorbed in the perovskite lifting some valence band electrons into the conduction band. The electrons, as well as the produced holes in the valence band, are free to move in the perovskite but due to the energy band structures of the materials only electrons can move to the n-type layer and only holes can move to the p-type layer [51] (see figure 7-1).

7.2 P-I-N Heterojunction Model for Perovskite Solar Cell

In this section a continuum model based on partial differential equations describing electron and hole number densities is developed. As in the case of the dye-sensitized solar cell, a 1-D structure is considered by assuming that the cell is homogeneous in the other dimensions.

First one must decide whether electron-hole pairs created by absorbed photons dissociate very quickly due to thermal fluctuations or whether one should model the diffusion of excitons. This is a well-known problem that is addressed in any textbook dealing with semiconductor physics. The approach taken is that the electron can be thought to orbit the hole the same

way an electron orbits a proton in a hydrogen atom. Therefore the hydrogen atom solution of the Schrödinger equation is valid here as long as one uses the perovskite permittivity instead of vacuum one and effective masses for the particles. The binding energy given by the solution is [23]

$$E_b = -\frac{m_R q^4}{8\epsilon_r^2 \epsilon_0^2 h^2}, \tag{7.1}$$

where m_R is the reduced mass of the problem (taking effective electron and hole masses as inputs), q is electron charge, ϵ_r is the relative permittivity of the perovskite and h is the Planck constant.

Frost et al. [55] used density functional theory to calculate theoretical values for the effective charge carrier masses and for the relative permittivity. Using their results of 0.15 times electron rest mass for electrons and 0.12 times for holes as well as 25.7 for the relative permittivity [56], one finds that the binding energy is about 1 meV. Compared to the characteristic thermal energy of about 26 meV at room temperature (298.15 K), the conclusion is that excitons break up very quickly due to thermal excitations. Hence only free electrons and holes should be modelled.

7.2.1 N-type Layer

As shown in figure 7-1 the valence band of TiO_2 is thought to lie much lower than the valence band of the perovskite absorber and hence no significant flow of holes into the TiO_2 valence band occurs. Subsequently modelling will consider only electric potential and transport of electrons as recombination would require a source for holes.

Electric potential is governed by Gauss' law:

$$\frac{\partial^2 \varphi}{\partial x^2} = -\frac{q}{\epsilon_{r,n}\epsilon_0} \cdot (n_{eq,n} - n), \tag{7.2}$$

where φ is electric potential, x is distance from the FTO contact, q is elementary charge, ϵ_r is the relative permittivity of the n-type layer, ϵ_0 is vacuum permittivity and n is electron number density. Titanium dioxide deposited by spray pyrolysis is thought to be moderately n-doped [12] so the concentration of positively charged donor ions $n_{eq,n}$ must also be taken into account.

Electron transport occurs both by drift and diffusion.

$$j_e = -D_{ntype} \cdot \frac{\partial n}{\partial x} + n \cdot \mu_{ntype} \cdot \frac{\partial \varphi}{\partial x}, \tag{7.3}$$

where j_e is electron flux, D_{ntype} is electron diffusion coefficient and μ_{ntype} is electron mobility.

Inserting this into the continuity equation 2.25 yields

$$\frac{\partial n}{\partial t} = D_{ntype} \cdot \frac{\partial^2 n}{\partial x^2} - \mu_{ntype} \cdot \left(\frac{\partial n}{\partial x} \cdot \frac{\partial \varphi}{\partial x} + n \cdot \frac{\partial^2 \varphi}{\partial x^2} \right) \tag{7.4}$$

7.2.2 Perovskite Layer

In addition to charge transport, light absorption leads to the creation of free electrons and holes and recombination destroys them.

Charge generation is modelled using the same formalism as in the dye cell model. The only difference is that there are no separate injection and dye regeneration events so all created excited states are assumed to result in free electrons and holes.

$$G = \eta_{CG}\phi \cdot \frac{\alpha_t}{e^{\alpha_t d} - 1} \cdot e^{\alpha_t x} \tag{7.5}$$

Presently next to nothing is known about recombination in perovskite cells. Therefore the approach taken here is to use conventional Shockley-Read-Hall formalism from established semiconductor theory [26]. In this picture there are multiple localized (trap) states in the band gap which act to catalyse recombination. Generally states that are near the middle of the gap are the most efficient recombination centers so a model with a single trap state at the center of the gap is used.

Electrons fall into the trap with a net rate of

$$R_n = \frac{n \cdot (1 - f) - N_C e^{\frac{E_T - E_C}{k_B T}} \cdot f}{\tau_n}, \tag{7.6}$$

where f is the probability the trap is occupied by an electron, N_C is the conduction band density of states, E_T is the energy level of the trap, E_C is the conduction band energy level and τ_n is the pseudo-lifetime of conduction band electrons.

Holes get trapped with the rate

$$R_p = \frac{p \cdot f - N_V e^{\frac{E_V - E_T}{k_B T}} \cdot (1 - f)}{\tau_p}, \tag{7.7}$$

where p is the hole number density, N_V the valence band density of states and τ_p the pseudo-lifetime of valence band holes.

Combining the two recombination equations by knowing that at steady-state both reactions must proceed at the same rate yields the occupation probability of the trap, which can then be inserted into either recombination rate equation to obtain the final equation for recombination

$$R = \frac{np - n_{eq}p_{eq}}{\tau_n \cdot \left(n + N_C e^{\frac{E_T - E_C}{k_B T}}\right) + \tau_p \cdot \left(p + N_V e^{\frac{E_V - E_T}{k_B T}}\right)}. \tag{7.8}$$

Inserting the recombination and generation terms along with and diffusion transport terms into respective electron and hole continuity equations results in

$$\frac{\partial n}{\partial t} = D_n \cdot \frac{\partial^2 n}{\partial x^2} - \mu_n \cdot \left(\frac{\partial n}{\partial x} \cdot \frac{\partial \varphi}{\partial x} + n \cdot \frac{\partial^2 \varphi}{\partial x^2}\right) + G - R \tag{7.9}$$

for electrons and

$$\frac{\partial p}{\partial t} = D_p \cdot \frac{\partial^2 p}{\partial x^2} + \mu_p \cdot \left(\frac{\partial p}{\partial x} \cdot \frac{\partial \varphi}{\partial x} + p \cdot \frac{\partial^2 \varphi}{\partial x^2} \right) + G - R \tag{7.10}$$

for holes.

Electric potential is again given by Gauss' Law

$$\frac{\partial^2 \varphi}{\partial x^2} = -\frac{q}{\epsilon_r \epsilon_0} \cdot (p - n + n_{eq} - p_{eq}), \tag{7.11}$$

where n_{eq} and p_{eq} refer to electron and hole concentrations at equilibrium and without any band bending effects. For a fully intrinsic semiconductor these cancel out because only free charges exist (trapped charge is neglected in the model), whereas in doped semiconductors the equilibrium values represent ionized dopant atoms.

7.2.3 P-type Layer

Due to the energy differences of the conduction bands (see fig. 7-1), no electrons are expected to be injected into the p-type layer. Thus only the transport of holes is considered. Generation is zero because the band gap is too high. As there is no process that creates electrons in excess of thermal generation, recombination is also zero.

$$\frac{\partial p}{\partial t} = D_{ptype} \cdot \frac{\partial^2 p}{\partial x^2} + \mu_{ptype} \cdot \left(\frac{\partial p}{\partial x} \cdot \frac{\partial \varphi}{\partial x} + p \cdot \frac{\partial^2 \varphi}{\partial x^2} \right) \tag{7.12}$$

$$\frac{\partial^2 \varphi}{\partial x^2} = -\frac{q}{\epsilon_{r,p} \epsilon_0} \cdot (p - p_{eq,p}) \tag{7.13}$$

7.2.4 Metal Contact to N-type Layer

As stated before, fluorine-doped tin oxide is used as the metal contact for the n-type side. In principle this configuration could lead to a rectifying Schottky contact but experience with the same interface in dye cells indicates that there is no significant voltage loss. This is taken into account in the model by assuming that there is no band bending at the interface and that electron concentration is the same as equilibrium concentration in bulk material. These assumptions lead to a perfect ohmic contact with zero voltage loss across the interface.

$$n = n_{eq,n} \tag{7.14}$$

7.2.5 Boundary Between N-type Layer and Perovskite

Gauss' Law requires that electric displacement field is continuous across material boundaries [57]. Remembering that electric displacement field is electric field multiplied by material permittivity and adding the requirement that electric potential must be continuous, one has all the boundary conditions for electric potential.

$$\epsilon_0 \epsilon_{r,n} \cdot \frac{\partial \varphi}{\partial x}|_{ntype} = \epsilon_0 \epsilon_r \cdot \frac{\partial \varphi}{\partial x}|_{perovskite} \tag{7.15}$$

$$\varphi_{ntype} = \varphi_{perovskite} \tag{7.16}$$

For electrons, it is assumed that charge transfer across the boundary is infinitely fast resulting in a continuous quasi-Fermi level. This should be a reasonable approximation for electron flow from the perovskite as it is energetically downhill, but may not be valid for the opposite direction of flow. Therefore this report is restricted to modelling only positive photocurrents and the continuous quasi-Fermi level assumption should be re-examined for any reverse current flow calculation.

The difference of the quasi-Fermi level from its equilibrium value is given by

$$E_F - E_{F,eq} = k_B T \cdot \ln\left(\frac{n}{n_{eq}}\right) \tag{7.17}$$

where E_F is the quasi-Fermi level, $E_{F,eq}$ is the quasi-Fermi level at equilibrium, n is electron concentration and n_{eq} is electron concentration at equilibrium. Setting the quasi-Fermi levels equal at the interface results in

$$\frac{n_{ntype}}{n_{eq,ntype}} \cdot e^{\frac{E_{F,eq,ntype}}{k_B T}} = \frac{n}{n_{eq}} \cdot e^{\frac{E_{F,eq}}{k_B T}} \tag{7.18}$$

The flow of electrons is discontinuous by the amount of surface recombination flux.

$$j_{e,ntype} = D_{ntype} \cdot \frac{\partial n_{ntype}}{\partial x} - \mu_{ntype} \cdot n_{ntype} \cdot \frac{\partial \varphi_{ntype}}{\partial x} = \frac{I_{cell}}{q A_{cell}} \tag{7.19}$$

$$j_{e,perovskite} = D_n \cdot \frac{\partial n}{\partial x} - \mu_n \cdot n \cdot \frac{\partial \varphi}{\partial x} = \frac{I_{cell} + I_{surf,n}}{q A_{cell}} \tag{7.20}$$

where j_e is the electron flux, I_{cell} is cell current, $I_{surf,n}$ is the surface recombination current, q is elementary charge and A_{cell} is cell area.

Hole flux is given by the surface recombination.

$$j_{h,perovskite} = D_p \cdot \frac{\partial p}{\partial x} + \mu_p \cdot p \cdot \frac{\partial \varphi}{\partial x} = \frac{I_{surf,n}}{q A_{cell}} \tag{7.21}$$

where $j_{h,perovskite}$ is the hole flux.

In this report surface recombination at the n-type interface is considered to be negligible as Burschka et al. were able to fabricate a highly efficient cell with a high surface area contact between mesoporous TiO_2 and perovskite [58]. Therefore the surface recombination term is merely for the purpose of compatibility with possible future modifications.

7.2.6 Boundary Between Perovskite and P-type Layer

The boundary conditions at the P-type interface are similar to the N-type interface. Aside from different material properties, surface recombination at this interface is considered to be significant to device performance [59].

The boundary conditions for electric potential are

$$\epsilon_0 \epsilon_{r,p} \cdot \frac{\partial \varphi}{\partial x}|_{ptype} = \epsilon_0 \epsilon_r \cdot \frac{\partial \varphi}{\partial x}|_{perovskite} \tag{7.22}$$

$$\varphi_{ptype} = \varphi_{perovskite} \tag{7.23}$$

for electrons

$$j_{n,perovskite} = D_n \cdot \frac{\partial n}{\partial x} - \mu_n \cdot n \cdot \frac{\partial \varphi}{\partial x} = -\frac{I_{surf,p}}{qA_{cell}} \tag{7.24}$$

and for holes

$$\frac{p_{ptype}}{p_{eq,ptype}} \cdot e^{-\frac{E_{F,eq,ptype}}{k_B T}} = \frac{p}{p_{eq}} \cdot e^{-\frac{E_{F,eq}}{k_B T}}, \tag{7.25}$$

$$j_{p,ptype} = D_{ptype} \cdot \frac{\partial p_{ptype}}{\partial x} + \mu_{ptype} \cdot p_{ptype} \cdot \frac{\partial \varphi_{ptype}}{\partial x} = -\frac{I_{cell}}{qA_{cell}}, \tag{7.26}$$

$$j_{p,perovskite} = D_p \cdot \frac{\partial p}{\partial x} + \mu_p \cdot p \cdot \frac{\partial \varphi}{\partial x} = -\frac{I_{cell} + I_{surf,p}}{qA_{cell}} \tag{7.27}$$

For the sake of simplicity and to facilitate numerical solutions (finding the correct solution was easier when surface recombination did not radically change with electron concentration) surface recombination is taken to follow a power law dependency to both free electron concentration in the perovskite and free hole concentration in the P-type layer. Physically this can be a reasonable approximation to trap mediated recombination where trapped electrons and holes recombine with free holes and electrons, although in this report it is used simply due to its convenient mathematical form. Expressing the number of trapped electrons as a function of free electrons is described in section 4.2.3.

$$\frac{I_{surf,p}}{qA_{cell}} = k_p \cdot n^{0.5} \cdot p_{ptype}^{0.5} \tag{7.28}$$

where k_p is the surface recombination rate coefficient, n the electron concentration at the perovskite surface and p_{ptype} hole concentration at the spiro surface. Note that this formulation gives some recombination even at equilibrium in the dark. However, the correction term would include the dark concentration, which requires solving the model numerically. Moreover, the correction term is also very small as dark concentrations are negligible compared to reasonable operating conditions.

Layer	**Conduction band (E_C)** eV	**Valence band (E_V)** eV	**Fermi level ($E_{F,eq}$)** eV
N-type	-3.9	-7.2	-3.95
Perovskite	-3.75	-5.4	-4.575
P-type	-1.5	-5.05	-5.0

Table 7.1: Material energy level values used in perovskite solar cell modelling. Perovskite ($CH_3NH_3PbI_3$) values as well as spiro-OMeTAD HOMO (valence band) and LUMO (conduction band) values are taken from a report by Schulz et al. [60].

7.2.7 Metal Contact to P-type Layer

As with the N-type side contact, the P-type contact is also assumed to be perfect with no voltage loss or band bendings. Abate et al. observed negligible contact resistance between doped spiro-OMeTAD and gold contact [54] giving experimental support to this model.

Perfect contact means that hole concentration at the contact is unchanged from equilibrium condition in the bulk.

$$p = p_{eq,p} \tag{7.29}$$

Electric potential is set to zero.

$$\varphi = 0 \tag{7.30}$$

7.2.8 Parameter Values

The energy levels of the materials are given in table 7.1. Base values are taken from a report by Schulz et al. [60] Unfortunately their values for the compact TiO_2 given appear to contradict the picture of easy electron transfer from the perovskite so the conduction band energy level was set to -3.9 eV versus vacuum instead of -3.6 eV as this ensures that the TiO_2 conduction band lower than the perovskite conduction band. The valence band and Fermi levels were shifted accordingly. Other changes include reducing the band gap to 1.65 eV based on IPCE saturation around 750 nm from a report by Lee et al. [52], assuming the perovskite Fermi level to lie exactly in the middle of the band gap and shifting the spiro highest occupied molecular orbital (HOMO) 50 meV lower to -5.05 eV. Schulz and coworkers used undoped spiro-OMeTAD in their measurements. Therefore the Fermi level of doped spiro was simply assumed to be 50 meV higher than the HOMO level. The changes were made because they were found to facilitate the numerical solving of the model and improve the agreement between experimental and simulated I-V curves.

Parameter values for the base case transport model are given in table 7.2. Although references can be found for some parameters, many values have been simply been set so that they result in reasonably realistic I-V curves. Typical film thickness values for the N-type, perovskite and P-type layer are 50, 500 and 500 nm, respectively [52, 53]. However, difficulties

in numerical solutions necessitated a reduction in perovskite and P-type film thicknesses to 300 and 100 nm.

For the selective contacts, equilibrium carrier concentrations are based simply on estimated doping densities. For the perovskite effective charge carrier masses from numercal simulations are used to estimate conduction and valence band densities of state and equilibrium concentrations from the assumption that Fermi level is exactly in the middle of the band gap.

$$N = 2 \cdot \left(\frac{2\pi m_{eff} k_B T}{h^2} \right)^{\frac{3}{2}} \tag{7.31}$$

where N is the density of states, m_{eff} is the effective mass (0.15 times electron rest mass for electrons and 0.12 times for holes [55]), h is the Planck constant, k_B is the Boltzmann constant and T is temperature.

$$n_{eq} = N_C \cdot e^{\frac{E_{F,eq} - E_C}{k_B T}} \tag{7.32}$$

$$p_{eq} = N_V \cdot e^{\frac{E_V - E_{F,eq}}{k_B T}} \tag{7.33}$$

where N_C is the conduction band density of states, N_V valence band density of states, E_C conduction band energy, E_V valence band energy and $E_{F,eq}$ is the Fermi level at equilibrium.

In addition to the base case model of table 7.2, an alternate scheme was simulated. Here recombination was set to occur mostly on the perovskite–spiro interface instead of in the bulk perovskite. The parameter values were otherwise the same as the base case except for the surface recombination coefficient (5 m/s instead of 0 m/s) and electron and hole pseudo-lifetimes (both 1.25 ns instead of 6.67 ps). The base case pseudo-lifetimes values were chosen so that calculated open circuit voltages were at the lower end of those reported in the literature [52, 53, 58, 59].

The photon flux used in the simulations corresponds roughly to one sun illumination.

Parameter description	Symbol	Unit	Value	Reference
Perovskite parameters				
Electron mobility	μ_n	$m^2/(Vs)$	$6.6 \cdot 10^{-3}$	[61]
Hole mobility	μ_p	$m^2/(Vs)$	$6.6 \cdot 10^{-3}$	[61]
Electron equilibrium concentration	n_{eq}	$1/m^3$	$1.61 \cdot 10^{10}$	see text
Hole equilibrium concentration	p_{eq}	$1/m^3$	$1.15 \cdot 10^{10}$	see text
Relative permittivity	ϵ_r	–	25.7	[56]
Electron pseudo-lifetime	τ_n	s	$6.67 \cdot 10^{-12}$	see text
Hole pseudo-lifetime	τ_p	s	$6.67 \cdot 10^{-12}$	see text
Trap energy level	E_T	eV	-4.575	assumption
Surface recombination coefficient	k_p	m/s	0	assumption
Layer thickness	d	m	$300 \cdot 10^{-9}$	assumption
N-type parameters				
Electron mobility	μ_n	$m^2/(Vs)$	$5 \cdot 10^{-7}$	[49]
Electron equilibrium concentration	n_{eq}	$1/m^3$	$1.7 \cdot 10^{24}$	[62]
Relative permittivity	$\epsilon_{r,n}$	–	40	[62]
Layer thickness	d_n	m	$50 \cdot 10^{-9}$	assumption
P-type parameters				
Hole mobility	μ_p	$m^2/(Vs)$	$3.6 \cdot 10^{-8}$	[54]
Hole equilibrium concentration	p_{eq}	$1/m^3$	$5.0 \cdot 10^{22}$	[54]
Relative permittivity	$\epsilon_{r,p}$	–	3	[54]
Layer thickness	d_p	m	$100 \cdot 10^{-9}$	assumption
Optical parameters				
Charge generation efficiency	η_{CG}	–	1.0	assumption
Total absorption coefficient	α_t	$1/m$	$-1 \cdot 10^4$	assumption
Incident photon flux	ϕ	$1/(m^2s)$	$1 \cdot 10^{21}$	n/a
Cell parameters				
Cell area	A_{cell}	m^2	$1 \cdot 10^{-4}$	n/a
Cell temperature	T	K	298	n/a

Table 7.2: Base parameter values used in perovskite solar cell modelling.

7.3 Results

7.3.1 Band Diagrams

Simulated (see appendix D for a brief description of the model solver) band diagrams for zero bias in the dark, near short circuit and at open circuit are shown in figures 7-2, 7-3 and 7-4, respectively.

Due to the intrinsic semiconductor nature of the perovskite, there is very little electric charge in the film and the gradient of electric potential (electric field) is effectively constant.

Electric potential change is divided between perovskite and spiro layers. This is unfortunate as this potential change causes band bending in the spiro layer, which then leads to increased series resistance through hole depletion near the perovskite interface. Although this effect diminishes as cell voltage is increased, it would be preferable to have the entire potential change in the perovskite where the electric field drives charge separation. Both band bending and voltage loss in the TiO_2 layer are negligible due to the relatively high doping density.

The Fermi levels of the selective contacts play a key role in determining the quasi-Fermi levels in perovskite. As the Fermi level of TiO_2 is taken to be closer to the band edge than the Fermi level of spiro-OMeTAD, electron concentration is typically higher than hole concentration in the perovskite absorber. This is particularly true near open circuit conditions.

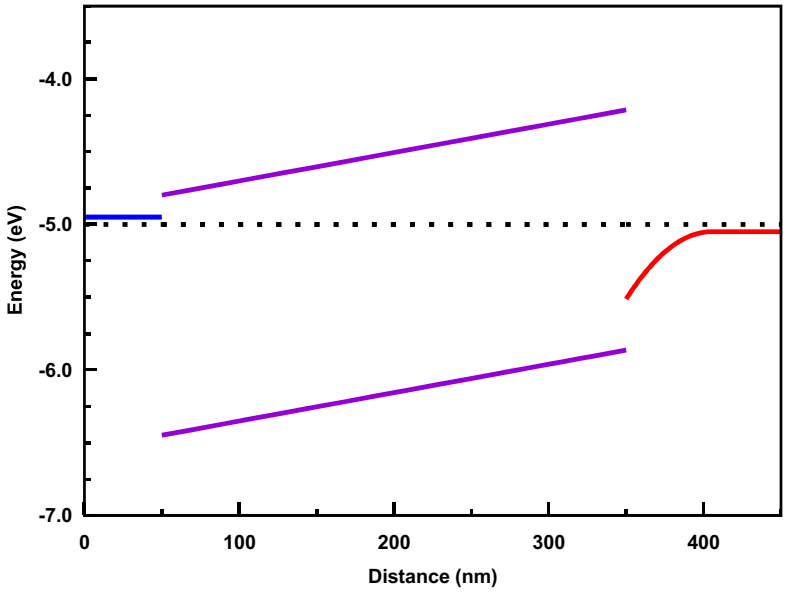

Figure 7-2: Band diagram of a perovskite cell at zero bias in the dark. Layers from left to right: TiO_2, perovskite, spiro-OMeTAD. Solid lines indicate conduction and valence bands, dotted line Fermi level (TiO_2 valence and spiro conduction band not drawn). Equilibration of Fermi levels causes band bending which is divided between spiro-OMeTAD and perovskite layers. Perovskite layer has very little net electric charge at point in the film meaning that the gradient of electric potential (electric field) is effectively constant. Band bending in spiro leads to hole depletion near the perovskite interface which will cause increased series resistance.

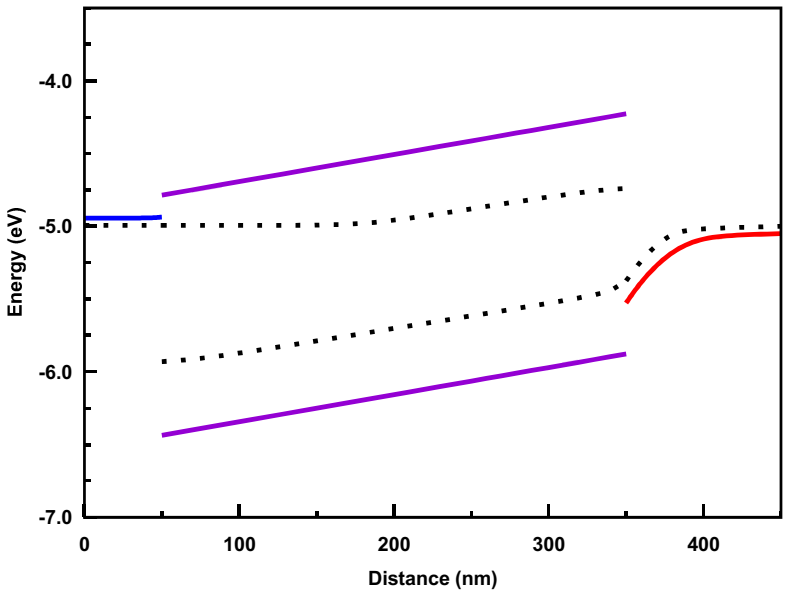

Figure 7-3: Band diagram of a perovskite cell near short circuit at 6 mV bias. Layers from left to right: TiO_2, perovskite, spiro-OMeTAD. Solid lines indicate conduction and valence bands, dotted line Fermi level (TiO_2 valence and spiro conduction band not drawn). Electric field drives charge separation in the perovskite causing a build-up of charge carriers near selective contacts. Hole depletion in spiro causes significant voltage loss.

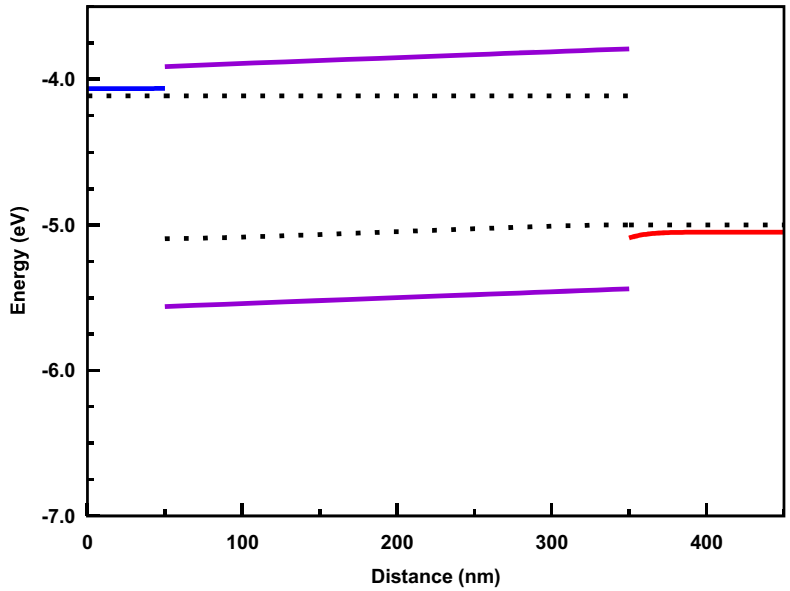

Figure 7-4: Band diagram of a perovskite cell at open circuit (886 mV). Layers from left to right: TiO_2, perovskite, spiro-OMeTAD. Solid lines indicate conduction and valence bands, dotted line Fermi level (TiO_2 valence and spiro conduction band not drawn). Fermi levels of selective contacts set the Fermi levels in perovskite resulting in higher electron than hole concentration.

7.3.2 J-V Curves

Figure 7-5 shows simulated J-V curves of the two different recombination schemes as well as an experimental cell illuminated with a red LED. Note that neither short circuit currents nor open circuits voltages of the experimental and simulated cells should be compared as the purpose of the calculations was not to predict either of these values. Instead the shapes of the curves could potentially yield useful information.

Band bending induced voltage loss in spiro is a significant factor in the low short circuit current and fill factor of the base case cell but limited perovskite conductivity is more important in limiting device efficiency.

In the alternate case with surface recombination perovskite conductivity plays a much smaller role while spiro series resistance is still significant. Both short circuit current and fill factors are much higher than in the base case because decreasing cell voltage results in higher electric potential at the perovskite–spiro interface leading to a steep decrease in electron concentration (a change of more than three orders of magnitude going from open circuit to short circuit). A decrease in hole concentration in spiro also reduces surface recombination but this concentration change is less than a factor of ten between open and short circuit.

The light intensity dependence of open circuit voltage in the simulated cells could be fitted to nonideality factors of around two: 2.2 for the base recombination case and 2.0 for the alternate one. Experimental results from ten different cells fabricated by Optoelectronic Device Group at University of Oxford yielded two different response groups: the first cells had nonideality factors ranging from 2.4 to 2.9 while in the other group the range was from 5.4 to 5.7. The simulations therefore appear to be broadly compatible with the first group of cells but not the other. Differences in experimental cell fabrication were not disclosed to the author so speculation on reasons for the differences is not possible. Light intensity dependency of short circuit current was also measured for two cells but no clear trend could be seen.

Based on a comparison of the shapes of the simulated J-V curves to the experimental one, it would appear that the alternate surface recombination scheme is a better description of the cell, although it is plausible that relatively minor changes in recombination equations or parameter values could change this view. Indeed a significant improvement could be seen in the base case fill factor when the voltage loss caused by P-type layer series resistance was removed (data not shown).

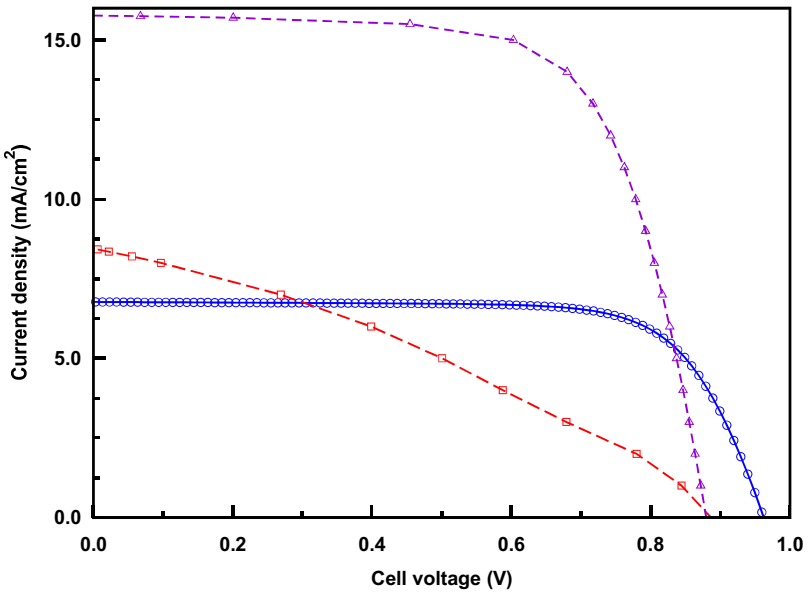

Figure 7-5: Measured and simulated J-V curves of perovskite solar cells. Measured cell (circles and solid line) was illuminated using a red LED with unknown photon flux. Simulated cells were illuminated with $1{\cdot}10^{21}$ $m^{-2}s^{-1}$ photon flux corresponding to a maximum short circuit current of about 16.02 mA/cm^2. J-V curve shapes appear to support the alternate recombination scheme (triangles and dashed line) over the base case (squares and dotted line). Experimental data provided by Adam Pockett from University of Bath Department of Chemistry using a cell fabricated by the Photovoltaic and Optoelectronic Device Group at University of Oxford Department of Physics.

7.3.3 Effect of Perovskite Fermi Level

Doping could theoretically be used to shift the equilibrium Fermi level of the perovskite potentially changing device performance. Usually doping is thought to increase the charge carrier concentration and hence improving material conductivity but a careful look at the model equations (continuity equations 7.9 and 7.10) will show that as long as the perovskite absorber can be thought of as intrinsic or near-intrinsic (i.e. the right hand side of equation 7.11 is approximately zero) the selective contacts will primarily determine charge carrier concentrations (via boundary conditions 7.18 and 7.25. Instead, doping affects mainly the electric potential in the perovskite. This means that doping must be strong enough to cause a significant change in electric potential — simply altering equilibrium charge carrier concentrations even by several orders of magnitude will have negligible effect.

Four different initial Fermi levels were simulated for the base recombination case and three for the alternate case. Fermi levels and corresponding equilibrium carrier concentrations (equations 7.32 and 7.33) are given in table 7.3.

Figures 7-6 and 7-7 show the calculated J-V curves for different doping regimes. The most important effect in both the base and alternate recombination schemes is the improvement of the fill factor caused by the reduction of spiro series resistance: The electric displacement field is continuous across the spiro–perovskite interface and thus the gradient of the electric potential at the perovskite side will affect band bending in spiro. The lower the gradient at a given electric potential change in perovskite, the less band bending there is in spiro. P-type doping causes the gradient to be lower and will therefore shift electric potential change to occur inside the absorber (see figure 7-8).

Decreased band bending in spiro elevates hole concentrations in the perovskite, which results in lower open circuit voltages in the bulk recombination case and slightly lower fill factors in the alternate (surface) one although the latter effect so small that it is overwhelmed by the improved spiro conduction mentioned above. In order to carry significant current in the spiro depletion layer, the hole concentration must remain reasonably high. Therefore the Fermi level in the hole depletion layer tends to follow the valence band bending at all but the lowest currents (see figure 7-3) . When current becomes low enough the Fermi level decouples from the valence band (figures 7-4 and 7-2) causing a shift in the J-V curve trend (the point where the J-V curves intersect in figure 7-6).

Enhanced average built-in field resulting from P-type doping is also more effective in driving free charges towards the selective contacts which yields higher short circuit currents in the bulk recombination case.

In summary it can be stated that the beneficial effect of light P-type doping is overwhelmingly a consequence of reduced band bending in spiro resulting from the continuity of electric displacement field. Therefore eliminating this band bending by altering the spiro layer would render doping ineffective.

Fermi level	**Electron concentration**	**Hole concentration**
eV	$1/m^3$	$1/m^3$
Base case		
-3.935	$1.073 \cdot 10^{21}$	$1.729 \cdot 10^{-1}$
-4.575	$1.610 \cdot 10^{10}$	$1.152 \cdot 10^{10}$
-5.220	$1.989 \cdot 10^{-1}$	$9.329 \cdot 10^{20}$
-5.240	$9.130 \cdot 10^{-2}$	$2.033 \cdot 10^{21}$
Alternate case		
-3.905	$3.451 \cdot 10^{21}$	$5.377 \cdot 10^{-2}$
-4.575	$1.610 \cdot 10^{10}$	$1.152 \cdot 10^{10}$
-5.260	$4.190 \cdot 10^{-2}$	$4.429 \cdot 10^{21}$

Table 7.3: Fermi levels and corresponding charge carrier concentrations used in modelling the effect of equilibrium Fermi level in the perovskite.

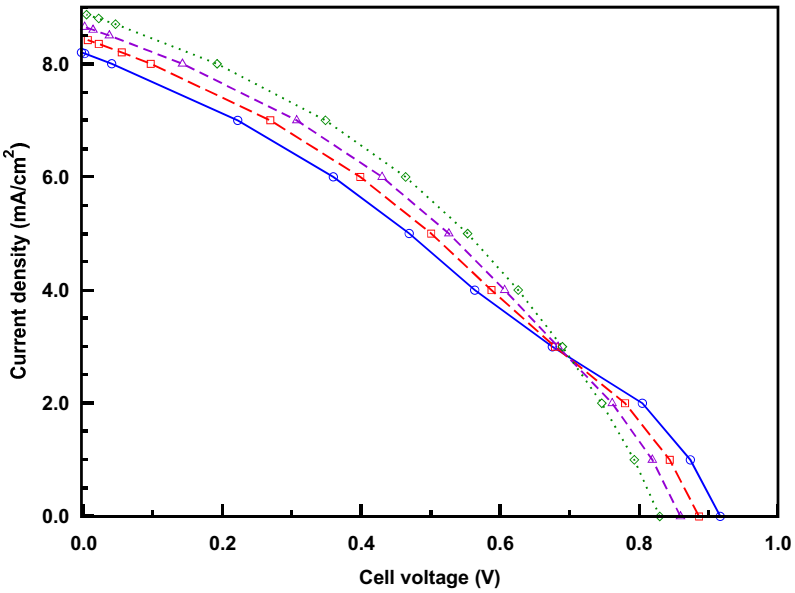

Figure 7-6: Effect of perovskite equilibrium Fermi level on the base recombination case J-V curves. Moving towards N-type doping (circles and solid line) increases open circuit voltage but decreases short circuit current and maximum power. P-type doping (diamonds and dotted line) yields the best result. Squares and dashed line indicates intrinsic perovskite, triangles and dashed line light P-type doping.

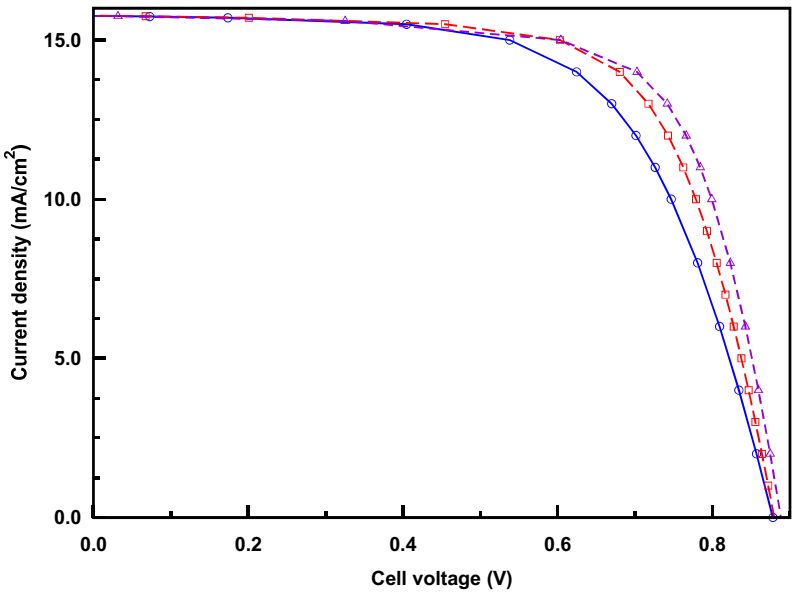

Figure 7-7: Effect of perovskite equilibrium Fermi level on the alternate recombination case J-V curves. P-type doping (triangles and dashed line) improves fill factor significantly and open circuit voltage slightly. N-type doping (circles and solid line) decreases device performance compared to the intrinsic (squares and dashed line) case.

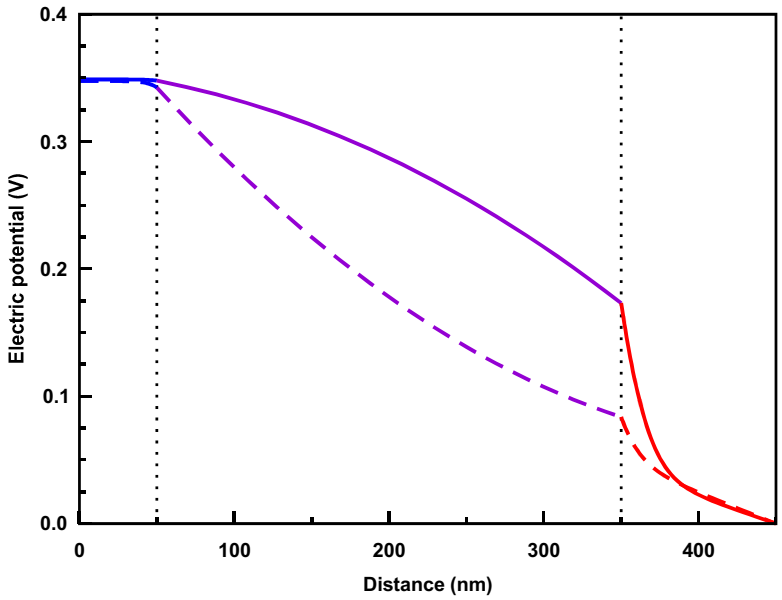

Figure 7-8: Electric potential at approximately 700 mV forward bias for the alternate recombination scheme cell with -3.905 eV (N-type doping, solid lines) and -5.260 eV (P-type doping, dashed lines) equilibrium Fermi levels. Vertical lines indicate perovskite boundaries. P-type doping (lower Fermi level) reduces electric potential change in spiro and increases potential change in the perovskite (i.e. increases the average electric field inside the absorber).

7.3.4 Effect of Spiro Doping

As seen in the previous sections, spiro conductivity and band bending plays a major role in limiting the performance of simulated devices. Therefore added doping of the spiro would seem to be a viable way to improve power generation. Three different doping densities were simulated for both the recombination schemes. In addition to just changing equilibrium hole concentration, doping also moves the equilibrium Fermi level according to the equation

$$E_{F,new} = E_{F,old} + \frac{k_B T}{q} \cdot \ln\left(\frac{p_{eq,old}}{p_{eq,new}}\right) \tag{7.34}$$

Hole concentrations and corresponding Fermi levels can be found in table 7.4.

Simulated J-V curves are shown in figures 7-9 (bulk recombination) and 7-10 (surface recombination). Doping the spiro layer generates the same effect as P-type doping of the perovskite: spiro band bending decreases improving conductivity (due to reduced hole depletion) and increasing the average built-in field in the perovskite. The results are improved fill factors for both recombination schemes and significantly lowered open circuit values for the bulk recombination case (see previous section). Increased electric potential change in perovskite decreases surface recombination in the alternate recombination scheme improving open circuit voltages by a few millivolts.

Hole concentration $1/\mathrm{m}^3$	**Fermi level** eV
$2.81 \cdot 10^{22}$	-4.985
$5.00 \cdot 10^{22}$	-5.000
$8.89 \cdot 10^{22}$	-5.015

Table 7.4: Equilibrium hole concentrations and corresponding Fermi levels used in modelling the effect of spiro doping on cell J-V curves.

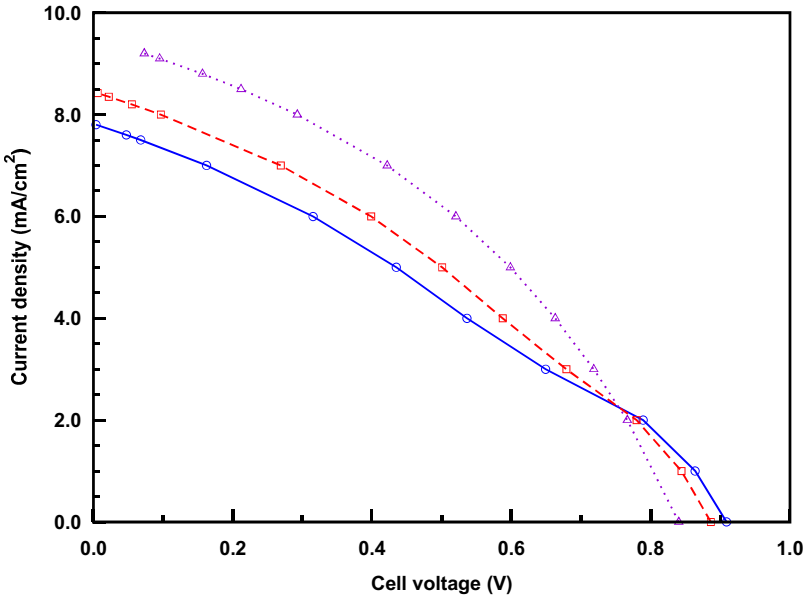

Figure 7-9: Simulated J-V curves for different doping densities using the bulk recombination scheme. Hole concentrations were $2.81 \cdot 10^{22}$ (circles and solid line), $5.00 \cdot 10^{22}$ (squares and dashed line) and $8.89 \cdot 10^{22}$ 1/m^3 (triangles and dotted line).

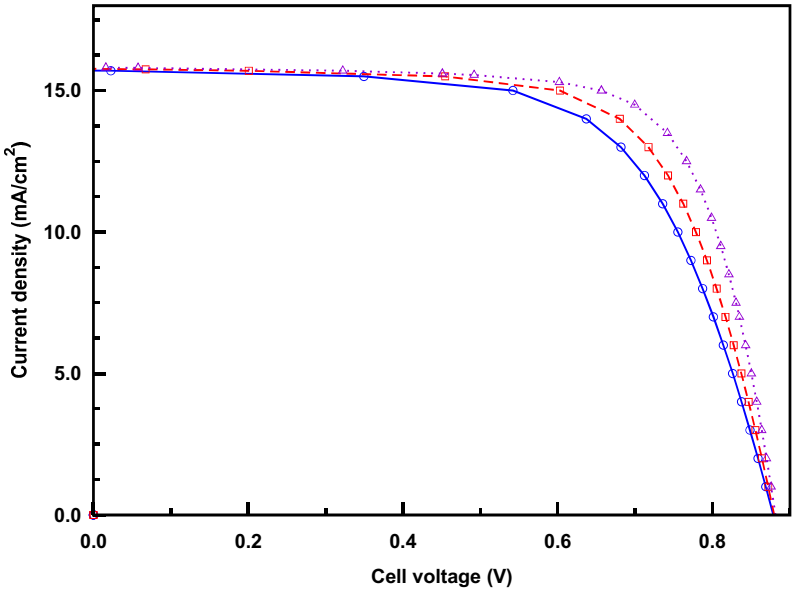

Figure 7-10: Simulated J-V curves for different doping densities using the surface recombination scheme. Hole concentrations were $2.81 \cdot 10^{22}$ (circles and solid line), $5.00 \cdot 10^{22}$ (squares and dashed line) and $8.89 \cdot 10^{22}$ 1/m^3 (triangles and dotted line).

7.4 Conclusions

The perovskite solar cell has been modelled as a p-i-n heterojunction using continuum drift-diffusion equations. The results indicate that electric fields play a significant role in charge transport in the device. In particular the nature of the interface between the perovskite absorber and spiro-OMeTAD hole selective contact would appear to have a significant effect in device performance. Band bending of the spiro valence band near the perovskite results in a hole depletion layer which increases series resistance but decreases any potential surface recombination at this interface.

However, the analysis relies on several unproven assumptions such as the perovskite being an intrinsic semiconductor and no mobile ions inside either the perovskite or spiro. It could very well be that spiro behaves more as an electrolyte than a semiconductor and that the anomalous hysteresis observed in perovskite cells [63] is due to mobile ions. As such, the work contained in this chapter should be considered exploratory and at best as a starting point for more rigorous studies. The most important objectives of future work should be to confirm the mode of charge transport and the importance of various possible recombination pathways in the device.

Chapter 8

Conclusions and Outlook

In this work device level charge transport models describing dye-sensitized and perovskite solar cells were developed.

In the case of dye-sensitized solar cells the processes governing cell operation are quite well understood as a result of more than two decades of scientific studies meaning that the presented model does not contain anything that has not been previously published by other authors. However, to the author's knowledge, this is the first time when features such as nonlinear recombination and trapping, mass transport in the electrolyte, nonideal regeneration, and substrate recombination are all incorporated into a single model. Although the model contains the relevant device physics, some flaws remain: the optical model is admittedly too simple for a broad range of wavelengths and it is possible that the substrate recombination blocking layer resistance is large enough to warrant inclusion into the model.

The biggest achievement of this work is the solution to the device model inverse problem by using analytical approximations and spreadsheet calculations. Two different methods were developed corresponding to low and high light intensities. The difference between the two is that in the low light intensity approximation mass transport in the electrolyte is completely omitted whereas in the high light intesity case tri-iodide transport is included. In both models the effect of iodide diffusion is assumed to be negligible. Based on simulations made with the full numerical model, this is a good approximation for typical electrolyte formulations where iodide concentration is about ten times higher than that of tri-iodide. The low light intensity inverse solution was applied to an experimental cell resulting in highly accurate predictions for observed I-V curves even though the analysis utilized only data measured at open circuit. For the measured cell, charge transport in the TiO_2 photoelectrode did limit electron collection but this is unlikely to be the case for higher efficiency cells made by others [14]. Dye regeneration appeared to be perfect in the measured cell even at high voltages, which appears to contradict previous work [42, 43]. However, it is possible that the measured voltages were simply not high enough to cause significant recombination to the oxidized dye molecules. Therefore both the transient absorption measurement described by Anderson et al. [43] and the impedance method of this work should be conducted on the same cell and the conclusions compared.

In the future the mass transport model of the cell should be validated by applying the high light intensity inverse solution to experimental cell data. This requires controlling cell temperature and a reference electrode for separating photoelectrode and counter electrode responses. Placing the cell on a hot plate is an obvious solution to the former, dividing the counter electrode conductor surface by e.g. laser scribing can be used to achieve the latter. The resistive and capacitive properties of the blocking layers should be measured in order to confirm the observation that blocking layer capacitance can be seen in the high frequency parts of impedance plots and that the resistance does not distort photoelectrode transport resistance measurements. Provided that the inverse solution is successful for experimental cells also at high light intensities, the method should be made part of routine analysis of new cell designs utilizing novel materials. It should also be noted that the fundamental principles of the inverse solutions (fitting measured data to analytical solutions of physics-based charge transport models) are applicable to all electrical devices. Therefore inverse problem solutions for other devices should be explored.

In contrast to the dye cells very little is known about perovskite solar cell device physics. In this work perovskite cells are assumed to work as p-i-n heterojunctions, but this cannot be taken for granted. Based on the simulations, the built-in electric field appears to play a major role in improving charge separation. The work functions and band structures of the cell materials would lead one to suggest that the perovskite absorber contains many times more free electrons than holes. Therefore hole transport could be a performance limiting factor.

Future work on perovskite device physics should focus on finding the correct picture for electric potential distribution in the cell — which is likely to involve the observed hysteresis — as well as quantifying the current lost to different recombination processes.

Appendix A

Complex Number Representation of Sinusoidal Signals

This appendix shows how complex numbers can be used to represent the amplitudes and phase shifts of sinusoidal signals. As shown below, this greatly simplifies the the formalism needed to express differential equation solutions involving sinusoidal boundary conditions.

We will start by considering a differential equation of the from

$$\frac{\partial f}{\partial t} = -\frac{\partial f}{\partial x} \tag{A.1}$$

subject to the condition

$$f(x = 0, t) = A \sin(\omega t + \varphi) \tag{A.2}$$

where t is the time variable, A is the amplitude, ω is the angular frequency and φ is the phase shift of the sinusoidal signal.

The solution to this has the form

$$\begin{aligned} f = &\sin(\omega t + \varphi) \left(D_1 \sin(\omega x) + D_2 \cos(\omega x)\right) \\ &+ \cos(\omega t + \varphi) \left(D_3 \sin(\omega x) + D_4 \cos(\omega x)\right) \end{aligned} \tag{A.3}$$

where D_1, D_2, D_3 and D_4 are constants.

After applying the boundary condition this simplifies to

$$f = A \sin(\omega t + \varphi) \cos(\omega x) - A \cos(\omega t + \varphi) \sin(\omega x) \tag{A.4}$$

Both the general and specific solutions are quite complicated compared to the original partial differential equation. Therefore one would like to use a more compact notation.

We begin by noting that the solution can be expressed as a simple sine wave using a position-

dependent change in phase shift

$$f = A\sin(\omega t + \varphi - \omega x) \tag{A.5}$$

The importance of this is that for any sine wave amplitude and phase shift define the entire wave. No further information is needed.

The problem defined in equations A.1 and A.2 is changed into the complex formalism by changing the boundary conditions function from a sine wave to a complex exponential function.

$$f(x = 0, t) = Ae^{i(\omega t+\varphi)} \tag{A.6}$$

Strictly speaking this boundary condition is different than the previous one because the complex exponential also has an imaginary part, but if one considers only amplitude and phase shift to be important (as is the case in any real world application) then this formalism will give identical results.

The complex exponential boundary condition enables solutions to be sought by separation of variables

$$f = g(x)e^{i(\omega t+\varphi)} \tag{A.7}$$

Inserting this into equation A.1 yields

$$\begin{aligned} i\omega g(x)e^{i(\omega t+\varphi)} &= -\frac{\partial g(x)}{\partial x}e^{i(\omega t+\varphi)} \\ \Rightarrow g(x) &= C_1 e^{-i\omega x} \end{aligned} \tag{A.8}$$

Applying the boundary condition gives

$$f = Ae^{i(\omega t+\varphi-\omega x)} \tag{A.9}$$

As one can see, the complex number formalism results in the same amplitude (A) and phase shift ($\varphi - \omega x$) as the sine wave formalism.

Other more complicated differential equations often result in solutions where amplitudes are complex numbers. These can be converted into the real number amplitude and phase shift formalism using Euler's formula and trigonometric indentities

$$(x + iy)e^{i(\omega t+\varphi)} = \sqrt{x^2 + y^2} \cdot e^{i(\omega+\varphi+\arctan(-\frac{y}{x}))} \tag{A.10}$$

Appendix B

Dye-Sensitized Solar Cell Impedance Response

Impedance measurements are often visualized using the Nyquist plot where the real part (also known as resistance) of the complex impedance is plotted as the x-axis and the imaginary part (reactance) as the y-axis. Usually the y-axis is inverted. Figure B-1 shows an example Nyquist impedance plot of an experimental dye solar cell. Typically at least three parts can be easily distinguished in the plot: series resistance caused by the FTO glass, high frequency arc caused by the counter electrode and a low frequency arc caused by the photoelectrode. When measured at low enough bias voltages, the photoelectrode arc shows a straight line at high frequencies indicating the presence of significant transport resistance caused by slow diffusion of electrons in the semiconductor film. Sometimes it is also possible to see a third arc at very low frequencies that is caused by slow diffusion of redox ions in the electrolyte (not shown in the example figure).

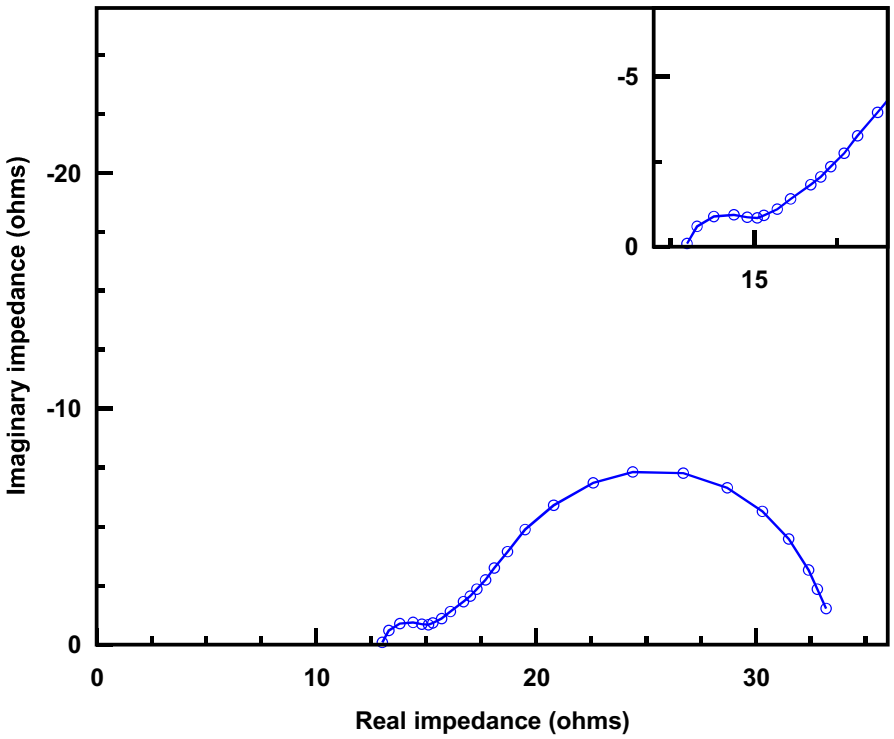

Figure B-1: An example Nyquist plot of a dye solar cell impedance spectrum. Low frequency points are on the right, high frequency on the left. Substrate series resistance is the difference between the origin and the first data point on the left. The small arc on the left is caused by the counter electrode, the bigger arc by the photoelectrode. The straight line at approximately 45 degree angle to the x-axis between the two semicircles is a sign of the photoelectrode transport resistance caused by the diffusion of electrons. The overall photoelectrode arc is caused by the combined effect of transport, recombination and capacitance.

Appendix C

Dye Solar Cell Model Numerical Solver

The equations in section 4.2.10 were solved using a numerical solver using a multiple shooting method implemented in the Python programming language. The method divides the independent variable space into multiple parts and guesses the solution at some of the boundaries of these parts. Then numerical integration is used to obtain the full solution. If the solution is the correct one, then all concentrations and their gradients are continuous across all the internal boundaries and the boundary conditions specified in sections 4.2.11 and 4.2.12 hold. Finding the correct guess is left to a numerical root finding algorithm. The integration and root finding algorithms were taken from the freely available SciPy library (http://scipy.org/). Initial guesses were computed using the analytical solutions from chapter 6. Variables were scaled by dividing them with the average values of the initial guess.

Table C.1 shows the equations constraining solution variables when the y-space is divided into four parts. The free variables are the inputs to the root finding algorithm. Numerical integration is performed from $y = 0$ to $y = 0.25$, $y = 0.5$ to $y = 0.25$, $y = 0.5$ to $y = 0.75$ and $y = 1$ to $y = 0.75$. The root is the solution where all variables are continuous at $y = 0.25$ and $y = 0.75$. An example illustrating the multiple shooting method is given in figure C-1.

Variable description	**Symbol**	$y = 0$	$y = 0.5$	$y = 1$
Electron concentration	n_{DC}	4.66	Free	Free
Gradient of electron concentration	$\frac{\partial n_{DC}}{\partial y}$	Free	Free	4.68
Iodide concentration	$c_{red,DC}$	Free	Free	Free
Gradient of iodide concentration	$\frac{\partial n_{DC}}{\partial y}$	4.69	Free	Free
Tri-iodide concentration	$c_{ox,DC}$	Free	Free	Free
Gradient of tri-iodide concentration	$\frac{\partial c_{ox,DC}}{\partial y}$	4.70	Free	Free
Iodide integral	I_{red}	4.79	Free	4.80
Tri-iodide integral	I_{ox}	4.81	Free	4.82

Table C.1: Equations constraining the variables in the DC dye solar cell model.

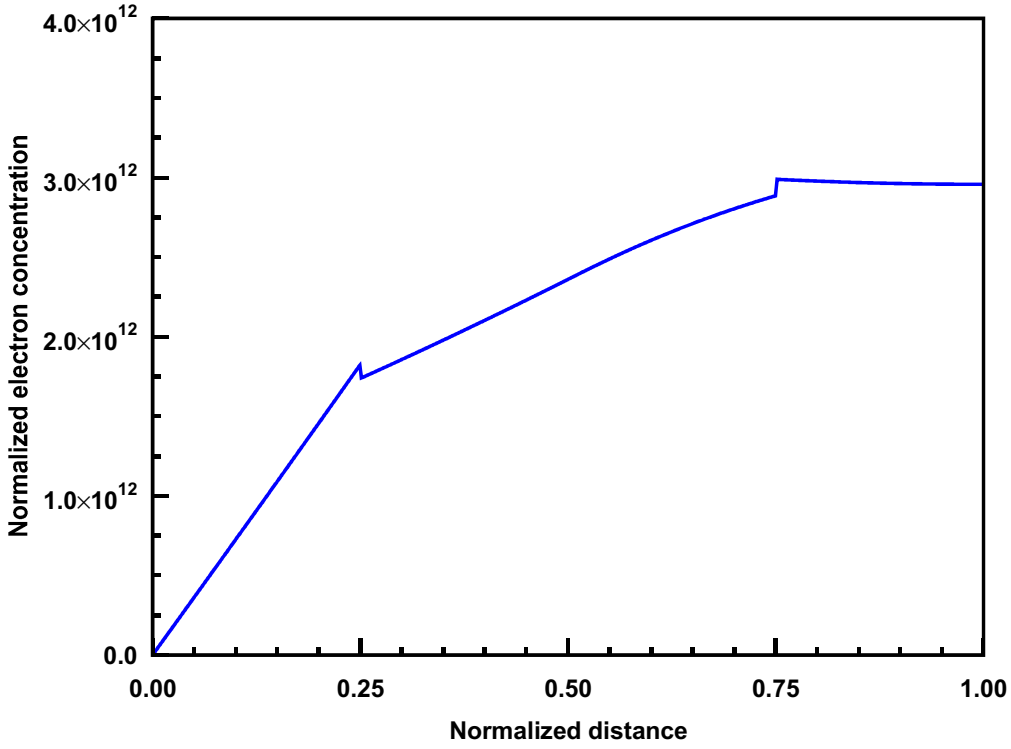

Figure C-1: Normalized electron concentration calculated with the multiple shooting method using an analytical initial guess. Concentration is discontinuous at normalized distances $y = 0.25$ and $y = 0.75$ indicating that a root finding algorithm must be used to obtain the correct solution.

Appendix D

Perovskite Cell Model Numerical Solver

The perosvkite cell numerical solver was also implemented in Python using the SciPy library for numerical integration and root finding. However, a shooting method was used instead of multiple shooting. Gradient of the electric potential at the metal contact of the P-type layer was specified manually and the boundary conditions and differential equations were used to calculate the electron concentration at the N-type–metal contact. If the initial electric potential gradient was correct, then the electron concentration at the other end would match equation 7.14. Electron concentration at the perovskite-P-type interface is not given directly by the boundary conditions so it must the found numerically by iteration until the hole gradient at the N-type–perovskite interface matches equation 7.21.

Bibliography

[1] Statistical Review of World Energy 2014. BP: www.bp.com/statisticalreview, June 2014.

[2] Air quality guidelines. Global update 2005. Particulate matter, ozone, nitrogen dioxide and sulfur dioxide. WHO: http://www.euro.who.int/en/publications/key-publications, June 2014.

[3] Tomas Markvart. *Solar Electricity*. John Wiley & Sons, second edition, 2000.

[4] Levelized Cost and Levelized Avoided Cost of New Generation Resources in the Annual Energy Outlook 2014. U.S. Energy Information Administration: http://www.eia.gov/forecasts/aeo/, June 2014.

[5] Hironori Arakawa, Takeshi Yamaguchi, Takanori Sutou, Yutaro Koishi, Nobuyuki Tobe, Daisuke Matsumoto, and Takuma Nagai. Efficient dye-sensitized solar cell sub-modules. *Current Applied Physics*, 10(2, Supplement):S157 – S160, 2010.

[6] Ravi Harikisun and Hans Desilvestro. Long-term stability of dye solar cells. *Solar Energy*, 85(6):1179 – 1188, 2011.

[7] Peter J. Holliman, Matthew L. Davies, Arthur Connell, Beatriz Vaca Velasco, and Trystan M. Watson. Ultra-fast dye sensitisation and co-sensitisation for dye sensitized solar cells. *Chem. Commun.*, 46:7256–7258, 2010.

[8] Trystan M. Watson, Ian Mabbett, and David Worsley. Ultrafast TiO_2 Sintering of Metal Mounted Dye-Sensitized Solar Cells. *ECS Transactions*, 33(17):151–158, 2011.

[9] Sven Soedergren, Anders Hagfeldt, Joergen Olsson, and Sten-Eric Lindquist. Theoretical Models for the Action Spectrum and the Current-Voltage Characteristics of Microporous Semiconductor Films in Photoelectrochemical Cells. *The Journal of Physical Chemistry*, 98(21):5552–5556, 1994.

[10] Juan Bisquert and Vyacheslav S. Vikhrenko. Interpretation of the Time Constants Measured by Kinetic Techniques in Nanostructured Semiconductor Electrodes and Dye-Sensitized Solar Cells. *The Journal of Physical Chemistry B*, 108(7):2313–2322, 2004.

[11] P. Salvador, M. Gonzalez Hidalgo, Arie Zaban, and Juan Bisquert. Illumination Intensity Dependence of the Photovoltage in Nanostructured TiO2 Dye-Sensitized Solar Cells. *The Journal of Physical Chemistry B*, 109(33):15915–15926, 2005.

[12] Petra J. Cameron, Laurence M. Peter, and Sarmimala Hore. How Important is the Back Reaction of Electrons via the Substrate in Dye-Sensitized Nanocrystalline Solar Cells? *The Journal of Physical Chemistry B*, 109(2):930–936, 2005.

[13] K. Lobato, L. M. Peter, and U. Würfel. Direct Measurement of the Internal Electron Quasi-Fermi Level in Dye Sensitized Solar Cells Using a Titanium Secondary Electrode. *The Journal of Physical Chemistry B*, 110(33):16201–16204, 2006. PMID: 16913742.

[14] Qing Wang, Seigo Ito, Michael Grätzel, Francisco Fabregat-Santiago, Ivan Mora-Sero, Juan Bisquert, Takeru Bessho, and Hachiro Imai. Characteristics of High Efficiency Dye-Sensitized Solar Cells. *The Journal of Physical Chemistry B*, 110(50):25210–25221, 2006. PMID: 17165965.

[15] Gerrit Boschloo and Anders Hagfeldt. Characteristics of the Iodide/Triiodide Redox Mediator in Dye-Sensitized Solar Cells. *Accounts of Chemical Research*, 42(11):1819–1826, 2009. PMID: 19845388.

[16] Juan Bisquert, Francisco Fabregat-Santiago, Ivan Mora-Sero, Germa Garcia-Belmonte, and Sixto Gimenez. Electron Lifetime in Dye-Sensitized Solar Cells: Theory and Interpretation of Measurements. *The Journal of Physical Chemistry C*, 113(40):17278–17290, 2009.

[17] James R. Jennings, Feng Li, and Qing Wang. Reliable Determination of Electron Diffusion Length and Charge Separation Efficiency in Dye-Sensitized Solar Cells. *The Journal of Physical Chemistry C*, 114(34):14665–14674, 2010.

[18] Janne Halme, Paula Vahermaa, Kati Miettunen, and Peter Lund. Device Physics of Dye Solar Cells. *Advanced Materials*, 22(35):E210–E234, 2010.

[19] Piers R. F. Barnes, Assaf Y. Anderson, James R. Durrant, and Brian C. O'Regan. Simulation and measurement of complete dye sensitised solar cells: including the influence of trapping, electrolyte, oxidised dyes and light intensity on steady state and transient device behaviour. *Phys. Chem. Chem. Phys.*, 13:5798–5816, 2011.

[20] Walter A. Harrison. *Electronic Structure and the Properties of Solids.* W. H. Freeman and Company, 1980.

[21] N. W. Ashcroft and N. D. Mermin. *Solid State Physics.* Saunders College Publishing, 1976.

[22] G. Hadziioannou and P. F. van Hutten, editors. *Semiconducting Polymers — Chemistry, Physics and Engineering.* WILEY-VCH, 2000.

[23] J. R. Hook and H. E. Hall. *Solid State Physics.* John Wiley & Sons, 2nd edition, 1991.

[24] F. Mandl. *Statistical Physics*. John Wiley & Sons, 2nd edition edition, 1988.

[25] A. J. Bard and L. R. Faulkner. *Electrochemical Methods*. John Wiley & Sons, 1980.

[26] S. M. Sze. *Physics of Semiconductor Devices*. John Wiley & Sons, 2nd edition, 1981.

[27] A. Einstein and A. D. Cowper (translator). *Investigations on the Theory of the Brownian Motion*. Methuen & Co., unknown year.

[28] Jenny Nelson. *The Physics of Solar Cells*. Imperial College Press, 2003.

[29] Antonio Luque and Steven Hegedus, editors. *Handbook of Photovoltaic Science and Engineering*. John Wiley & Sons, 2003.

[30] J Ross Macdonald, editor. *Impedance Spectroscopy: Emphasizing Solid Materials and Systems*. John Wiley & Sons, 1987.

[31] Erwin Kreyszig. *Advanced Engineering Mathematics*. John Wiley & Sons, sixth edition edition, 1988.

[32] Michael Grätzel. Conversion of sunlight to electric power by nanocrystalline dye-sensitized solar cells. *Journal of Photochemistry and Photobiology A: Chemistry*, 164(13):3 – 14, 2004. Proceedings of the Dye Solar Cell Osaka ICP-21 Pre-symposium. Dedicated to Professor Shozo Yanagida on the occasion of his retirement.

[33] Anders Hagfeldt, Gerrit Boschloo, Licheng Sun, Lars Kloo, and Henrik Pettersson. Dye-Sensitized Solar Cells. *Chemical Reviews*, 110(11):6595–6663, 2010.

[34] Seigo Ito, Takurou N. Murakami, Pascal Comte, Paul Liska, Carole Grätzel, Mohammad K. Nazeeruddin, and Michael Grätzel. Fabrication of thin film dye sensitized solar cells with solar to electric power conversion efficiency over 10%. *Thin Solid Films*, 516(14):4613 – 4619, 2008. 6th International Conference on Coatings on Glass and Plastics (ICCG6)-Advanced Coatings for Large-Area or High-Volume Products-.

[35] Martin A. Green, Keith Emery, Yoshihiro Hishikawa, Wilhelm Warta, and Ewan D. Dunlop. Solar cell efficiency tables (version 43). *Progress in Photovoltaics: Research and Applications*, 22(1):1–9, 2014.

[36] Laurence M. Peter. Dye-sensitized nanocrystalline solar cells. *Phys. Chem. Chem. Phys.*, 9:2630–2642, 2007.

[37] N. Papageorgiou, M. Grtzel, and P.P. Infelta. On the relevance of mass transport in thin layer nanocrystalline photoelectrochemical solar cells. *Solar Energy Materials and Solar Cells*, 44(4):405 – 438, 1996.

[38] Sara E. Koops, Brian C. ORegan, Piers R. F. Barnes, and James R. Durrant. Parameters Influencing the Efficiency of Electron Injection in Dye-Sensitized Solar Cells. *Journal of the American Chemical Society*, 131(13):4808–4818, 2009.

[39] Francisco Fabregat-Santiago, Juan Bisquert, Germ Garcia-Belmonte, Gerrit Boschloo, and Anders Hagfeldt. Influence of electrolyte in transport and recombination in dye-sensitized solar cells studied by impedance spectroscopy. *Solar Energy Materials and Solar Cells*, 87(14):117 – 131, 2005.

[40] Kai Zhu, Nikos Kopidakis, Nathan R. Neale, Jao van de Lagemaat, and Arthur J. Frank. Influence of Surface Area on Charge Transport and Recombination in Dye-Sensitized TiO_2 Solar Cells. *The Journal of Physical Chemistry B*, 110(50):25174–25180, 2006. PMID: 17165961.

[41] Ryuzi Katoh, Annemarie Huijser, Kohjiro Hara, Tom J. Savenije, and Laurens D. A. Siebbeles. Effect of the Particle Size on the Electron Injection Efficiency in Dye-Sensitized Nanocrystalline TiO2 Films Studied by Time-Resolved Microwave Conductivity (TRMC) Measurements. *The Journal of Physical Chemistry C*, 111(28):10741–10746, 2007.

[42] James R. Jennings, Yeru Liu, and Qing Wang. Efficiency Limitations in Dye-Sensitized Solar Cells Caused by Inefficient Sensitizer Regeneration. *The Journal of Physical Chemistry C*, 115(30):15109–15120, 2011.

[43] Assaf Y. Anderson, Piers R. F. Barnes, James R. Durrant, and Brian C. O'Regan. Quantifying Regeneration in Dye-Sensitized Solar Cells. *JOURNAL OF PHYSICAL CHEMISTRY C*, 115(5):2439–2447, FEB 10 2011.

[44] Anneke Hauch and Andreas Georg. Diffusion in the electrolyte and charge-transfer reaction at the platinum electrode in dye-sensitized solar cells. *Electrochimica Acta*, 46(22):3457 – 3466, 2001.

[45] Juan Bisquert, Germa Garcia-Belmonte, Francisco Fabregat-Santiago, Noemi S. Ferriols, Peter Bogdanoff, and Ernesto C. Pereira. Doubling Exponent Models for the Analysis of Porous Film Electrodes by Impedance. Relaxation of TiO2 Nanoporous in Aqueous Solution. *The Journal of Physical Chemistry B*, 104(10):2287–2298, 2000.

[46] NSG TEC Datasheet. Pilkington: http://www.pilkington.com, May 2014.

[47] Minna Toivola, Timo Peltola, Kati Miettunen, Janne Halme, and Peter Lund. Thin film nano solar cells – from device optimization to upscaling. *Journal of Nanoscience and Nanotechnology*, 10(2):1078–1084, 2010-02-01T00:00:00.

[48] N. Papageorgiou, Y. Athanassov, M. Armand, P. Bonhote, H. Pettersson, A. Azam, and M. Gratzel. The Performance and Stability of Ambient Temperature Molten Salts for Solar Cell Applications. *Journal of The Electrochemical Society*, 143(10):3099–3108, 1996.

[49] Tomas Leijtens, Jongchul Lim, Jol Teuscher, Taiho Park, and Henry J. Snaith. Charge Density Dependent Mobility of Organic Hole-Transporters and Mesoporous TiO_2 Determined by Transient Mobility Spectroscopy: Implications to Dye-Sensitized and Organic Solar Cells. *Advanced Materials*, 25(23):3227–3233, 2013.

[50] N. Papageorgiou, C. Barb, and M. Grtzel. Morphology and Adsorbate Dependence of Ionic Transport in Dye Sensitized Mesoporous TiO_2 Films. *The Journal of Physical Chemistry B*, 102(21):4156–4164, 1998.

[51] Hui-Seon Kim, Chang-Ryul Lee, Jeong-Hyeok Im, Ki-Beom Lee, Thomas Moehl, Arianna Marchioro, Soo-Jin Moon, Robin Humphry-Baker, Jun-Ho Yum, Jacques E. Moser, Michael Gratzel, and Nam-Guy Park. Lead iodide perovskite sensitized all-solid-state submicron thin film mesoscopic solar cell with efficiency exceeding 9%. *Scientific Reports*, 2:591, 2012.

[52] Michael M. Lee, Jol Teuscher, Tsutomu Miyasaka, Takurou N. Murakami, and Henry J. Snaith. Efficient Hybrid Solar Cells Based on Meso-Superstructured Organometal Halide Perovskites. *Science*, 338:643–647, 2012.

[53] James M. Ball, Michael M. Lee, Andrew Hey, and Henry J. Snaith. Low-temperature processed meso-superstructured to thin-film perovskite solar cells. *Energy Environ. Sci.*, 6:1739–1743, 2013.

[54] Antonio Abate, Daniel R. Staff, Derek J. Hollman, Henry J. Snaith, and Alison B. Walker. Influence of ionizing dopants on charge transport in organic semiconductors. *Phys. Chem. Chem. Phys.*, 16:1132–1138, 2014.

[55] Jarvist M. Frost, Keith T. Butler, Federico Brivio, Christopher H. Hendon, Mark van Schilfgaarde, and Aron Walsh. Atomistic origins of high-performance in hybrid halide perovskite solar cells. *Nano Letters*, 14(5):2584–2590, 2014. PMID: 24684284.

[56] Federico Brivio, Alison B. Walker, and Aron Walsh. Structural and electronic properties of hybrid perovskites for high-efficiency thin-film photovoltaics from first-principles. *APL Materials*, 1(4):–, 2013.

[57] I. S. Grant and W. R. Phillips. *Electromagnetism*. John Wiley & Sons, 1975.

[58] J. Burschka, N. Pellet, S-J. Moon, R. Humphry-Baker, P. Gao, M. K. Nazeeruddin, and M. Gr ätzel. Sequential deposition as a route to high-performance perovskite-sensitized solar cells. *Nature*, 499:316–320, 2013.

[59] Dongqin Bi, Lei Yang, Gerrit Boschloo, Anders Hagfeldt, and Erik M. J. Johansson. Effect of Different Hole Transport Materials on Recombination in $CH_3NH_3PbI_3$ Perovskite-Sensitized Mesoscopic Solar Cells. *The Journal of Physical Chemistry Letters*, 4(9):1532–1536, 2013.

[60] Philip Schulz, Eran Edri, Saar Kirmayer, Gary Hodes, David Cahen, and Antoine Kahn. Interface energetics in organo-metal halide perovskite-based photovoltaic cells. *Energy Environ. Sci.*, 7:1377–1381, 2014.

[61] Constantinos C. Stoumpos, Christos D. Malliakas, and Mercouri G. Kanatzidis. Semiconducting Tin and Lead Iodide Perovskites with Organic Cations: Phase Transitions, High Mobilities, and Near-Infrared Photoluminescent Properties. *Inorganic Chemistry*, 52(15):9019–9038, 2013.

[62] Petra J. Cameron and Laurence M. Peter. Characterization of titanium dioxide blocking layers in dye-sensitized nanocrystalline solar cells. *The Journal of Physical Chemistry B*, 107(51):14394–14400, 2003.

[63] Henry J. Snaith, Antonio Abate, James M. Ball, Giles E. Eperon, Tomas Leijtens, Nakita K. Noel, Samuel D. Stranks, Jacob Tse-Wei Wang, Konrad Wojciechowski, and Wei Zhang. Anomalous Hysteresis in Perovskite Solar Cells. *The Journal of Physical Chemistry Letters*, 5(9):1511–1515, 2014.